6.2.6 Suspension Seismic Surveys

6.2.6.1 Introduction

Suspension seismic P-S logging at boreholes RF#14 through #29 was conducted from September 17 to 19 and December 5 to 12, 2000 using an OYO Model 170 P-S suspension logging system. In addition, suspension seismic logging was conducted at borehole RF#13 located in the center of the potential WHB footprint on December 15, 1998 using similar equipment and methods. Although logged before the current phase of site exploration, the borehole RF#13 results are presented herein due to their particular relevance to this scientific analysis. The locations of boreholes RF#13 through RF#29 are shown on Figure 3.

6.2.6.2 Equipment

As shown on Figure 29, the suspension system included a downhole tool, consisting of an energy source, isolation tubes and two biaxial geophone receivers; an OYO Model 170 digital data recorder for recording the seismic waves arriving at the two geophones; and a hoisting/depth measurement system.

The distance from the energy source, which was mounted near the bottom of the tool, to the near (lower) receiver was approximately 7.11 to 7.17 feet, except it was approximately 3.74 feet at borehole RF#16. The distance between receivers was approximately 3.33 to 3.36 feet.

The energy source is a solenoid whose activation causes a "hammer" to strike the tool casing, producing an impulsive pressure wave in the borehole liquid.[3] This pressure wave transmits energy to the borehole wall, producing both P and S waves that travel through the geologic formation. The dominant S-wave frequencies are typically 500 to 2,000 hertz and the P-wave frequencies, 1,000 to 3,000 hertz. The wave field can be treated as a point source in an infinite medium since the wavelength is sufficiently longer than the borehole diameter. As the P and S waves arrive near each geophone, they couple through the borehole liquid to the geophones. Flexible rubber tubes are incorporated in the tool casing to attenuate and filter wave propagation along the tool.

Each biaxial geophone included one vertical sensor and one horizontal sensor. The geophones are mounted in the downhole tool at an elevation higher than the source.

The OYO Model 170 recorder has six channels, two of which can record simultaneously. Each channel records 1024 12-bit samples at equal time intervals. The record length can be set at 5, 10, 20, 50 or 100 milliseconds. The recorded data was displayed on a cathode ray tube display, which allows the operator to adjust the gains, filters, delay time, pulse length (energy), and sample rate to improve the quality of the data before final recording of the data. In addition, the recorder allows the operator to sum up to eight sampling sequences to improve the signal-to-noise ratio. Before moving on to the next measurement depth, the final record was printed on paper tape with a common time scale and was stored on a floppy diskette for further processing.

---

[3] Suspension seismic measurements can only be performed below the level to which the borehole is filled with a liquid such as water or drilling mud.

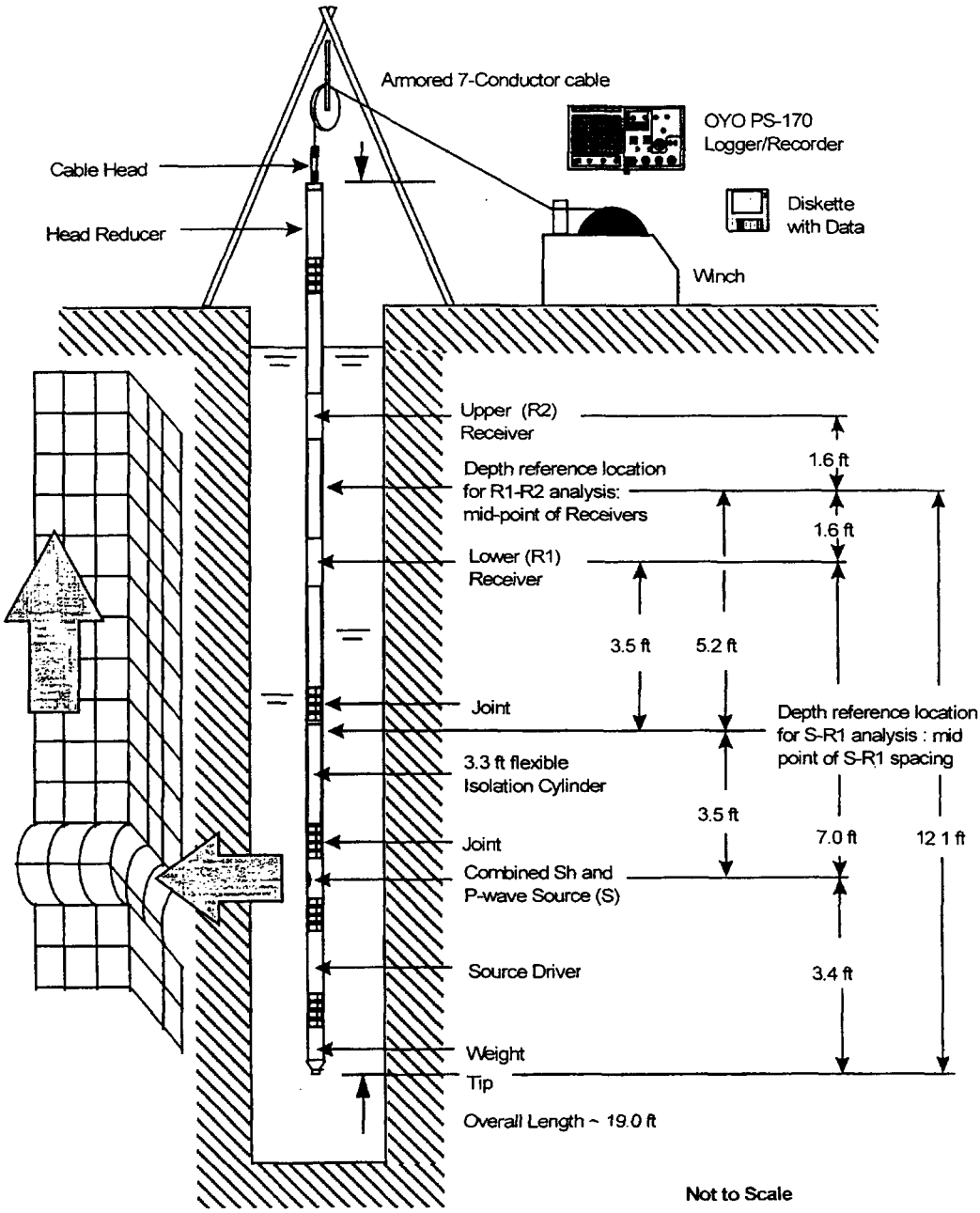

Source: Luebbers (2002b, page 18 of Attachment 4)

Note: The dimensions shown are typical dimensions and will vary with the specific equipment used for a particular survey. The dimensions have been converted from meters to feet.

Figure 29. Schematic Diagram of OYO P-S Logging Equipment

6.2.6.3 Procedures

To conduct the survey, the borehole[4] was filled with water and the suspension tool was lowered to the bottom of the casing by a winch and armored cable containing the data leads. The cable moved across a digital wheel assembly that recorded the movement of the cable and hence the depth of the tool.

Logging was conducted from lower elevations to higher ones, with velocity measurements being made at 0.5-meter (1.64-foot) intervals (occasional variations occurred). At each measurement depth the seismic energy source was actuated three times: (1) the source is activated in one direction (arbitrarily called the "normal" direction), producing dominantly horizontal shear with some vertical compression, and the waves are recorded on the horizontal geophones; (2) the source is activated in the opposite direction (referred to as the "reverse" direction), again producing dominantly horizontal shear with some vertical compression, and the waves are again recorded on the horizontal geophones; and (3) the source is again activated in the normal direction and the waves are recorded on the vertical geophones. The data logger began the record at the time the signal was transmitted to the actuator to cause the hammer to strike.

Upon completion of the measurements in each borehole and with the probe at zero depth, the operator checked that the digital depth readout indicated that the probe was at zero depth.

6.2.6.4 Data Evaluation and Results

The suspension data were analyzed by picking arrival times for both the compression wave and the shear wave at appropriate sensors. The compression wave was normally picked as the first break on the vertical sensors. The shear waves were identified by comparing the records for the normal source actuation and the reverse source actuation and noting a reversal in the waveform. The travel time to the peak of the first shear wave cycle was then picked; this point could be identified more accurately than the first break due to the continued signal from the compression wave and noise.

In some cases an arrival could not be identified with confidence on one or more of the sensors and this is reflected by a gap in the data. Most of the data where a pick was not made involves the compression wave. In general, the suspension seismic method has difficulty in recording compression waves above the water table, and all the logging reported herein was performed above the water table. There were also a significant number of measurement locations where a shear wave could be identified on the near receiver recording, but not on the far one. This is caused by loss of signal strength due to spatial spreading and material damping. Material damping can be affected by the type of material and by the type and extent of discontinuities in the medium, such as fractures, lithophysae, joints, and faults.

The OYO Model 170 suspension seismic logger system enables measurement of seismic velocity in two ways. Generally, the usual method is to calculate the velocity based on the difference in wave travel times from the source to the far and near receivers and the known distance between the receivers. The second method is to calculate the velocity based on the wave travel time from

[4] RF#22 was not cased at the time of suspension seismic logging. In all other boreholes a casing had been grouted in place before the geophysical survey.

the source to the near receiver and the known distance between the source and near receiver. The advantages of the receiver-to-receiver method are:

- The receiver-to-receiver is normally more accurate because the picks are made from the peak of the arrival waveform. The analyst picks the arrival waveform and software is used to find the peaks.

- For the typical setup, and for the results reviewed herein, receiver-to-receiver data has higher resolution because the distance between receivers is usually less than one-half the distance between the source and near receiver. Thus, the receiver-to-receiver data is better suited to identifying thin layers of notably high or low velocity, but gives the appearance of having more scatter.

- In the source-to-near receiver analysis the "normal" and "reverse" travel times were averaged, which reduces errors due to differences in source actuation pulses. In the receiver-to-receiver analysis, only the normal travel times were interpreted.

- Source-to-receiver travel times are subject to a source delay, nominally 4 milliseconds, whose variation could introduce some degree of error. In the receiver-to-receiver method the delay times cancel out, eliminating one potential source of error.

- The source-to-near receiver data are more subject to "picking" errors because the picks are based on the analyst's choice of first motion rather than detection of the peak by software. The effect of these errors on velocity is reduced, however, by the longer travel path and hence longer travel time.

- Because of the geometric arrangement of the source and the two receivers, the receiver-to-receiver survey usually extends to a depth about 5 feet closer to the ground surface than the source-to-near receiver survey.

The advantages of the source-to-near receiver method are:

- For the typical setup, and for the results reviewed herein, source-to-near receiver data has lower resolution because the distance from source to the near receiver is usually more than twice the distance between the receivers. Thus, the source-to-near receiver data should appear to have less variability (scatter) than the receiver-to-receiver data. Although less suited to identifying thin layers of notably high or low velocity, the source-to-near receiver velocities may be more appropriate for ground motion analysis because the velocity is measured over a longer interval.

- Because of the geometric arrangement of the source and the two receivers, the source-to-near receiver survey usually extends to a depth about 5 feet greater than the receiver-to-receiver survey.

Considering these points, the receiver-to-receiver results are usually considered the "primary" results and the source-to-near receiver results are used as a quality control check on the receiver-to-receiver results. Despite the general preference for receiver-to-receiver data on principle, in practice, more, and sometimes much more, of the receiver-to-receiver is missing and, primarily

for that reason, the decision was made to accept the source-to-near receiver results as being primary. Thus, on the boring logs in Attachment I, the source-to-near receiver suspension results are shown.

The reason why more receiver-to-receiver data are missing than source-to-receiver data is that the seismic waves must travel farther to reach the far receiver than to reach the near receiver and the farther the waves travel from the source, the more their amplitude is attenuated by spatial and material damping. In general, the ability to recognize the compression wave arrival at the far receiver was lost more frequently than the ability to recognize the shear wave arrival. The energy loss is higher in more fractured bedrock relative to less fractured bedrock.

The raw and filtered waveforms are reported in Scientific Notebooks SN-M&O-SCI-024-V1 (Luebbers 2002a) and SN-M&O-SCI-024-V2 (Luebbers 2002b). The interpreted arrival times and interval velocities are reported in DTN: MO0204SEPBSWHB.001. A similar suspension seismic survey of borehole RF#13 performed in 1998 is described in CRWMS M&O (1999b, Section 4.4) and the interpreted arrival times and interval velocities are reported in DTN: MO0204SEISDWHB.001. Based on an assessment of data quality, some inconsistencies were recognized in the data collected at shallow depths (generally to 25-foot depth, but as deep as 77 feet in borehole RF#25) and thus these data are ignored. The data that were collected and interpreted but ultimately ignored are summarized by depth (i.e., depth bgs to the midpoint between the two receivers) in Table 11.

Table 11. Extent of Suspension Seismic Logging in 2000

Borehole No. and Casing Condition	Data Collected	Depth of Logging	Depth of Data to be ignored
RF#14 Cased	12/9/00	543.3 ft	surface to 44.30 ft bgs
RF#15 Cased	12/5/00	316.9 ft	surface to 19.69 ft bgs
RF#16 Cased	12/12/00	446.4 ft	surface to 22.97 ft bgs
RF#17 Cased	12/11/00	648.3 ft	surface to 47.60 ft bgs
RF#18 Cased	12/12/00	484.3 ft	surface to 27.90 ft bgs
RF#19 Cased	12/7/00	638.5 ft	surface to 27.90 ft bgs
RF#20 Cased	12/7/00	151.2 ft	surface to 14.80 ft bgs
RF#21 Cased	12/7/00	184.0 ft	surface to 13.12 ft bgs
RF#22 Uncased	9/19/00	393.7 ft	Data OK
RF#23 Cased	12/7/00	151.2 ft	Data OK
RF#24 Cased	12/6/00	262.1 ft	surface to 23.00 ft bgs
RF#25 Cased	12/3/00	151.2 ft	surface to 77.10 ft bgs
RF#26 Cased	9/17/00	256.2 ft	surface to 13.12 ft bgs
RF#28 Cased	12/6/00	93.8 ft	surface to 22.97 ft bgs
RF#29 Cased	12/7/00	402.2 ft	surface to 19.69 ft bgs

Source: Page 12 of Luebbers (2002b, Attachment 4)

Notes: (1) The depth of logging is based on midpoint between source and the near receiver. (2) In the "Depth of Data to be Ignored" column, the use of the term surface is not intended to indicate that measurements were performed form borehole bottom to a depth of zero feet bgs, but rather that no data was retained from the ground surface to the stated lower limit.

The results of suspension seismic surveys are usually presented as plots of interval velocities versus depth. The velocity across the interval between the two receivers was calculated by dividing the fixed distance between the two biaxial receivers (approximately 3.3 feet) by the difference in travel times from the source to the respective receiver. The velocity across the interval between the source and the near receiver was calculated in a similar fashion by dividing the fixed distance between the source and the near receiver (approximately 7 feet) by the difference in travel time from the source to the near receiver. The travel time from the source to the near receiver was adjusted for the delay between the time the signal is given for the test to begin and the time the seismic wave is actually initiated. This adjustment to the source-to-receiver travel time does not need to be made to the receiver-to-receiver travel time because it is the difference between two source-to-receiver travel times and thus automatically adjusts for the factors involved.

Figures VII-1 to VII-16 present plots of suspension seismic shear-wave interval velocities versus depth bgs for each of boreholes RF#13 to RF#29.[5] For boreholes RF#14 to RF#29, two shear-wave velocity plots are presented, one based on the receiver-to-receiver travel time difference, and the other based on the source-to-near receiver travel time difference. The receiver-to-receiver velocity is plotted against the average of the depths bgs of the two receivers, while the source-to-near receiver velocity is plotted against the average of the depths bgs of the source and the near receiver. The shear-wave velocities derived from the downhole seismic measurements (discussed in Section 6.2.5) at the same borehole and the SASW velocity profile(s) for a survey located near the borehole (discussed in Section 6.2.7) are also shown for reference. For the downhole profiles, see DTNs: MO0111DVDWHBSC.001, MO0110DVDBOREH.000 and MO020498DNHOLE.000; and for the SASW profiles, see DTN: MO0110SASWWHBS.000.

The shear-wave interval velocity data from boreholes RF#13 to RF#29 were examined statistically in two ways. First, the data acquired at 0.5-meter intervals were divided into 1.5-meter (4.92 feet) sets and the mean, median, mean plus one standard deviation and mean minus one standard deviation was calculated for each set. The 1.5-meter depth increment was chosen to be similar to the 5-foot increment used for the downhole statistics discussed in Section 6.2.5.3. The results of this analysis are shown on Figures 30 (receiver-to-receiver) and 31 (source-to-receiver). The data were also divided according to lithostratigraphic unit and the same statistical parameters were calculated. The median, mean plus one standard deviation and mean minus one standard deviation are shown on Figures 32 (receiver-to-receiver) and 33 (source-to-receiver). Values of mean, median, standard deviation, and coefficient of variation and count (number of measurements in the data set) by lithostratigraphic unit are summarized in Tables VII-1 (receiver-to-receiver) and VII-2 (source-to-receiver). To facilitate comparisons, Figures VII-49 and VII-50 shows a plot of the averaged v_s for individual boreholes versus depth, together with the mean and mean ± one standard deviation for the entire data set. The number of profiles included in the statistical analysis at each depth interval is indicated in the bar graph along the right edge of the plot. At shallow and deeper depths, few profiles are available to be included in the statistical analysis, and the statistical values may not be meaningful.

---

[5] Throughout Attachments VII and VIII, the surveys performed by Redpath Geophysics are referred to as the 2000-1 surveys, the surveys performed by GEOVision Inc. (RF#13 and RF#17) are referred to as the 2000-2 surveys, and the survey performed by URS Corporation (RF#13) is referred to as the 1998 survey.

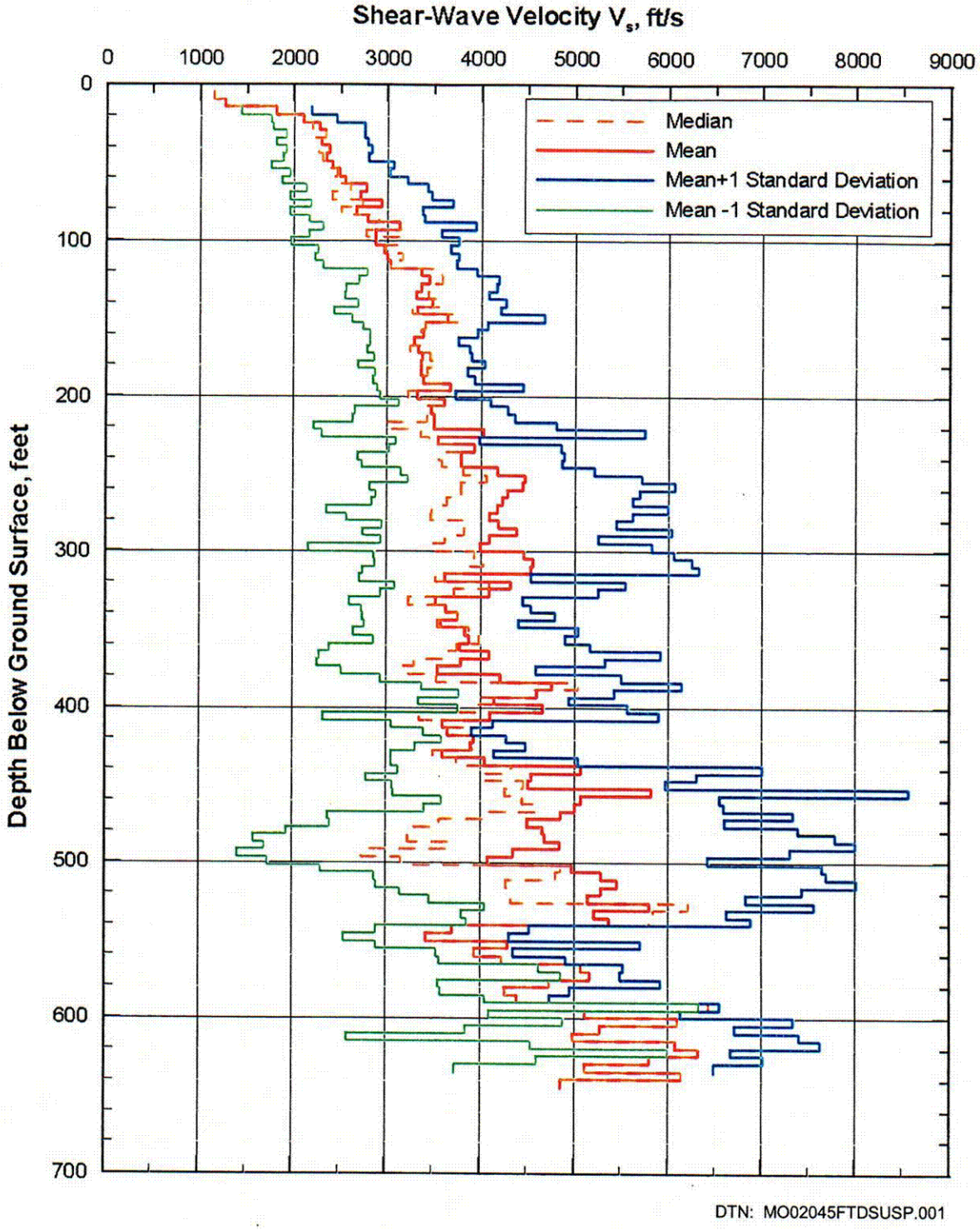

Figure 30. Shear-Wave Velocity by Depth Interval from Receiver-to-Receiver Interval Suspension Surveys in WHB Area

C01

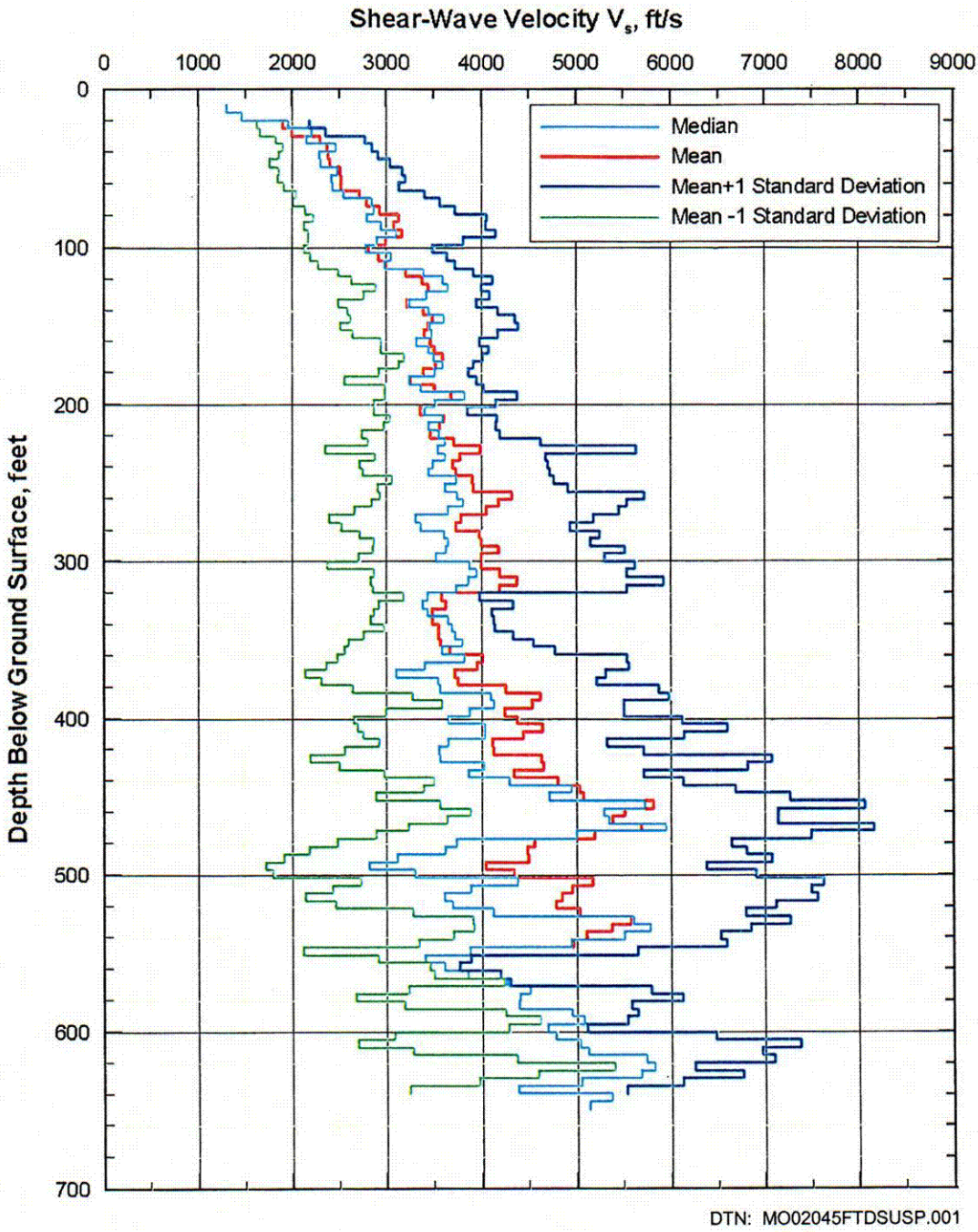

Figure 31. Shear-Wave Velocity by Depth Interval from Source-to-Receiver Interval Suspension Surveys in WHB Area

C02

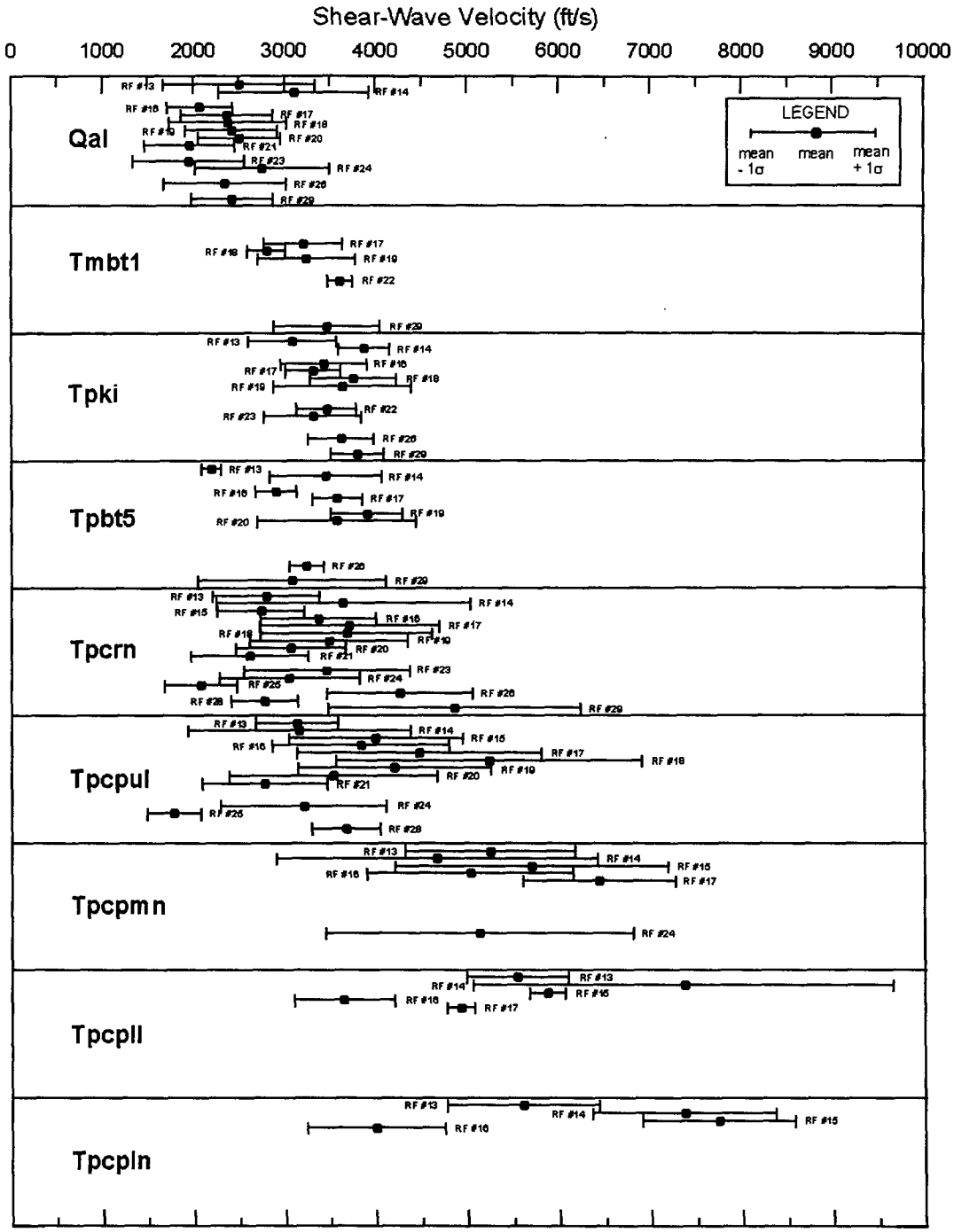

DTN: MO0204SUSPSEIS.001

Figure 32. Statistical Values of Shear-Wave Velocity by Lithostratigraphic Unit from Receiver-to-Receiver Interval Suspension Surveys in WHB Area

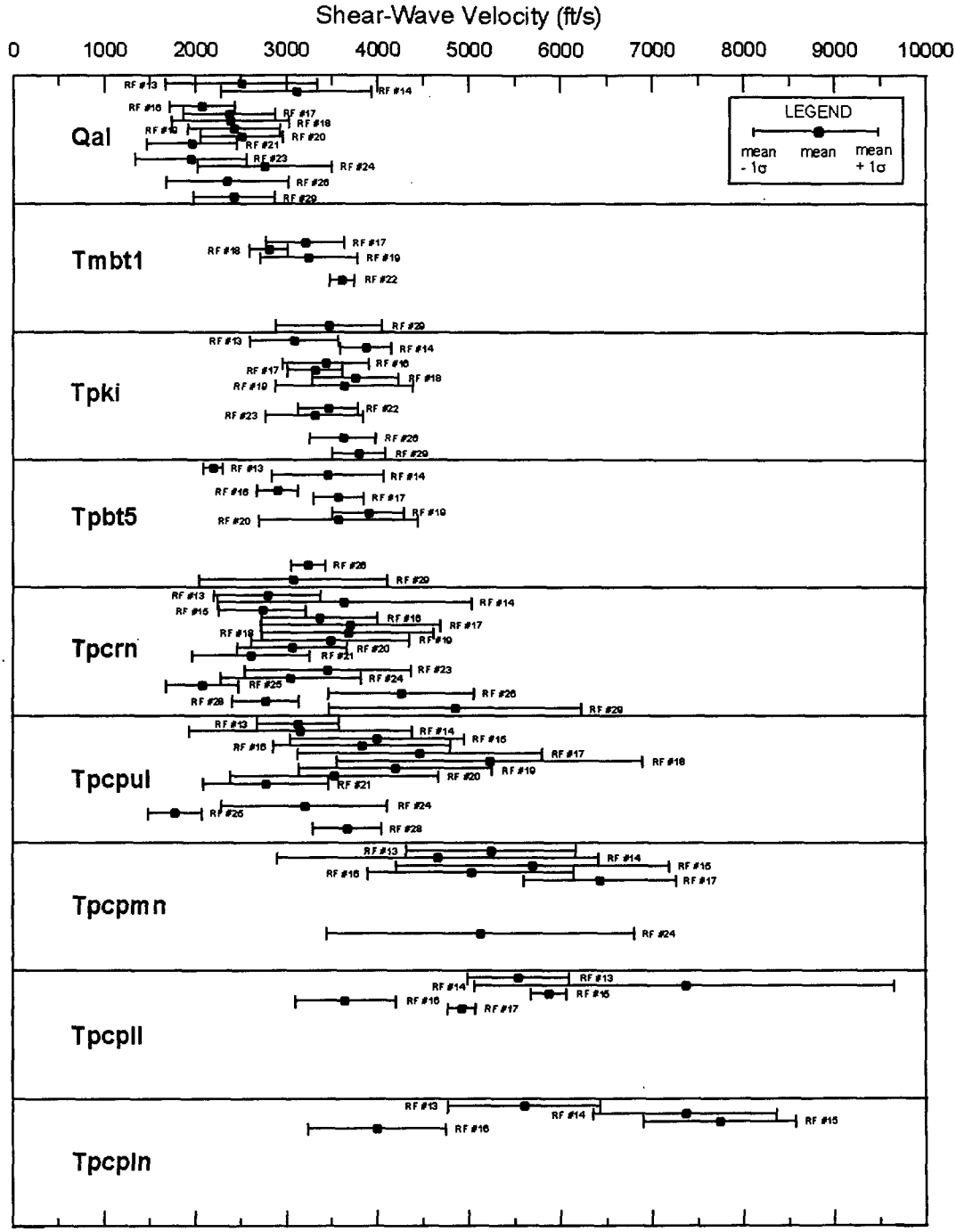

DTN: MO0204SUSPSEIS.001

Figure 33. Statistical Values of Shear-Wave Velocity by Lithostratigraphic Unit from Source-to-Receiver Interval Suspension Surveys in WHB Area

As mentioned in Section 6.2.2, it was estimated prior to drilling the deep boreholes that a shear-wave velocity of 5,000 ft/s rock would be found, based on the downhole results from borehole RF#13, at about 20 to 30 feet into the Tiva Canyon Tuff crystal-poor middle nonlithophysal zone (Tpcpmn). As can be seen from Figures 32 and 33, the mean value of shear-wave velocity is generally above 5,000 ft/s in the Tpcpmn and older zones. Where the shear-wave velocity is less than 5,000 ft/s in the Tpcpmn and older zones, the rock is generally highly fractured or the borehole passed through a zone of fracture fill (see Section 6.6.2 for a discussion of fracture fill). This observation suggests that an improved correlation (lower standard deviation) could be obtained if the velocity statistics were calculated as a function of both lithostratigraphic unit and fracture frequency or RQD. However, such knowledge would seem to have little practical import because the distribution of fractures in the rock is not known.

Figures VII-17 through VII-32 present plots of suspension seismic compression-wave interval velocities versus depth bgs for each of boreholes RF#13 to RF#29.[6] For each borehole two compression-wave velocity plots are presented, one based on the receiver-to-receiver travel time difference, and the other based on the source-to-near receiver travel time difference. The receiver-to-receiver velocity is plotted against the average depth bgs of the two receivers, while the source-to-near receiver velocity is plotted against the average of the depths bgs of the source and the near receiver. The compression-wave velocities derived from the downhole seismic measurements at the same borehole are also shown for reference.

The compression-wave interval velocity data from boreholes RF#14 to RF#29 were examined statistically in the same way as the shear-wave interval velocity data except that only the source-to-receiver data were considered. Receiver-to-receiver data were not considered because much of the data could not be interpreted and because compression-wave velocity is a less important parameter than shear-wave velocity. The statistics by depth interval and by lithostratigraphic unit are shown on Figures 34 and 35, respectively. Table VII-3 summaries values of mean, median, standard deviation, and coefficient of variation and count by lithostratigraphic unit. To facilitate comparisons, Figure VII-51 shows a plot of the averaged v_p for individual boreholes versus depth, together with the mean and mean ± one standard deviation for the entire data set. The number of profiles included in the statistical analysis at each depth interval is indicated in the bar graph along the right edge of the plot. At deeper depths, as well as at very shallow depths, few profiles are available to be included in the statistical analysis, and the statistical values may not be meaningful.

Where both shear-wave and compression-wave velocities are known for the same depth interval, the value of Poisson's ratio was calculated using equation 4 from the theory of elasticity for homogeneous, isotropic elastic materials. Figures VII-33 through VII-48 present plots of Poisson's ratio versus depth bgs derived from the shear- and compression-wave interval velocities measured at each of boreholes RF#13 to RF#29.

---

[6] Note that for borehole RF#13, there are no compression-wave suspension seismic velocity results. However, as will be discussed in Section 6.7.2, velocity and Poisson's ratio results from other methods are presented on the figures in Attachments VII and VIII. Consequently, for consistency of presentation, Figures VII-17 and VII-33 for RF#13 are presented even though they contain no suspension seismic data.

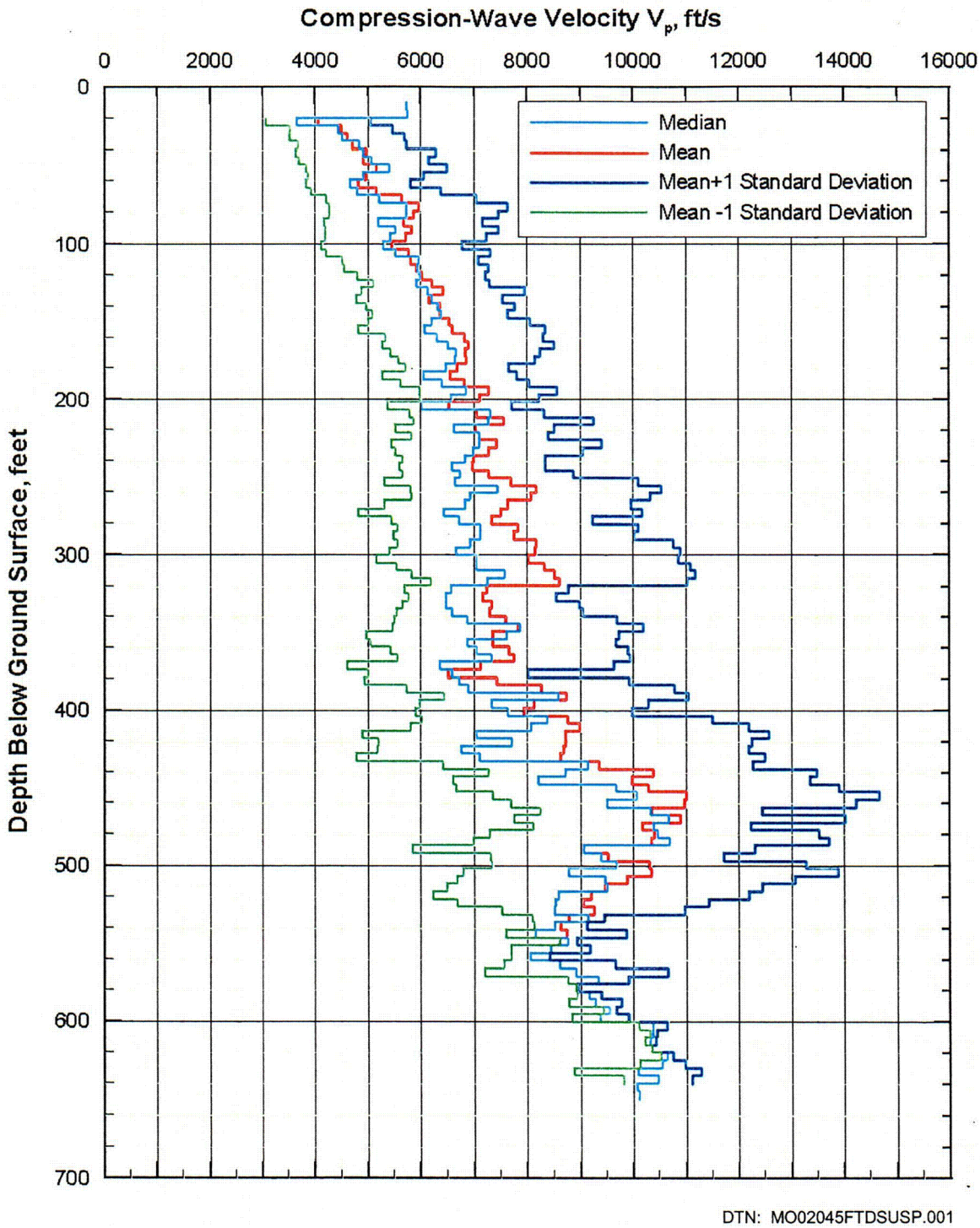

Figure 34. Compression-Wave Velocity by Depth Interval from Source-to-Receiver Interval Suspension Surveys in WHB Area

C03

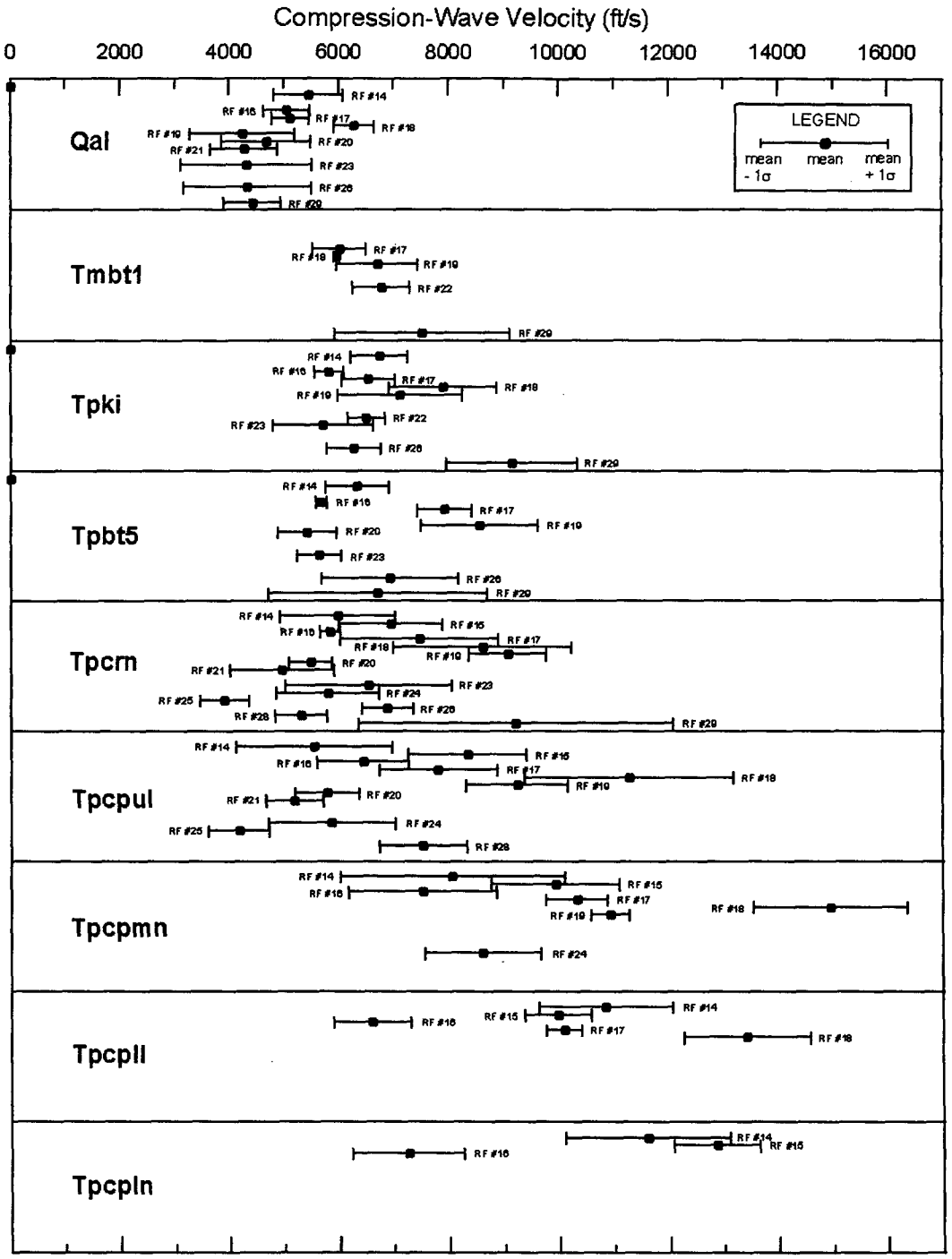

DTN: MO0204SUSPSEIS.001

Figure 35. Statistical Values of Compression-Wave Velocity by Lithostratigraphic Unit from Source-to-Receiver Interval Suspension Surveys in WHB Area

The Poisson's ratio data from boreholes RF#14 to RF#29 were examined statistically in the same way as the shear- and compression-wave interval velocity data. Again, only source-to-receiver data was considered. Figures 36 and 37 show statistics by depth interval and by lithostratigraphic unit, respectively. Table VII-4 summarizes values of mean, median, standard deviation, and coefficient of variation and count by lithostratigraphic unit. To facilitate comparisons, Figure VII-52 shows a plot of Poisson's ratio calculated from the average values of v_s and v_p for individual boreholes versus depth, together with the mean and mean ± one standard deviation for the entire data set. The number of profiles included in the statistical analysis at each depth interval is indicated in the bar graph along the right edge of the plot. At deeper depths, as well as at very shallow depths, few profiles are available to be included in the statistical analysis, and the statistical values may not be meaningful.

For this scientific analysis, the shear-wave travel times for each suspension seismic interval were accumulated to construct a plot of accumulated shear-wave arrival times versus depth bgs. This plot is the same in form as the adjusted shear-wave travel time versus depth plot from a downhole seismic survey. However, it should be noted that in the suspension method, the seismic waves are constrained to travelling in the relatively limited volume of material in the immediate vicinity of the direct path between the source and the receivers, while in the downhole method a greater potential exists for the seismic waves to deviate from a straight-line path from source to receiver. Plots of these results are presented as Figures VIII-1 through VIII-16.[7] The downhole adjusted travel times are also plotted for comparison, which is discussed in Section 6.7. As was discussed in Section 6.2.5 relative to the downhole seismic travel time versus depth bgs data, the results plotted on Figures VIII-1 through VIII-16 were evaluated by fitting straight lines to the data in depth intervals where the data suggested a zone of relatively constant velocity when viewed on a macroscale. The seismic velocity was then computed as the first derivative of depth with respect to time and noted on the appropriate figure. All of the resultant shear-wave velocities are plotted on Figure 38. These velocities are referred to as "linear approximations" herein and are also plotted on the graphs in Attachment VII.

Compression-wave arrival times were also accumulated with depth bgs and are shown on Figures VIII-1 through VIII-16. Linear functions were fitted to the accumulated arrival time plots and average compression-wave velocities were computed (DTNs: MO0204SEPFDSSS.000, MO0204SEPSWSSS.000). All of the resultant shear-wave velocities are plotted on Figure 39.

Poisson's ratio was calculated from the average shear-wave velocities and average compression-wave velocities on Figures 38 and 39. The resultant values of Poisson's ratio are plotted on Figure 40 for all the surveys as well as on each of Figures VII-33 through -48.

---

[7] Note that the travel time from ground surface to the suspension result at the shallowest depth is unknown and must be assigned arbitrarily. Because the travel time from ground surface to the shallowest suspension result is unknown, velocity cannot be assessed in this interval using the suspension results. In some cases, the records of measurements could not be interpreted and these create a gap in the accumulated travel time plot. In general, the downhole results were used to assign a travel time to the shallowest measurement and to shallowest measurement after a gap in the data. Other approaches could be taken, but this approach facilitates comparison of the suspension seismic and downhole seismic data. Note that these assigned travel time values only move the curve laterally on the graph and do not affect the shape or slope of the curve, which means they do not affect the interpreted velocity.

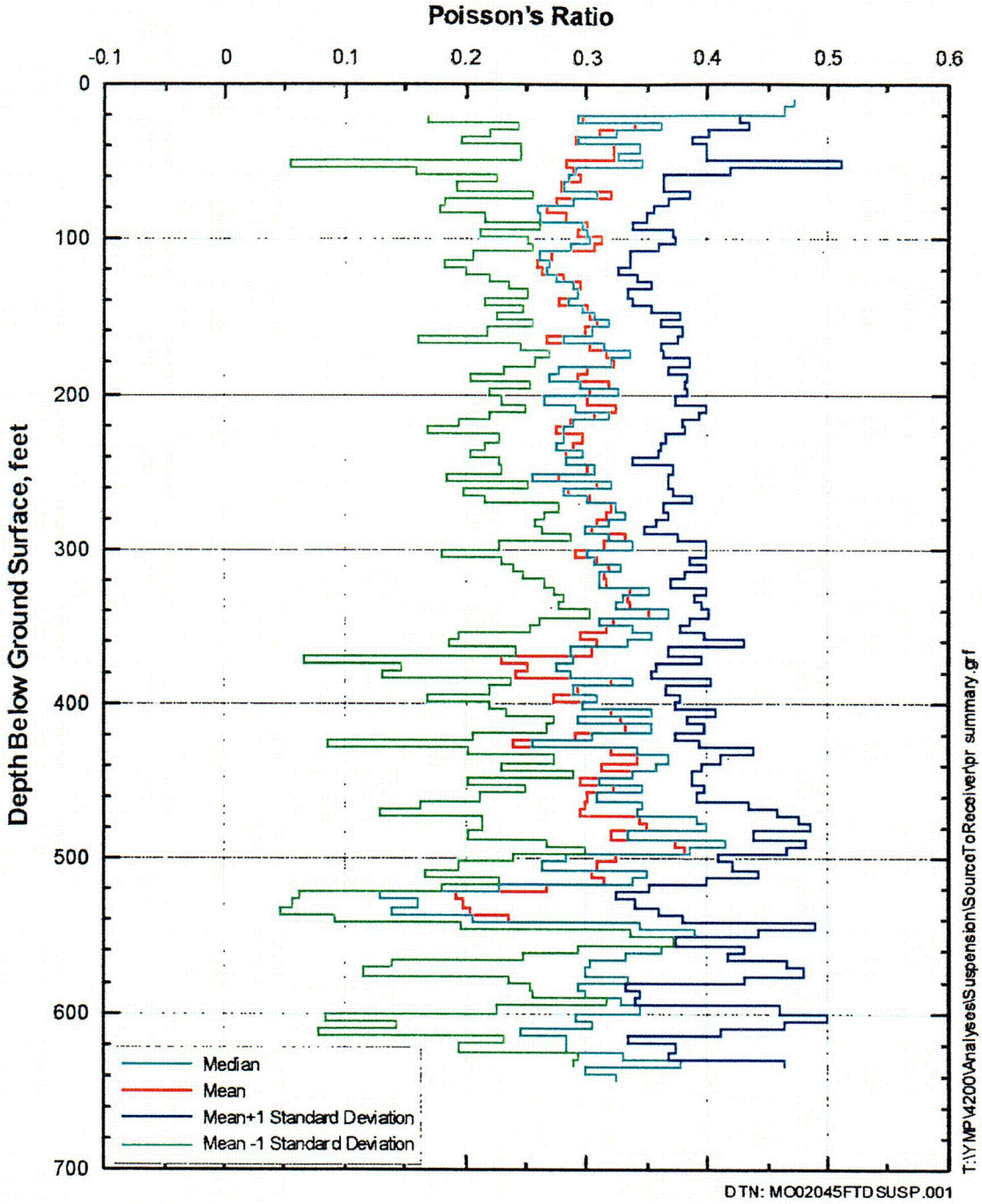

Figure 36. Poisson's Ratio by Depth Interval from Source-to-Receiver Interval Suspension Surveys in WHB Area

C04

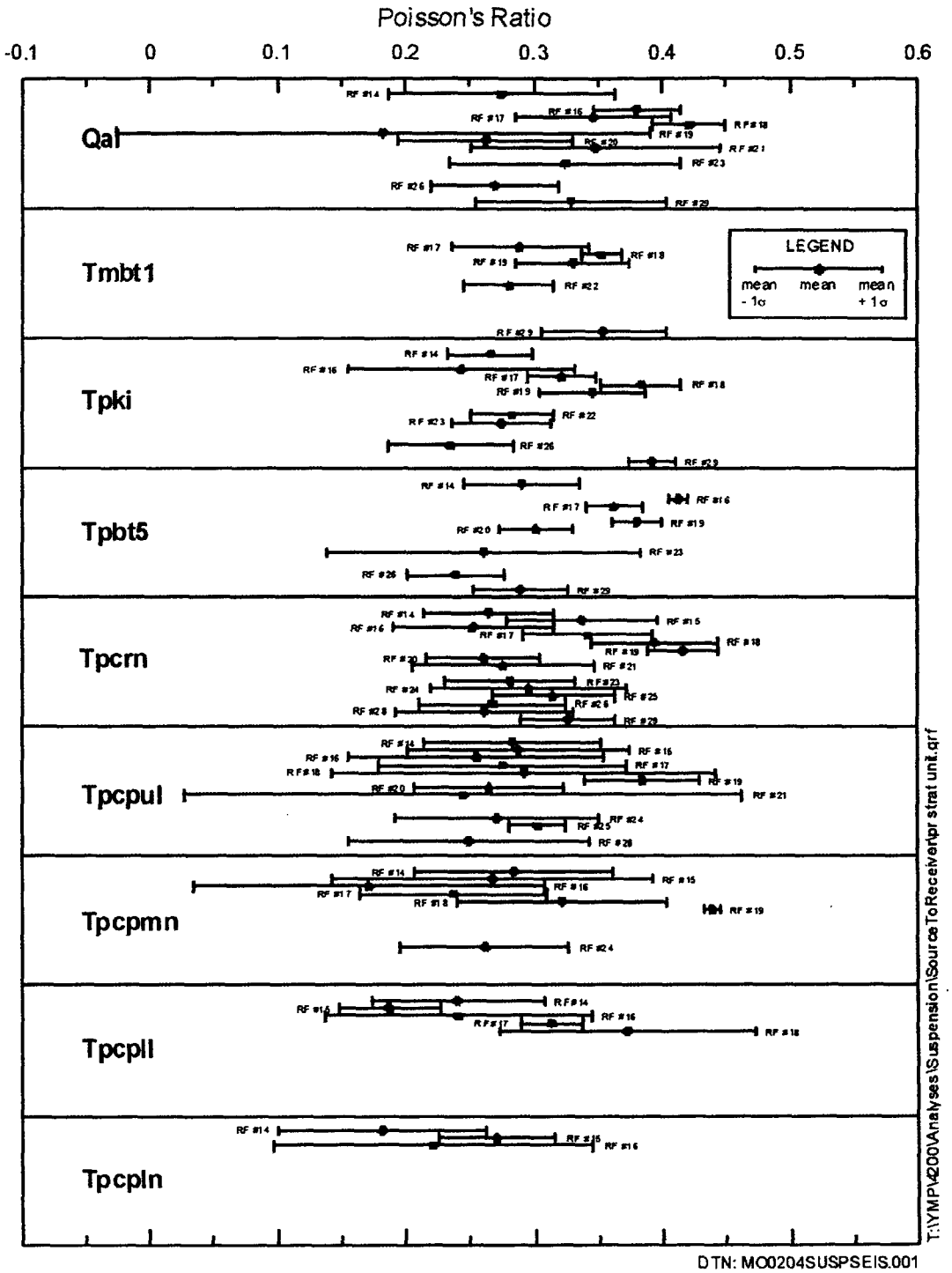

Figure 37. Statistical Values of Poisson's Ratio by Lithostratigraphic Unit for Poisson's Ratio from Source-to-Receiver Interval Suspension Surveys in WHB Area

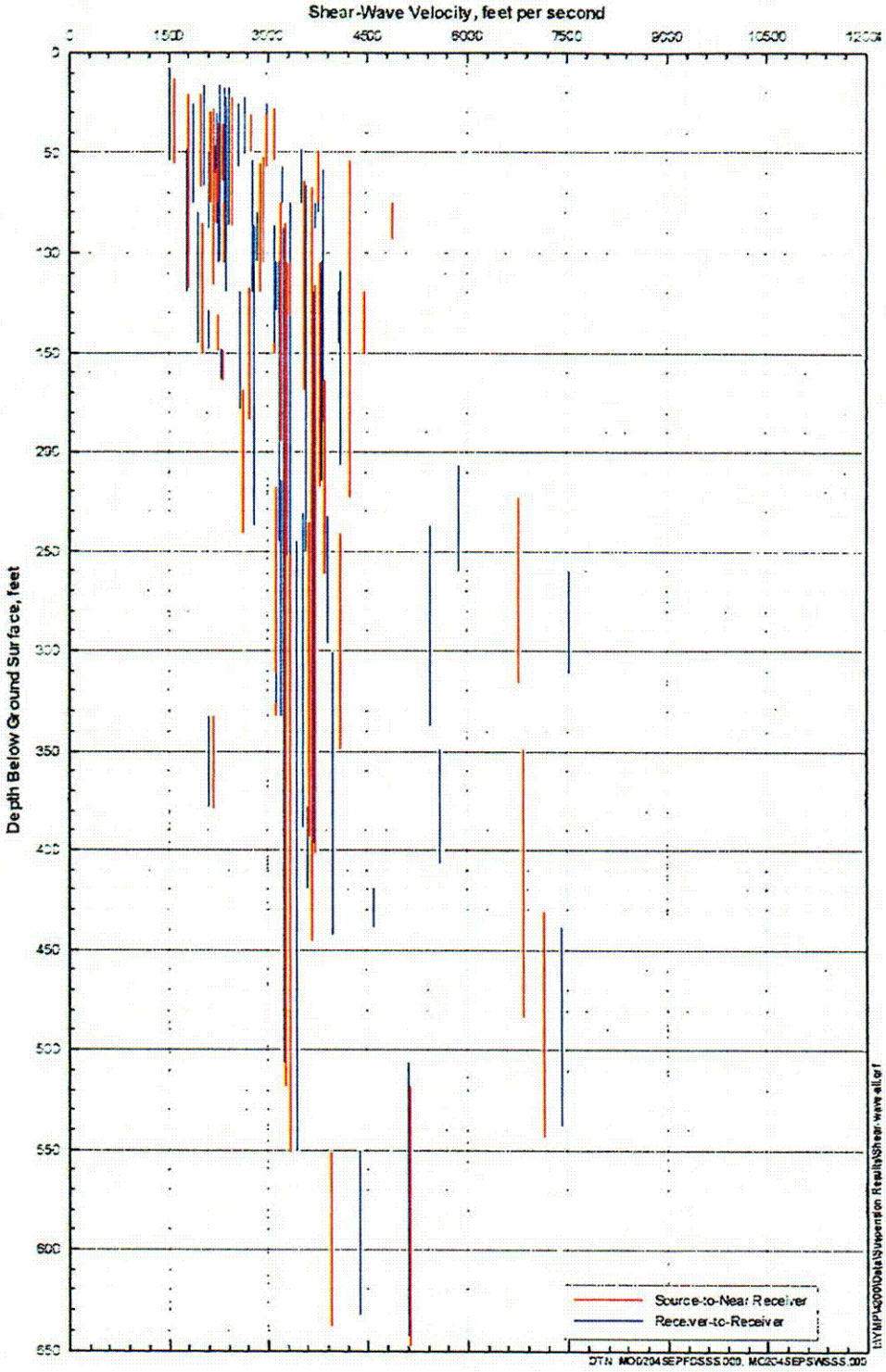

Figure 38. Shear-Wave Velocities from Linear Fits to Suspension Seismic Time Data

C05

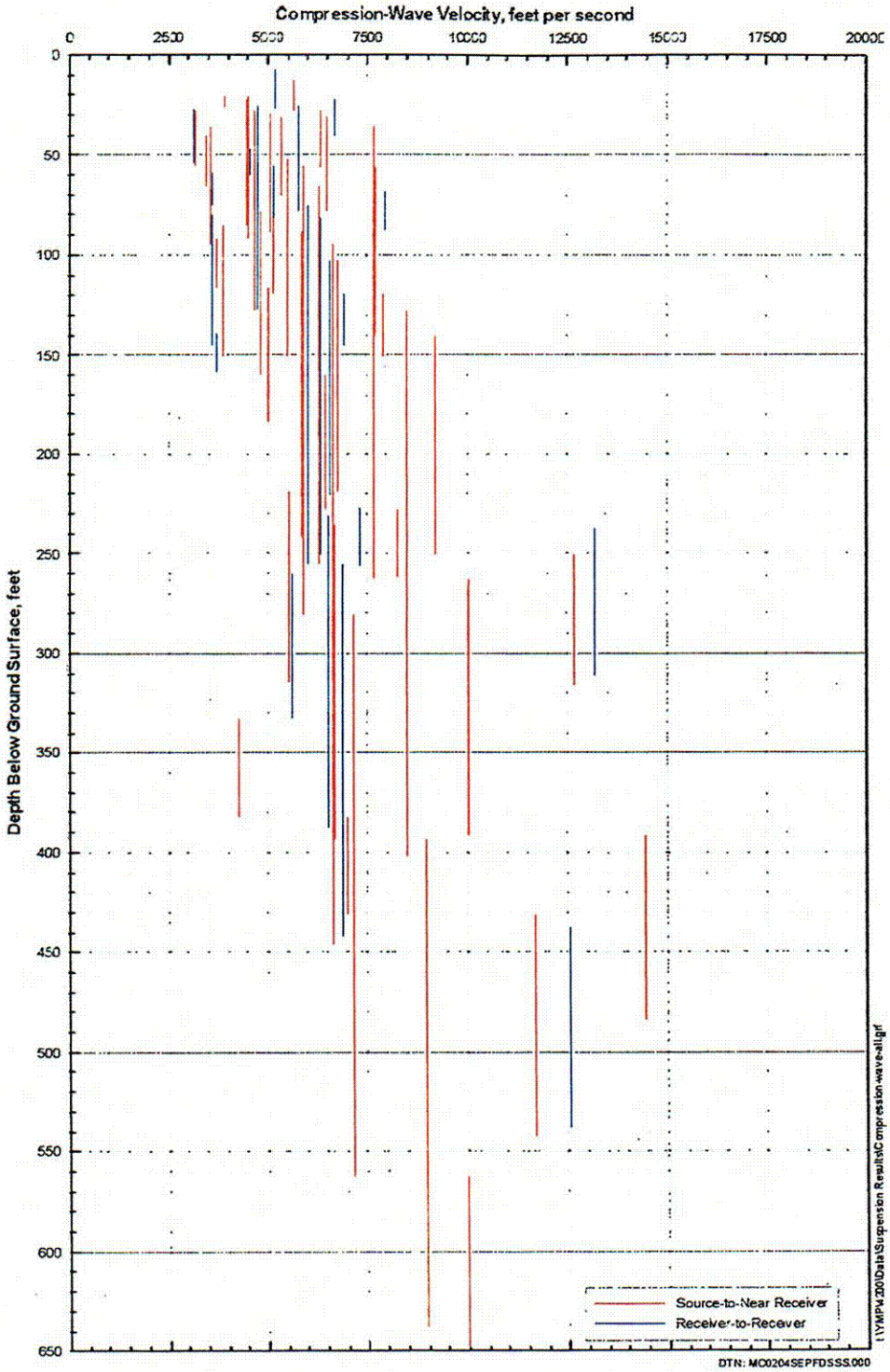

Figure 39. Compression-Wave Velocities from Linear Fits to Suspension Seismic Time Data

C06

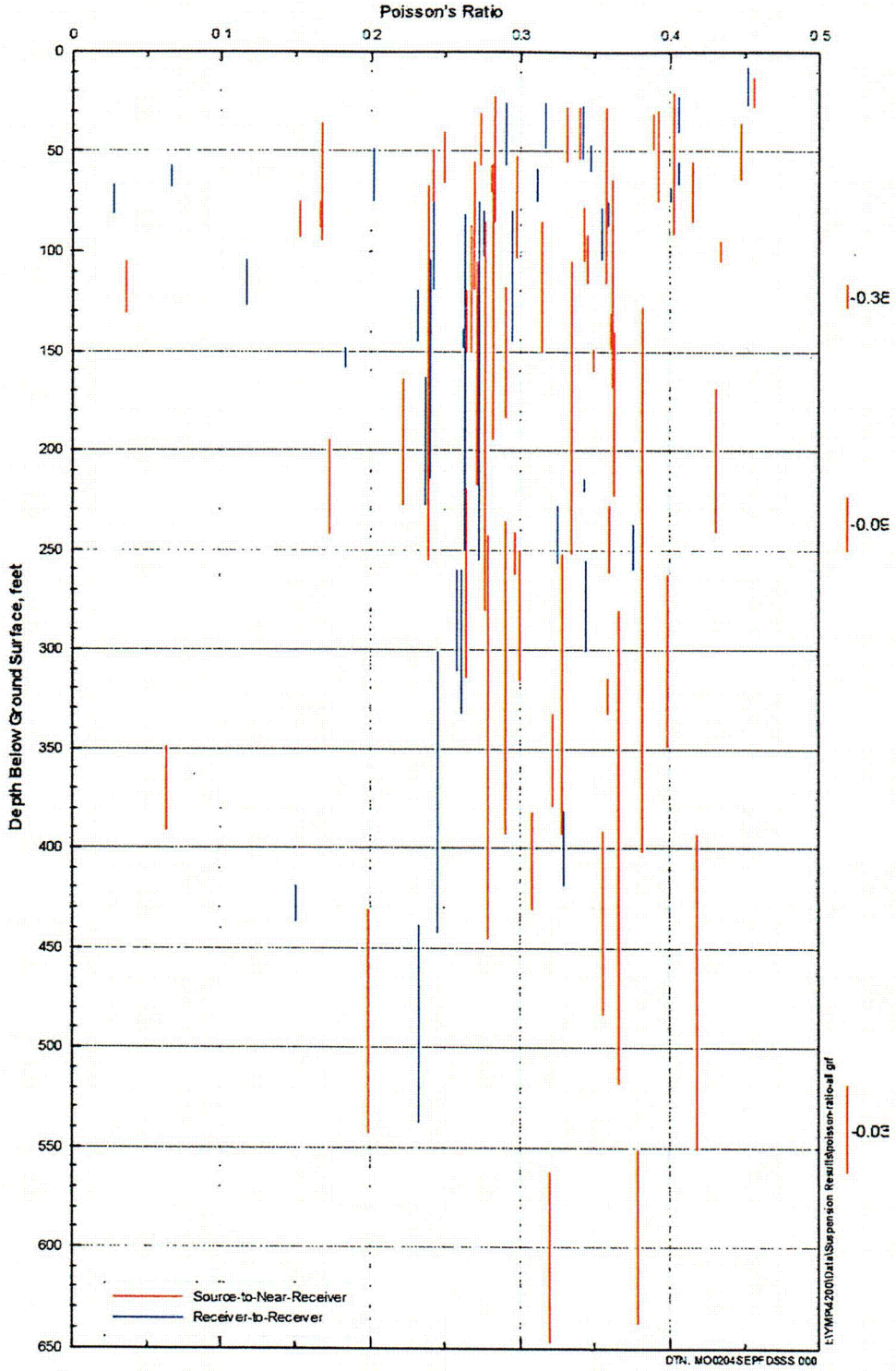

Figure 40. Poisson's Ratio from Linear Fits to Suspension Seismic Time Data

C07

Although natural soil and rock deposits are not homogeneous, isotropic or elastic, at shear strain levels less than about 10^{-4} to 10^{-6} (depending on the particular material), earth materials appear to behave elastically, which is sometimes referred to as pseudo-elastic behavior. Seismic geophysical methods typically involve strain levels less than this threshold strain value, and are considered to reflect behavior in the pseudo-elastic range. Thus, it is generally expected that the v_s and v_p interpreted at a given location (depth and borehole) will yield a value of Poisson's ratio in the range 0.00 to 0.50 associated with homogeneous, isotropic, elastic materials.

As shown on Figures 40 and VII-33 through -48, the values of Poisson's ratio derived from the interval velocities occasionally lie outside the range 0.00 to 0.50 associated with homogeneous, isotropic, elastic materials. All of the values outside the range 0.00 to 0.50 are negative, which means $v_p < \sqrt{2}\, v_s$, and most are between 0.00 and -0.10. However, the total number of values outside the range 0.00 to 0.50 is only a small fraction of the total number of values, which indicates that overall the velocities yield reasonable values of Poisson's ratio. As for the values of Poisson's ratio derived from the layer-average velocities, there are some intervals, generally short, where Poisson's ratio falls outside the range 0.00 to 0.50. Again, the values are always negative. These values are in every case the result of selecting different layer boundaries for the v_s and v_p profiles and can be ignored.

6.2.7 SASW Surveys

SASW surveys were performed at the proposed site of the WHB in the summers 2000 and 2001 by a team from the University of Texas at Austin (UTA) led by Dr. Kenneth H. Stokoe, II. The majority of the SASW surveys were performed from 24 July through 6 August 2000. Three additional sites were tested on 16 September 2000. A single survey, D-12, was performed in July 2001. This work was performed and documented through the use of Scientific Notebooks SN-M&O-SCI-022-V1 (Wong 2002c) and SN-M&O-SCI-040-V1 (Wong 2002a).

The objective of these investigations was to estimate the shear-wave velocity structure to a depth of approximately 150 ft at closely-spaced intervals on and near the proposed footprint of the WHB Area. A total of 35 shear-wave velocity profiles were developed. This section describes the SASW measurements, analysis procedures and the results.

6.2.7.1 Methodology

The SASW methodology is a non-destructive and non-intrusive seismic method. It utilizes the dispersive nature of Rayleigh-type surface waves propagating through a layered material to estimate the shear-wave velocity profile of the material (Stokoe, Wright et al. 1994). In this context, dispersion arises when surface-wave velocity varies with wavelength or frequency. Dispersion in surface-wave velocity arises from changing stiffness properties of the soil and rock layers with depth. This phenomenon is illustrated on Figure 41 for a multi-layered solid. A high-frequency surface wave, which propagates with a short wavelength, only stresses material near the exposed Layer 2 ıd thus only samples the properties of the shallow, near-surface material (Figure 41b). A lower-frequency surface wave, which has a longer wavelength, stresses material to a greater depth and thus samples the properties of both shallower and deeper materials (Figure 41c). Spectral analysis is used to separate the waves by frequency and wavelength to dete Layer 3 experimental ("field") dispersion curve for the site. An analytical

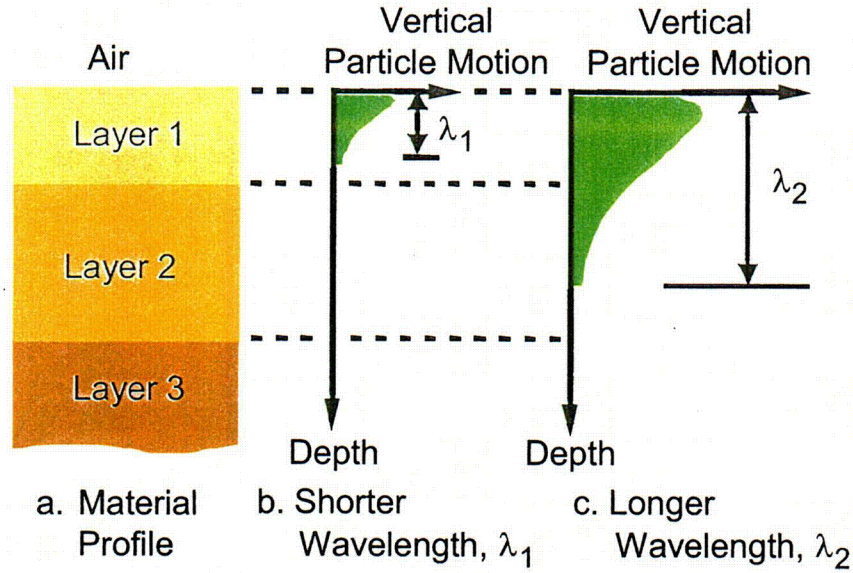

Figure 41. Illustration of Surface Waves with Different Wavelengths Sampling Different Materials in a Layered System which Results in Dispersion in Wave Velocities

theoretically match the field dispersion curve with a one-dimensional layered system of varying layer stiffnesses and thicknesses (Joh 1996). The one-dimensional shear-wave velocity profile that generates a dispersion curve which matches the field dispersion curve is presented as the profile at the site.

SASW measurements involve generating surface waves at one point on the ground surface and recording them as they pass by two or more locations. All measurement points are arranged along a single radial path from the source. Successively longer spacings between the receivers and between the source and first receiver are typically used to measure progressively longer wavelengths. This general configuration for one source/receiver set-up is illustrated on Figure 42. The distance between the source and first receiver (d) is kept equal to the distance between receivers. Measurements are performed with several (typically 7 or more) sets of source-receiver spacings. Phase plots from surface wave propagation between the receivers are recorded for each receiver spacing. From each phase plot, the phase velocity of the surface wave can be calculated at each frequency from (Joh 1996, p. 20):

$$V_R = f \cdot \frac{360}{\phi} \cdot d \qquad \text{(Eq. 5)}$$

where V_R is the phase velocity in ft/s or m/s, f is the frequency in Hertz (cycles per sec), ϕ is the phase angle in degrees (at frequency f), and d is the distance between the receivers in the same length units as used to represent V_R. From this calculation, a plot of phase velocity versus frequency, called an individual dispersion curve, is generated.

C08

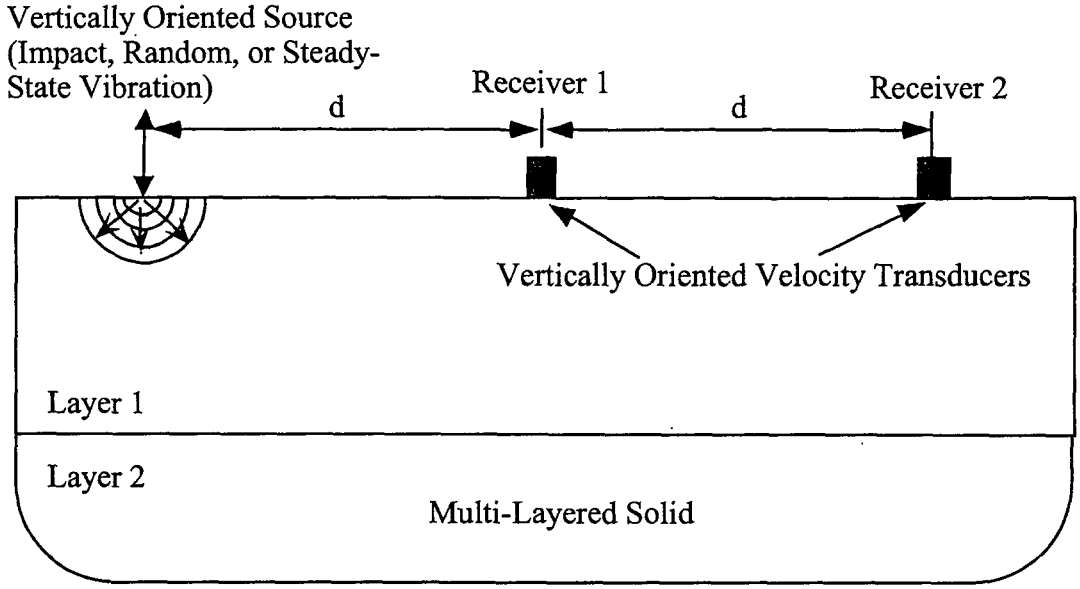

Figure 42. Schematic Diagram of the Generalized Equipment Arrangement Used for SASW Measurements

This procedure is repeated for all source-receiver spacings used at the site and typically involves significant overlapping in the dispersion data between adjacent receiver sets. The individual dispersion curves from all receiver spacings are combined into a single composite dispersion curve called the experimental or field dispersion curve. Once the composite dispersion curve is generated for the site, an iterative forward modeling procedure is used to create a theoretical dispersion curve to match this experimental curve (Joh 1996). The stiffness profile that provides the best match to the experimental dispersion curve is presented as the shear-wave velocity profile at the site.

6.2.7.2 Approach

A total of 40 SASW surveys were performed in the area of the proposed WHB. Their locations are shown on Figure 43. The lengths of the lines are drawn approximately equal to the maximum receiver spacing along SASW survey. To the extent possible, at least one line was laid out near every borehole to allow comparison of the SASW results with the downhole velocity measurements. The majority of the surveys were laid out approximately along strike of the bedding at the WHB to minimize possible 2- and 3-dimensional variations in the velocity structure. A single survey, D-12, was performed across a lower portion of Exile Hill (Figure 43).

Five of the surveys were combined with other adjacent surveys (SASW-8a+8; SASW-9a+9; SASW-10+37, SASW-32+35, and SASW-34+36) resulting in 35 experimental dispersion curves. A total of 35 shear-wave velocity profiles was thus generated within the WHB Area. The locations of these arrays referenced to other landmarks are presented in the Supplement Records of the Scientific Notebook SN-M&O-SCI-022-V1 (Wong 2002c, Appendices 1-34).

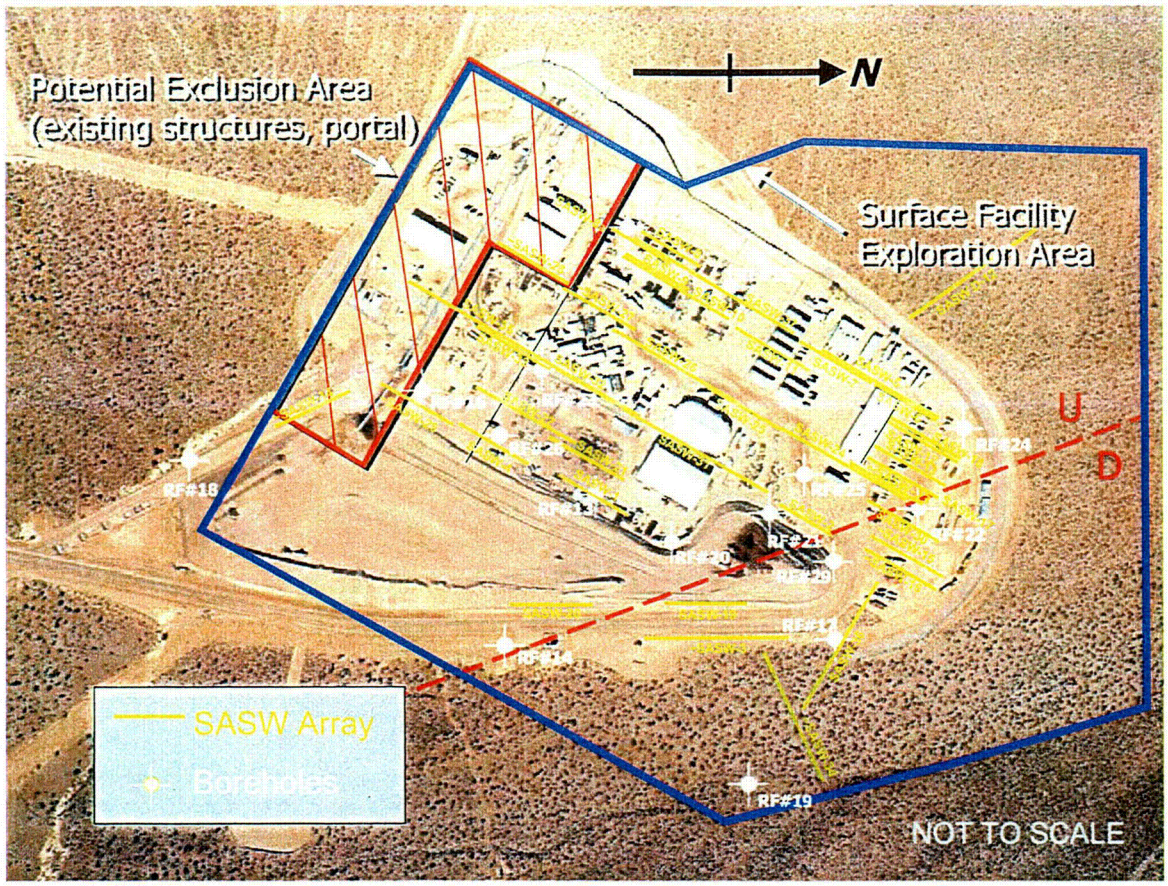

Note: The dashed line is the Exile Hill fault splay.

Figure 43. Locations of SASW Lines at the WHB Site Characterization Area

6.2.7.2.1 Equipment and Measurement Procedures

The basic configuration of the source and receivers used in each survey is illustrated on Figure 42. Vertical-component velocity transducers were used as receivers. The majority of the tests were conducted with Mark Products Model L-4C seismometers, which have a natural frequency of 1 Hz. Key characteristics of these receivers are: 1) they have significant output over the measurement frequency range of 2 to 300 Hz; 2) they are matched so that any differences in phase are negligible over the measurement frequency range; 3) they couple well to the ground; and 4) the coupling is similar for each receiver. These 1-Hz seismometers have outputs in excess of 10 volts/(in/sec) and phase shifts between receivers of less than 3.6 degrees for frequencies from 2 to 300 Hz. All equipment calibrations and procedures are presented in Scientific Notebook SN-M&O-SCI-022-V1 (Wong 2002c, Appendix 39).

The preferred arrangement of the receivers for each SASW survey is called a common receivers-midpoint geometry. This arrangement is illustrated on Figure 44. In this arrangement, the two receivers are located equidistant from an imaginary centerline of the survey, which is kept fixed. Due to limited space and numerous physical obstacles at the WHB site, it was not possible in many cases to use the common midpoint geometry. In these situations, a common source

C09

location was employed where the source location was kept constant and the receivers were moved away from the source. Additionally, at each spacing, SASW measurements are ideally performed with the source located first on one end of the survey and then repeated with the source moved to the opposite end of the survey (termed forward and reverse directions). If sound data are recorded in both directions, the cross-power spectra can be combined to eliminate any differences in receiver phase shifts or receiver coupling. Space limitations and numerous obstacles at the WHB limited the ability to perform forward and reverse testing at all spacings. Therefore, in some situations only one direction was recorded. Performing the survey in only one direction had an insignificant effect on the results because the receivers had already been shown to be well matched, and any differences in receiver-to-ground coupling were insignificant.

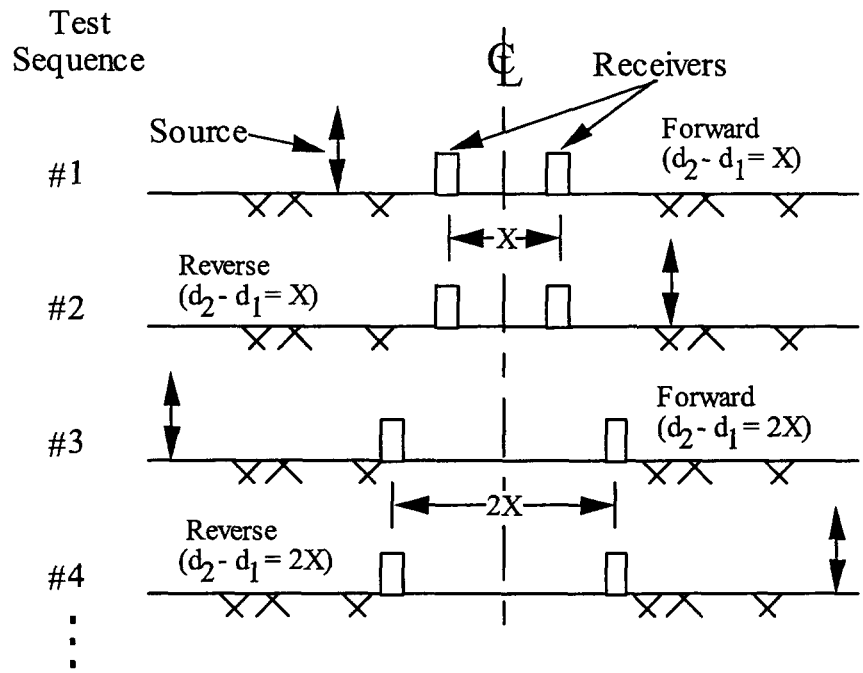

Figure 44. Common Receivers-Midpoint Geometry Often Used in SASW Surveys

Surveys were performed at a series of increasing spacings. Distances between receivers of 3, 6, 12, 25, 50, 100, and 200 ft were typically used to evaluate velocity profiles to depths on the order of 150 ft. The exact receiver spacings used at each site can be found on the data sheets presented in the Supplemental Records to Scientific Notebooks SN-M&O-SCI-022-V1 (Wong 2002c) and SN-M&O-SCI-040-V1 (Wong 2002a). The number and progression of receiver spacings resulted in extensive overlapping of individual dispersion curves used to develop the composite field curve which enhanced the reliability of the measurements.

Several types of sources were used to generate energy over the required frequency ranges. At the shortest receiver spacings (typically 3 and 6 ft), a hand-held geology hammer was used to impact the ground. At larger receiver spacings (typically 12 and 25 ft), a sledgehammer was employed (Figure 45). For receiver spacings equal to and greater than 25 ft, a bulldozer was

used by operating it back and forth over a distance of several meters. This arrangement with the bulldozer as the source is shown on Figures 46 and 47. Generally, when the bulldozer was used, measurements were performed in only the forward direction due to the limitations mentioned previously.

Figure 45. Using the Sledgehammer Source at SASW-23

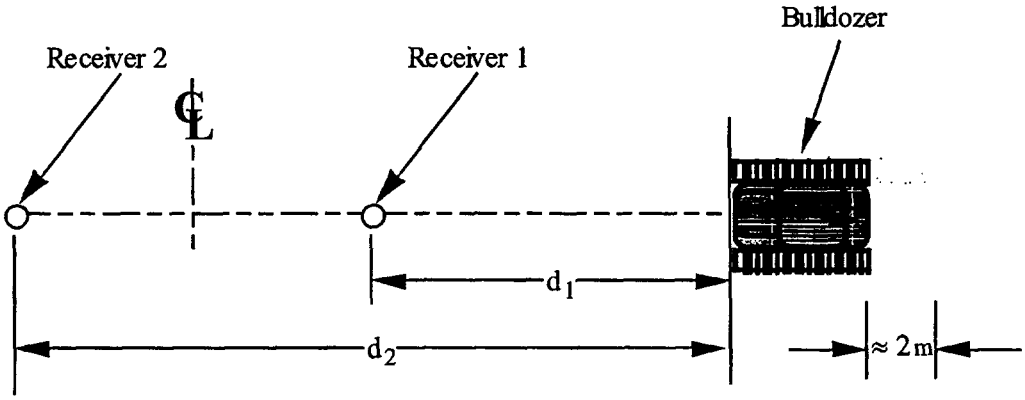

Figure 46. SASW Survey Set-Up Using the Bulldozer as a Wave Source

Figure 47. Bulldozer Source in Operation at SASW-32

At three sites (SASW-35, 36, and 37), deep profiling was performed using a Vibroseis truck as the source of the surface wave energy. As with the bulldozer, surveys were performed only in one direction with this large source. At one of these sites, receiver spacings up to 650 ft were used, generating dispersion curves with a maximum wavelength on the order of 1,000 ft. The dispersion curves from these deep surveys were combined with the shallower dispersion curves from nearby sites (SASW-10+37, 32+35, and 34+36).

The recording device used in the SASW surveys was a Hewlett-Packard 3562A Dynamic Signal Analyzer. The dynamic signal analyzer was used to collect the time records and to perform calculations in the frequency domain so that the relative phase of the cross-power spectrum (discussed below) was reviewed at each receiver spacing. This process also allowed the operator to subjectively evaluate the data being collected in the field to assure consistency with the expected Rayleigh wave propagation in a layered halfspace.

6.2.7.2.2 Calculations

The dynamic signal analyzer was used to measure time-domain records (x[t] and y[t]) from the two receivers at each receiver spacing. These time records were then transformed into the frequency domain (X [f] and Y [f]) and used to calculate the power spectra (G_{XX} and G_{YY}), the cross spectrum (G_{XY}), and the coherence function (γ^2). Expressions for these quantities are (Joh 1996, p. 32):

$$G_{XX} = X^*(f) \cdot X(f) \qquad \text{(Eq. 6)}$$

$$G_{YY} = Y^*(f) \cdot Y(f) \quad \text{(Eq. 7)}$$

$$G_{XY} = X^*(f) \cdot Y(f) \quad \text{(Eq. 8)}$$

$$\phi(f) = \arctan\left[\frac{\mathrm{Im}(G_{XY})}{\mathrm{Re}(G_{XY})}\right] \quad \text{(Eq. 9)}$$

$$\gamma^2(f) = \frac{|G_{XY}(f)|^2}{G_{XX}(f) \cdot G_{YY}(f)} \quad \text{(Eq. 10)}$$

where $G_{XY}(f) = \frac{1}{N}\sum_{i=1}^{N} X^*(f) \cdot Y_i(f)$ is the cross-power spectrum from coherent signal averaging, (*) represents the complex conjugate of the quantity, Im is the imaginary part of the expression, Re is the real part of the expression, and $\phi(f)$ is the relative phase of the cross-power spectrum.

The relative phase of the cross spectrum $\phi(f)$ is the key spectral quantity in SASW measurements. The coherence function of averaged measurements is also important as an indicator of the quality of the measurement over the monitored frequency range. Low values of coherence indicate a possible decrease in data quality. Typically, 3 to 5 time-domain records were averaged in the determination of the spectral functions when impact sources were used. However, when the bulldozer was used as the source at the larger spacings, 10 to 20 averages were typically taken. The relative phase of the cross spectrum, simply called the phase hereafter, represents the phase difference of the motion at the two receivers. One set of spectral functions was measured for each receiver spacing and measurement direction. All of the phase plots that were used in the interpretation of the data are presented in the Supplemental Records to Scientific Notebooks SN-M&O-SCI-022-V1 (Wong 2002c) and SN-M&O-SCI-040-V1 (Wong 2002a).

As an example, the wrapped phase spectrum and coherence function from one receiver spacing are shown in Figure 48. These data were collected from the 50-ft receiver spacing recorded at SASW-24.

6.2.7.2.3 Data Reduction and Forward Modeling Procedures

The data collected in the field in the form of phase plots and coherence functions were transferred from the field disks to a laptop computer, as discussed in the Supplemental Records to Scientific Notebook SN-M&O-SCI-022-V1 (Wong 2002c, Appendix 37, pages 327-368). The data were then reduced and interpreted using the program WinSASW, developed by Joh (1996). For each receiver spacing, the phase plot and coherence function were loaded into WinSASW. A masking procedure was performed to manually eliminate portions of the data with poor signal quality or portions of the data contaminated by the near-field noise.

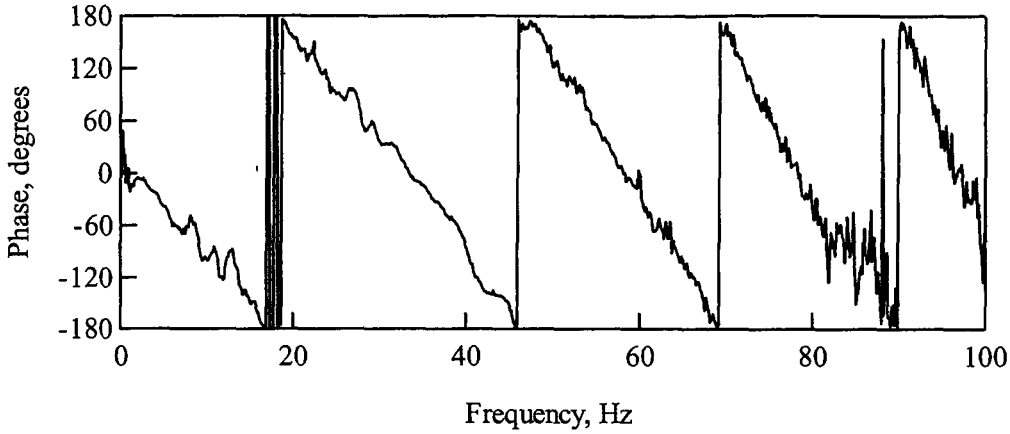

a. Cross-Power Spectrum

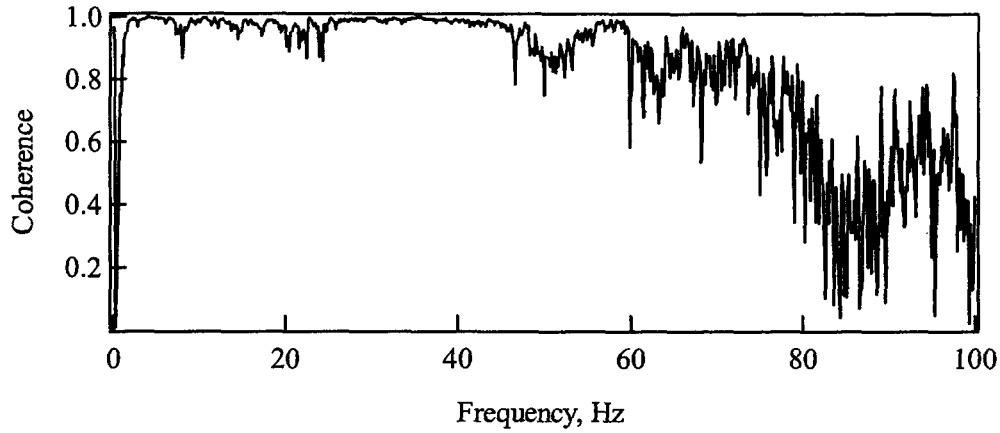

b. Coherence Function

Source: Wong (2002c, Appendix 39, page 437)

Figure 48. Cross-Power Spectrum and Coherence Function Measured at SASW-24 from 50-ft Receiver Spacing

Figure 49 shows the masking applied to the phase plot collected at SASW-24. The masking of every phase plot used in the data analysis at each site is presented in the Supplemental Records to Scientific Notebooks SN-M&O-SCI-022-V1 (Wong 2002c) and SN-M&O-SCI-040-V1 (Wong 2002a). The program uses the masking information to unwrap the phase plot and calculate the dispersion curve using equation 5. Figure 50 shows the individual dispersion curve created from the masking of the phase plot shown on Figure 49. This process was repeated for all receiver spacings resulting in an experimental dispersion curve covering a wide range of wavelengths (typically 1 to 300 ft). Figure 51 shows the composite experimental dispersion curve created at SASW-24.

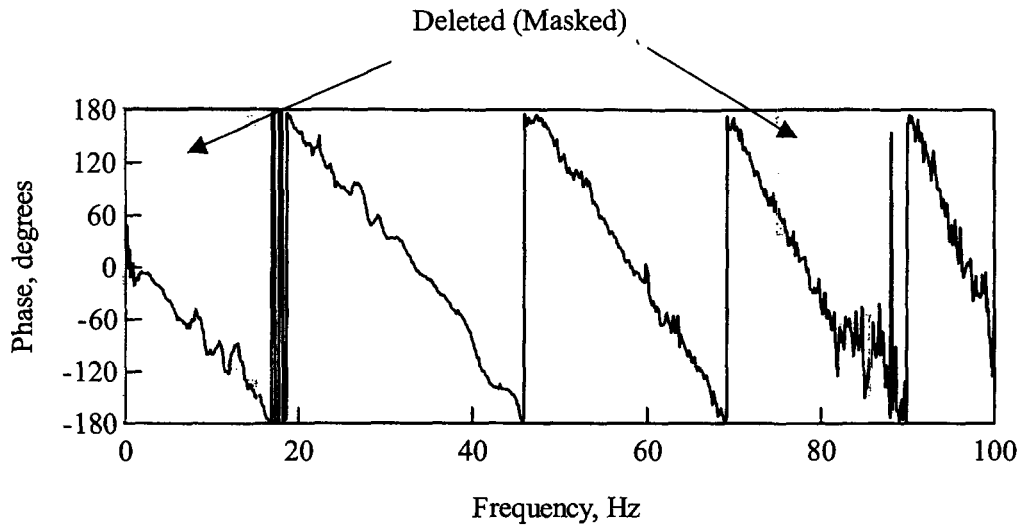

a. Cross-Power Spectrum

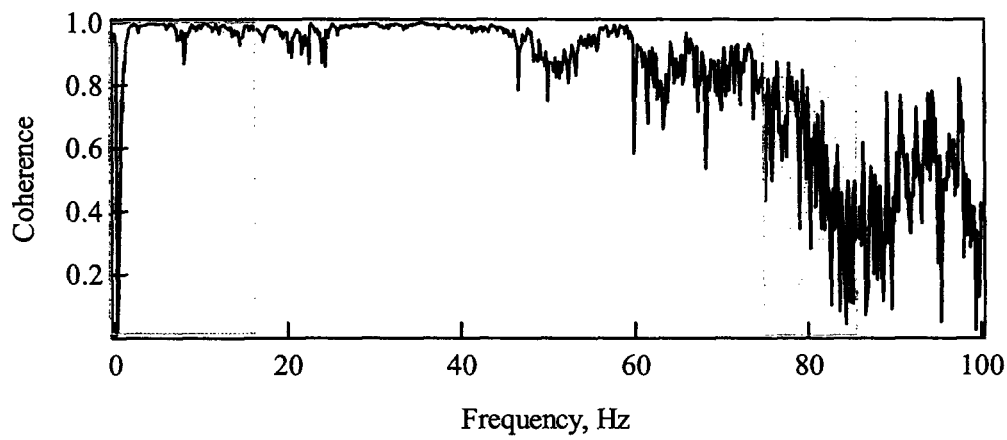

b. Coherence Function

Source: Wong (2002c, Appendix 39, page 438)

Figure 49. Cross-Power Spectrum and Coherence Function Measured at SASW-24 from 50-ft Receiver Spacing Shown with Masking Applied to Near-Field and Low Coherence Regions of the Phase Plot

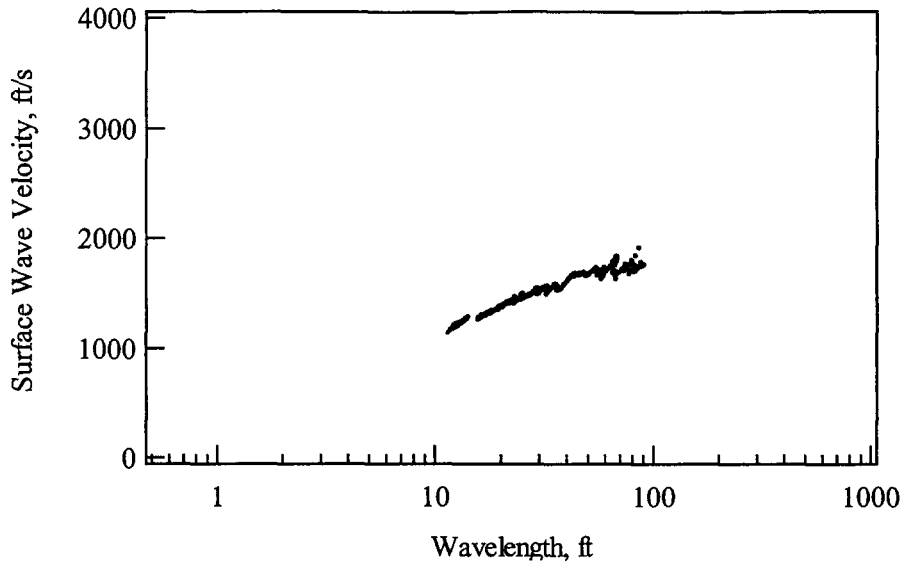

DTN: MO0110SASWWHBS.000

Figure 50. Individual Dispersion Curve Created from 50-ft Receiver Spacing at SASW-24

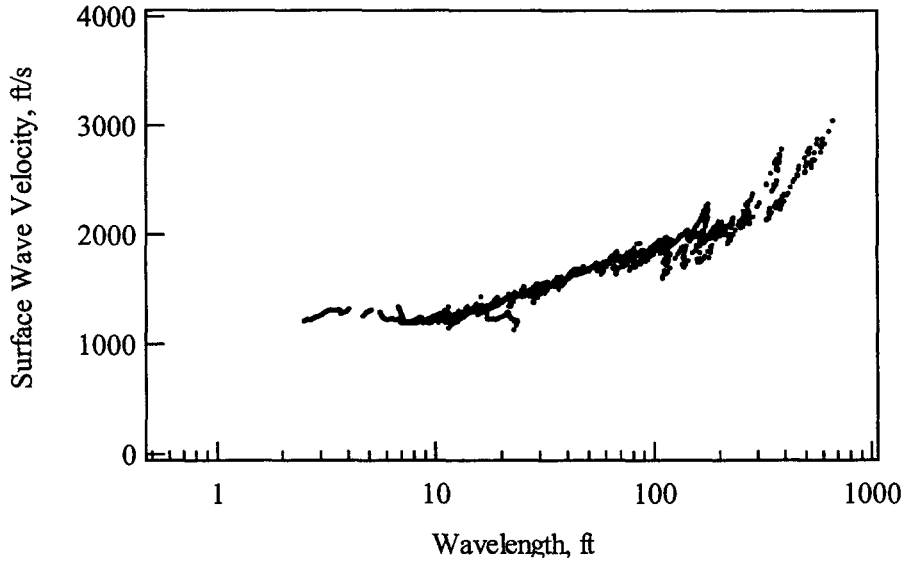

Source: Wong (2002c, Appendix 39, page 439)

Figure 51. Composite Experimental Dispersion Curve Created from All Receiver Spacings at SASW-24

The next step in the data reduction procedure was the creation of the theoretical dispersion curve. The program WinSASW was also used for this purpose. WinSASW uses an algorithm based on a stiffness matrix approach to generate a theoretical dispersion curve for a given shear-wave velocity profile (Kausel and Roesset 1981). The theoretical dispersion curve that is generated can be either the first-mode Rayleigh-wave solution (termed 2D approach) or a complete solution that includes all modes and all other body-wave arrivals (termed 3D approach). For these analyses, the more accurate 3D approach was employed. An initial shear-wave velocity profile was estimated based on the characteristics of the measured experimental dispersion curve. The theoretical dispersion curve was generated and compared to the experimental curve. The shear-wave velocities and layer thicknesses were iteratively changed until an acceptable fit to the experimental curve is achieved. Figure 52 shows the final fit to the composite experimental dispersion curve for SASW-24, and Figure 53 shows the final shear-wave velocity profile.

The theoretical and experimental dispersion curves generated at every site are presented in Attachment IX except for D-12. The D-12 survey was performed as part of the 2001 survey (Section 6.4). For the theoretical analysis, several factors must be considered. First, the density and Poisson's ratio of the material must be estimated. A value of Poisson's ratio of 0.25 was assigned to all materials (Figure 28). When no water table is present, as was the case here, low values of Poisson's ratio (< 0.4) have only a minor influence on the calculated dispersion curve (Brown 1998, Section 7.3.2). The values of unit weight were estimated based on values determined in the laboratory (Section 6.2.10). Thus, a density of 120 lbs/ft^3 was assigned to material with a shear-wave velocity less than 3,000 ft/s, 80 lbs/ft^3 for material between 3,000 and 5,000 ft/s, and 145 lbs/ft^3 for material with a shear-wave velocity equal to or greater than 5,000 ft/s. Relative changes in density with depth affect the dispersion curve, but again the effect on the final shear-wave velocity profile is minor. Therefore, precise knowledge of these values is not required.

Secondly, the theoretical dispersion curve can be generated using different configurations of receiver locations. For these analysis, the theoretical dispersion curve was calculated using a source-to-receiver-1 spacing of two wavelengths and a source-to-receiver-2 spacing of four wavelengths. These receiver locations represent far-field motions. Past studies have shown that the range in wavelengths collected in the SASW surveys do not differ significantly from the far-field motions (Foinquinos Mera 1991; Roesset et al. 1991).

Lastly, the final shear-wave velocity profile was presented to a depth of approximately 0.5 times the maximum wavelength in the experimental dispersion curve. This cutoff depth is based on the fact that most of the particle motion occurs at depths less than one-half of the wavelength, as shown on Figure 41. Experience has shown this to be an acceptable cut-off depth for shear-wave velocity profiles (Brown 1998, Section 7.5).

6.2.7.3 Results

All final shear-wave velocity profiles are shown in Figures 54 to 88 and values are listed in Attachment IX.. All 35 shear-wave velocity profiles estimated from the SASW surveys are shown on Figure 89 (except for D-12). For selected profiles, the generalized lithology from the nearest borehole (Figure 43) is also shown. A total of 20 profiles extend to depths of 150 ft or greater. Shear-wave velocity profiles to depths of 300 feet or greater were generated along five

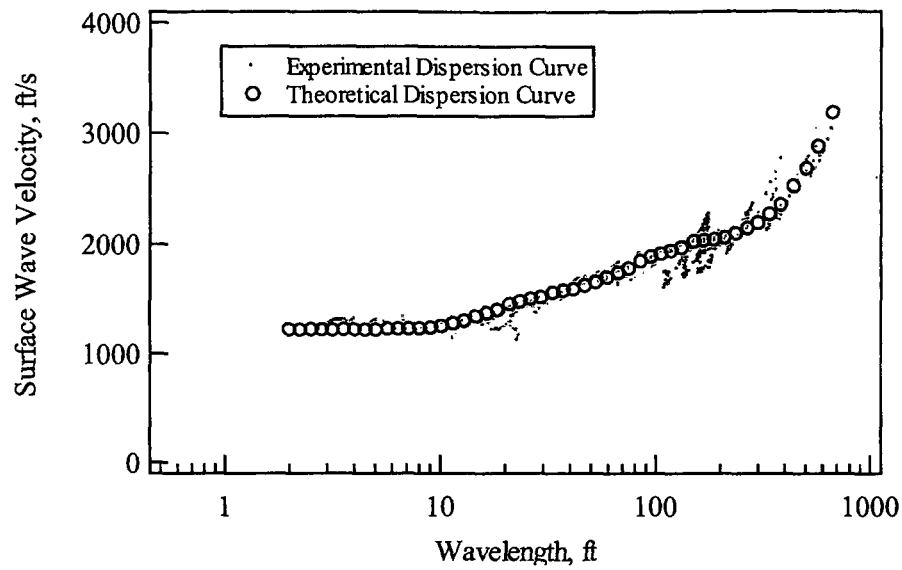

Source: Wong (2002c, Appendix 39, page 440)

Figure 52. Theoretical Dispersion Curve Fit to the Experimental Dispersion Curve at SASW-24

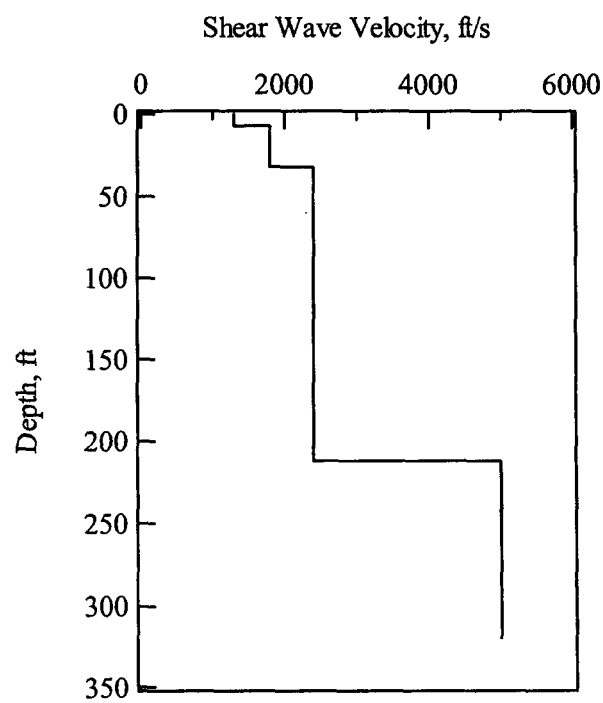

Source: Wong (2002c, Appendix 39, page 440)

Figure 53. Final Shear-Wave Velocity Profiles Determined at SASW-24

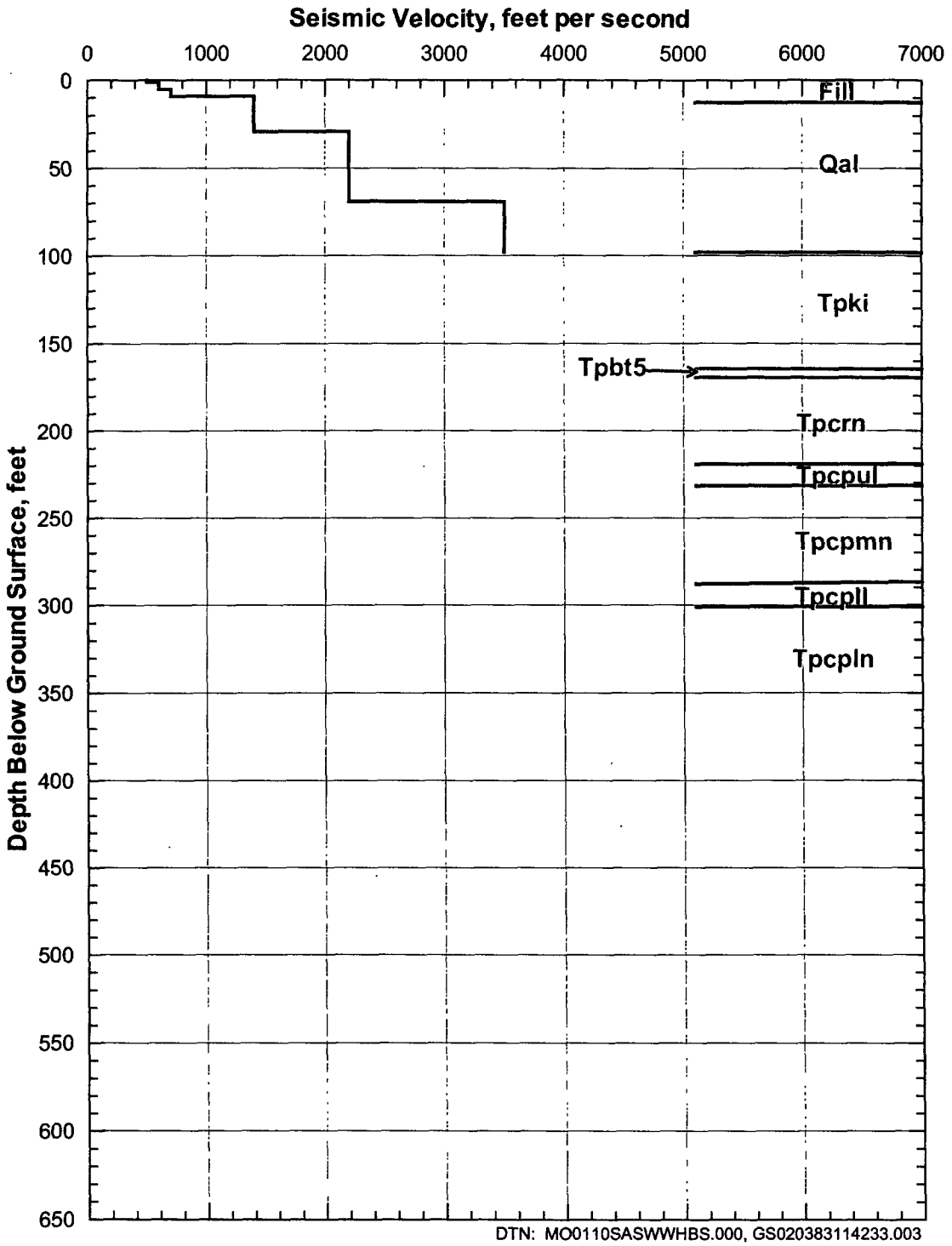

Figure 54. Shear-Wave Velocity Profile from SASW-1 and Generalized Lithology from RF#13

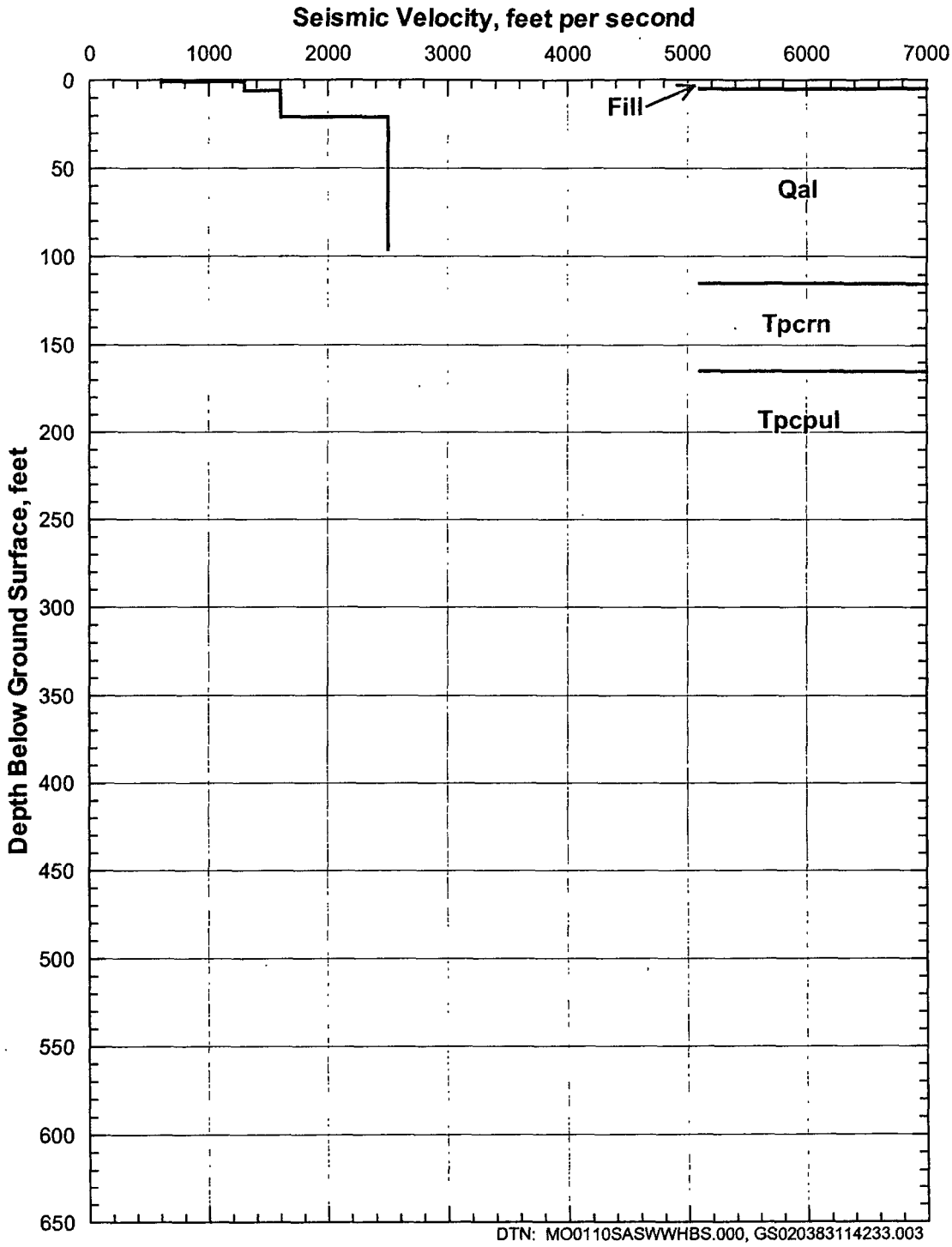

Figure 55. Shear-Wave Velocity Profile from SASW-2 and Generalized Lithology from RF#21

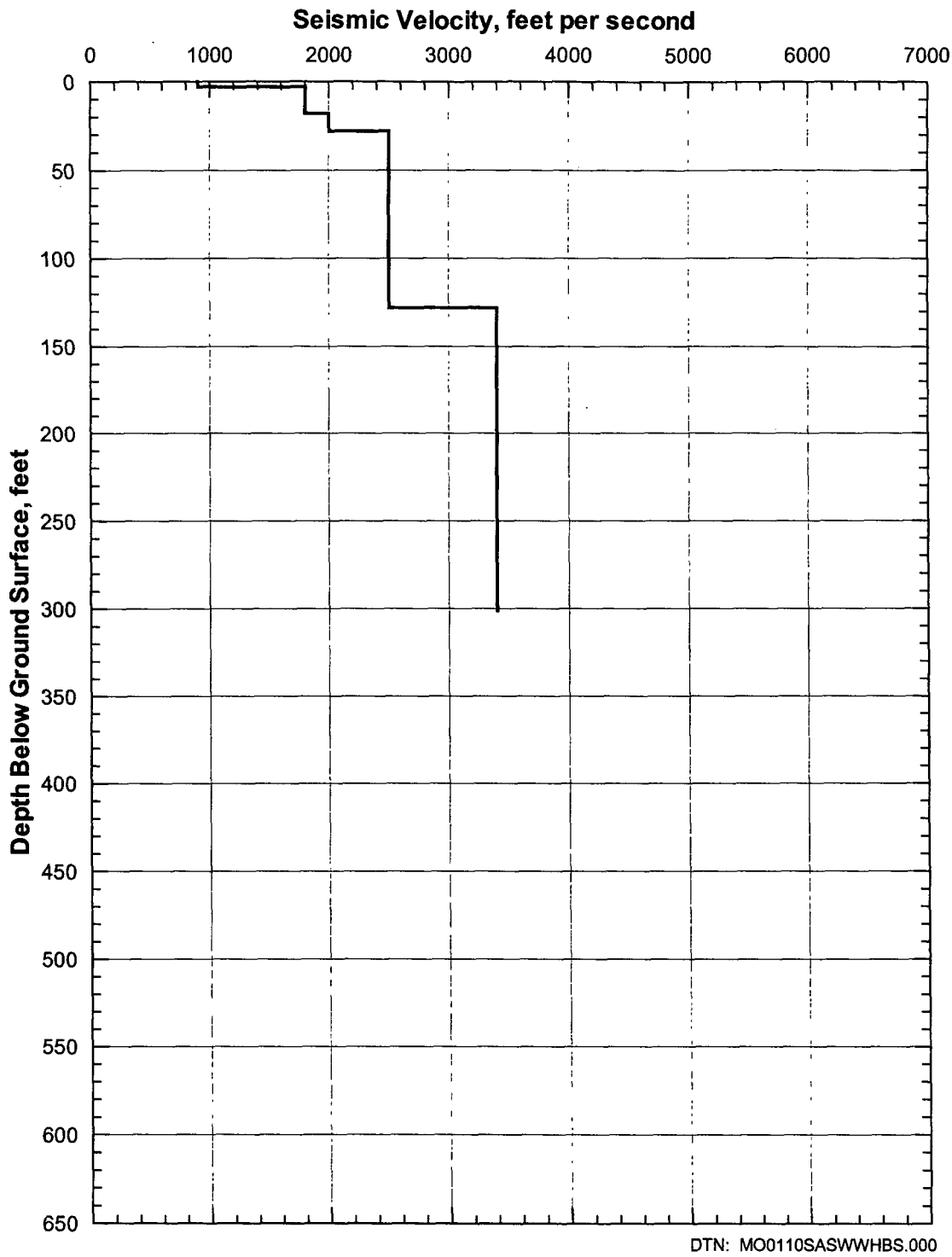

Figure 56. Shear-Wave Velocity Profile from SASW-3

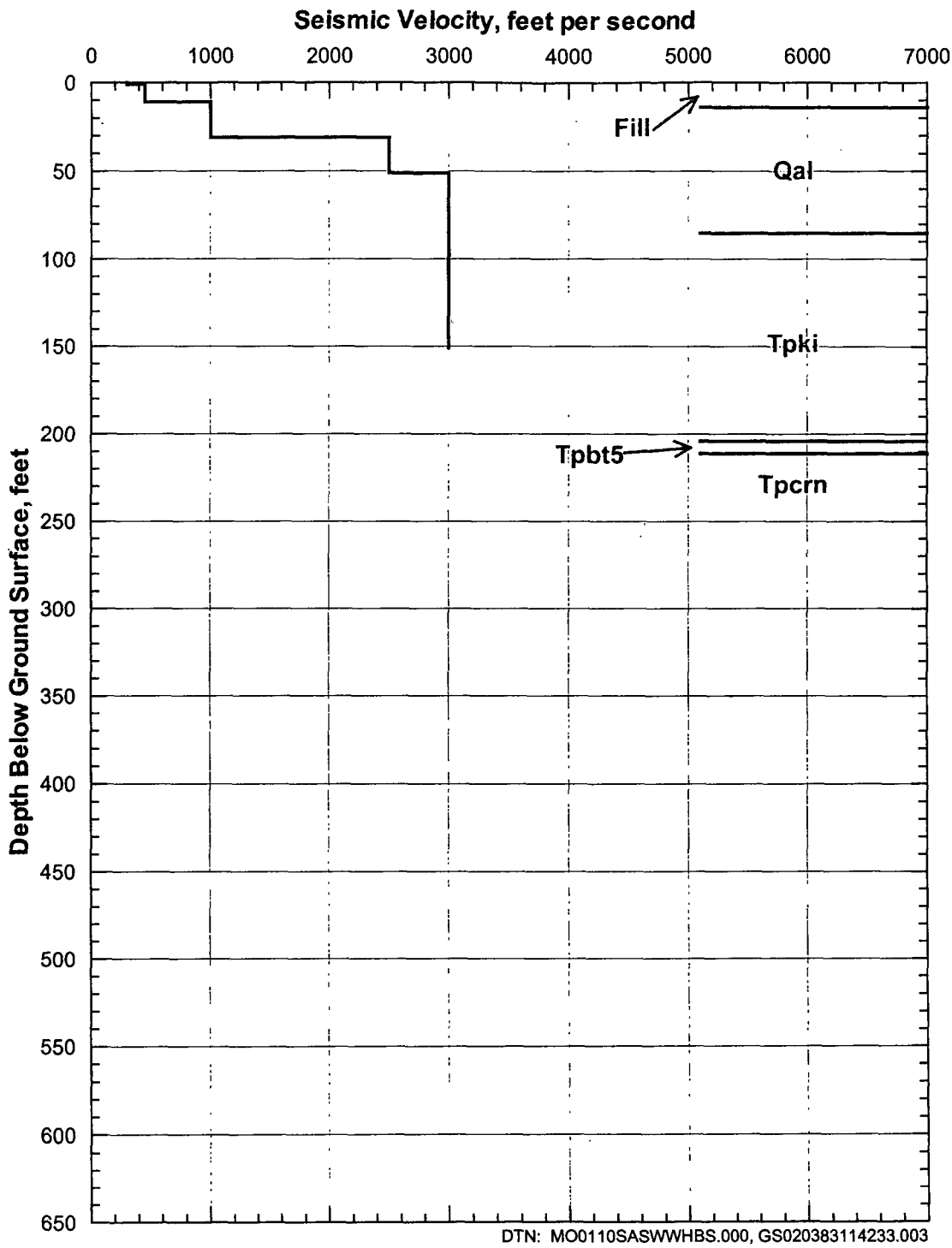

Figure 57. Shear-Wave Velocity Profile from SASW-4 and Generalized Lithology from RF#26

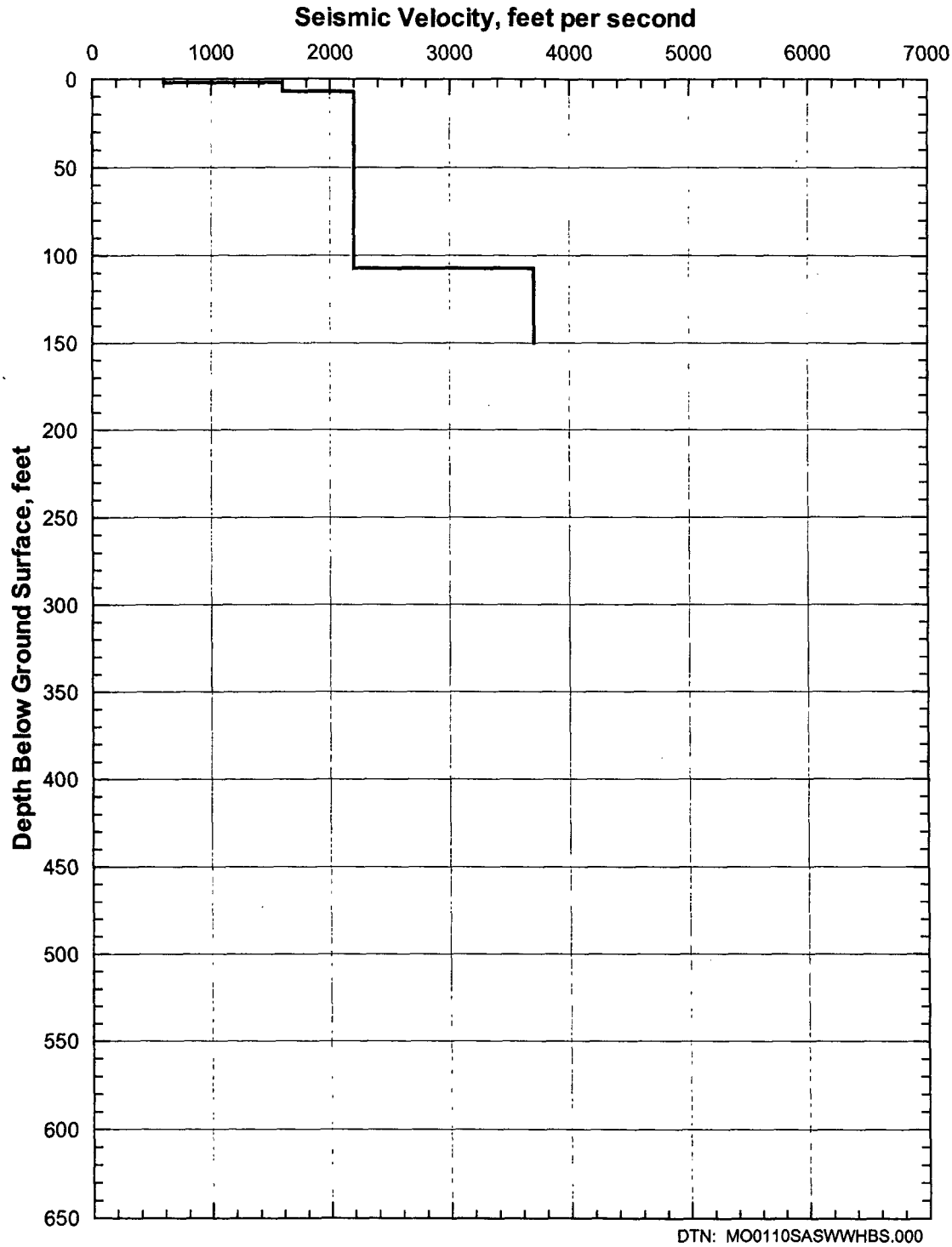

Figure 58. Shear-Wave Velocity Profile from SASW-5

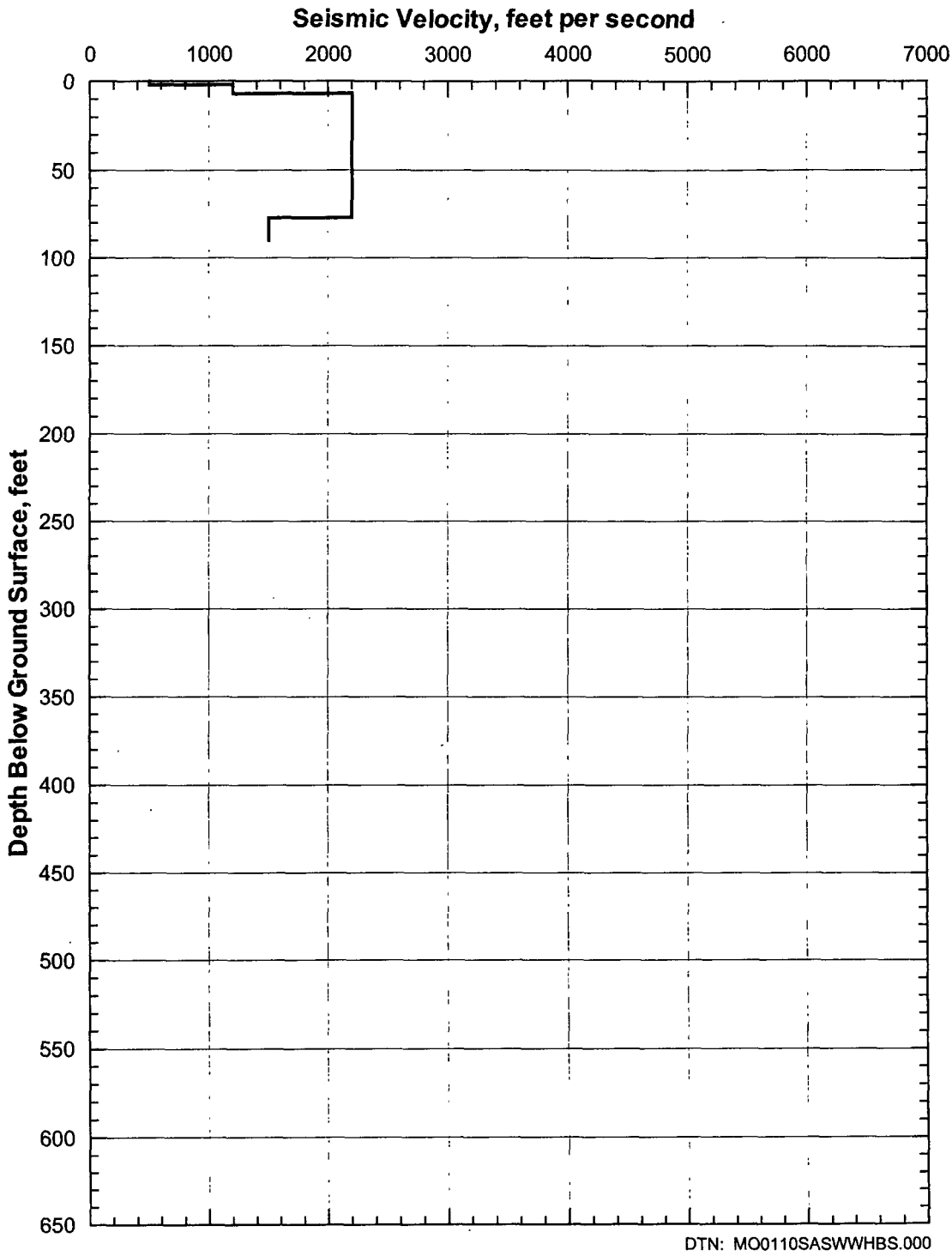

Figure 59. Shear-Wave Velocity Profile from SASW-6

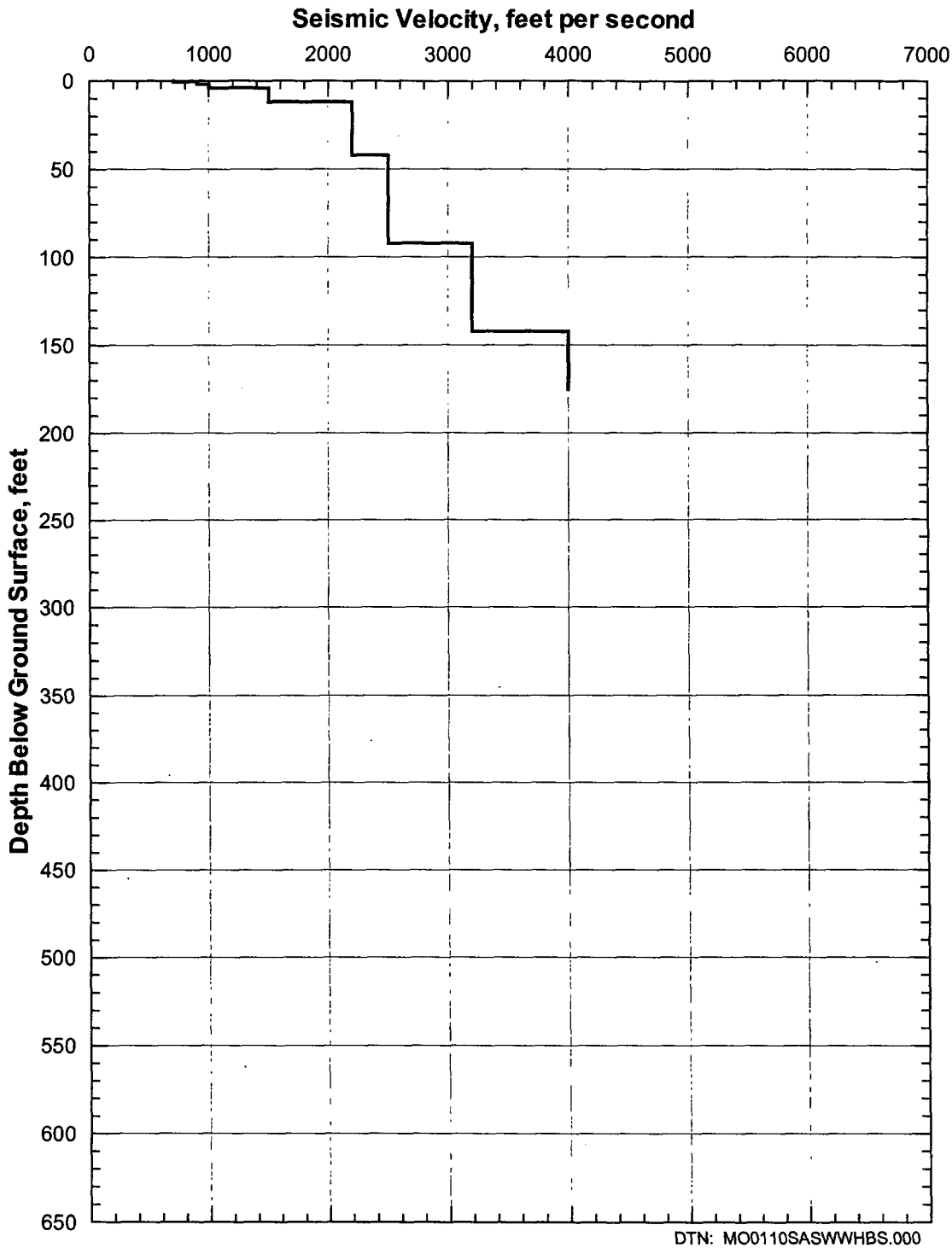

Figure 60. Shear-Wave Velocity Profile from SASW-7

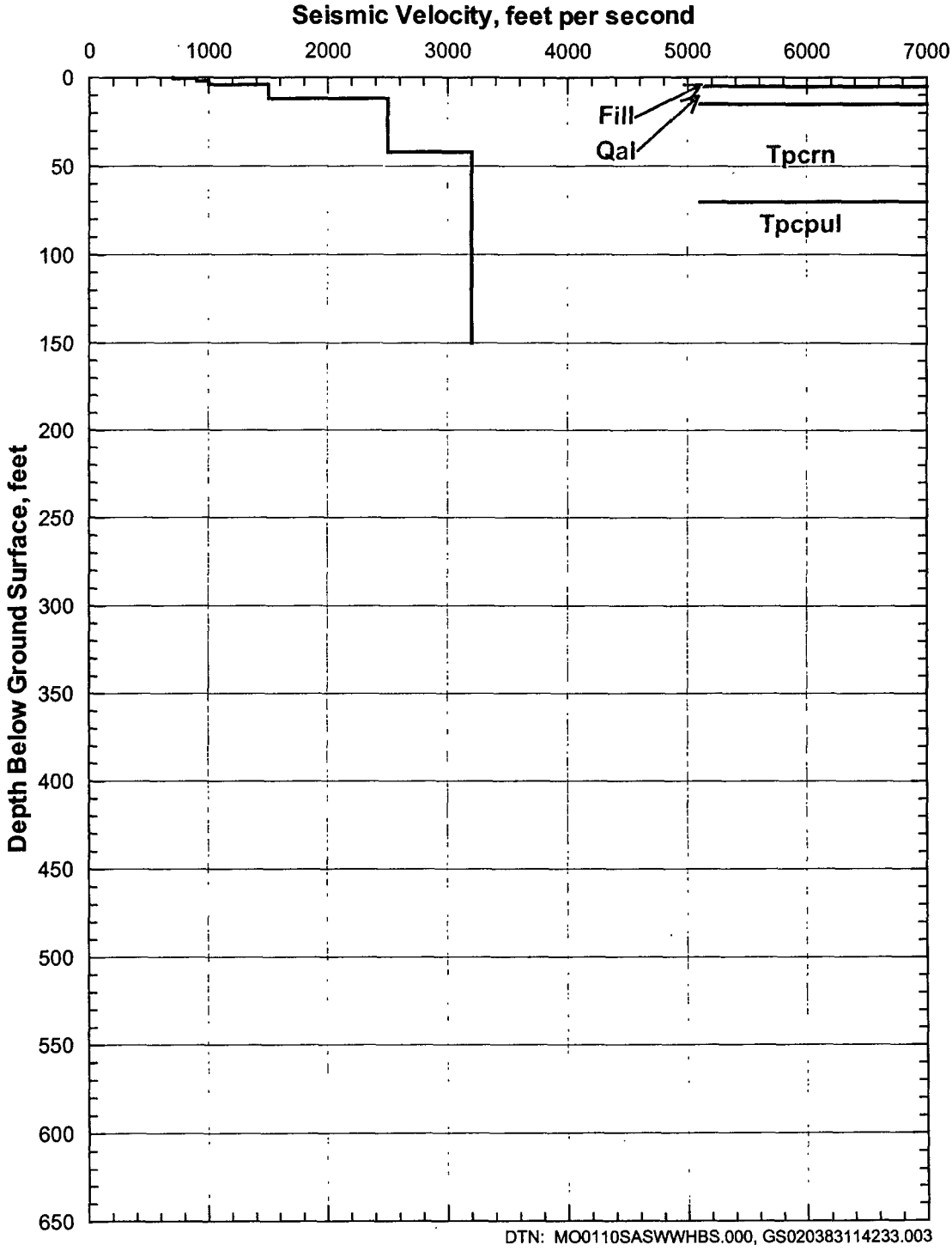

Figure 61. Shear-Wave Velocity Profile from SASW-8 and Generalized Lithology from RF#28

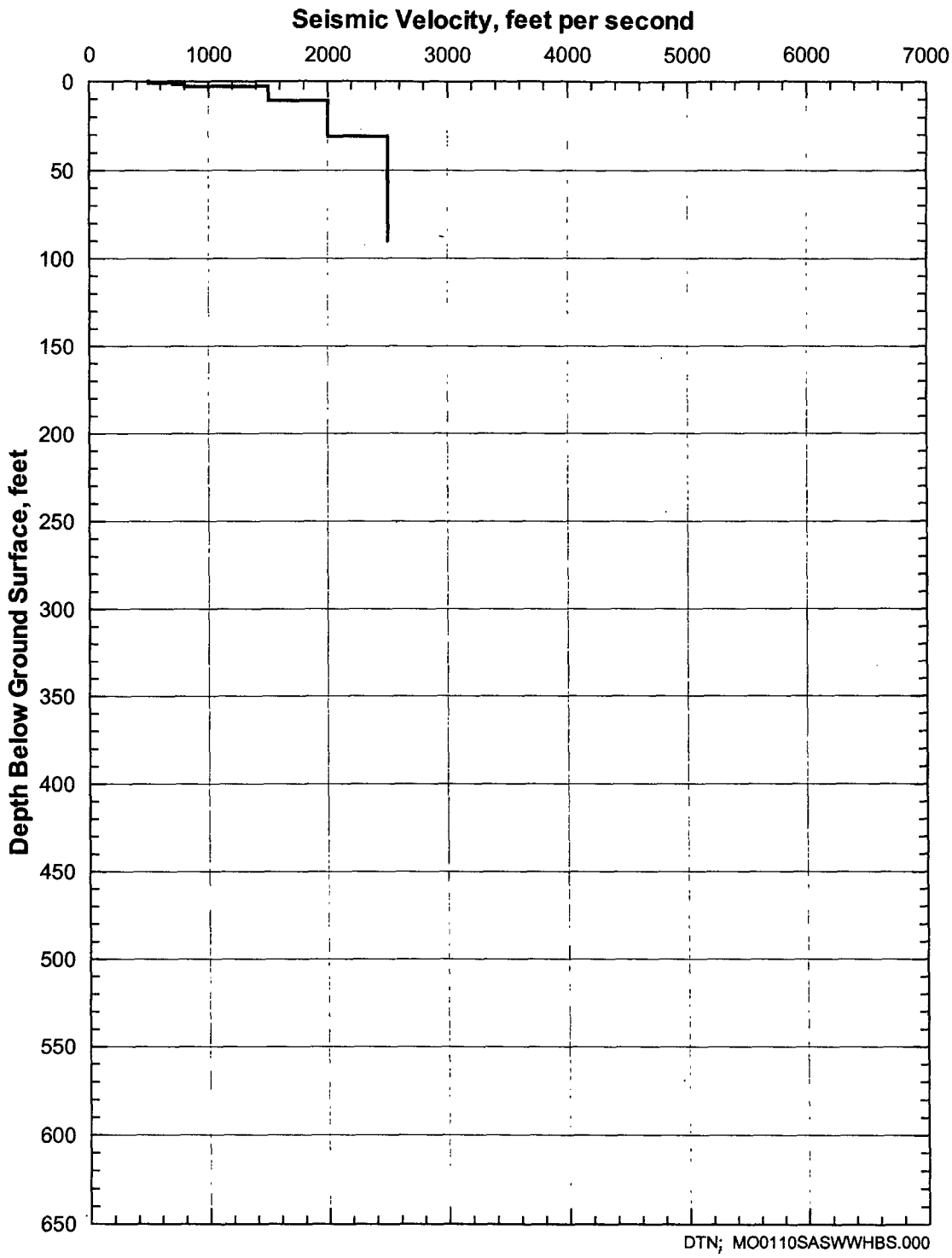

Figure 62. Shear-Wave Velocity Profile from SASW-9

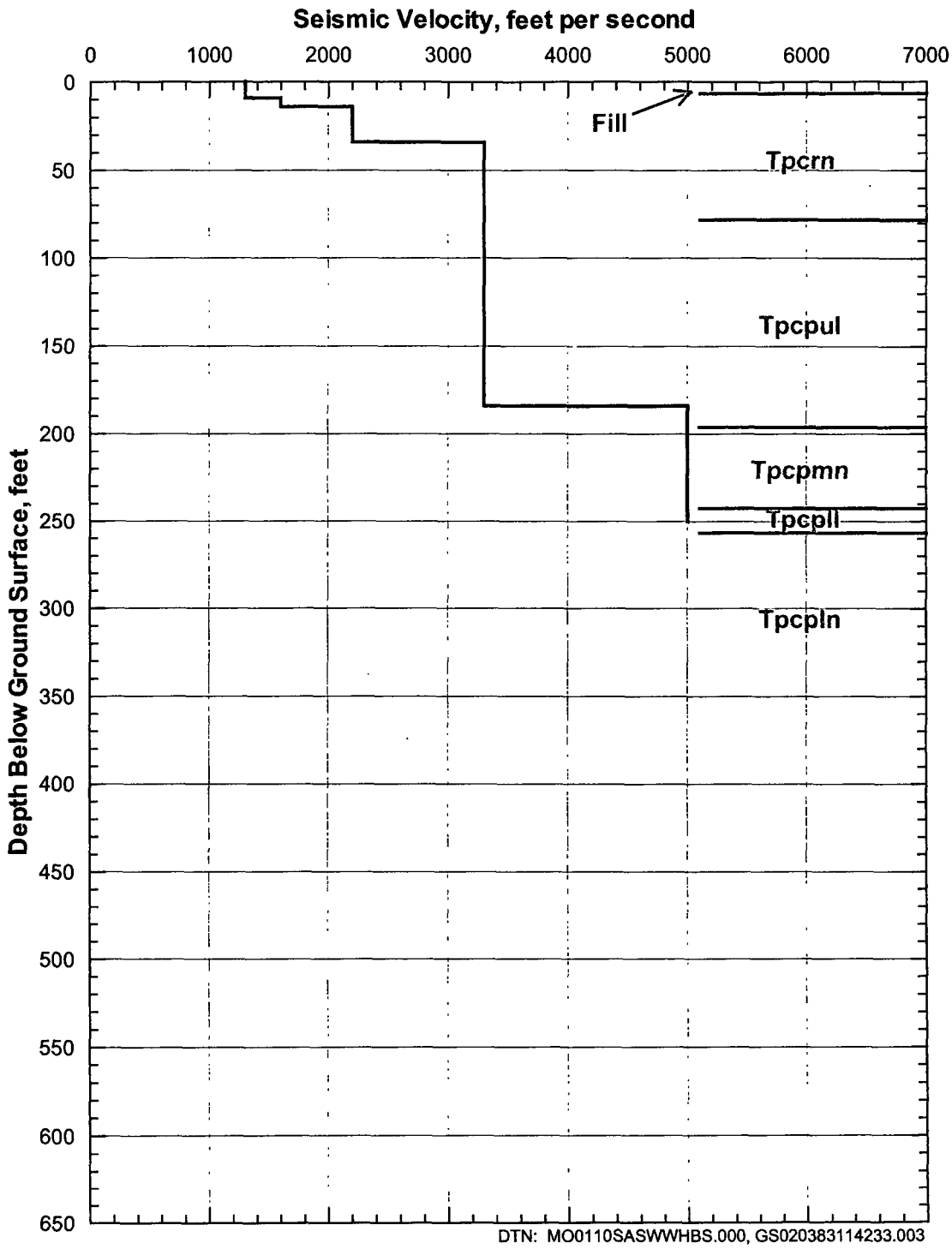

Figure 63. Shear-Wave Velocity Profile from SASW-10+37 and Generalized Lithology from RF#15

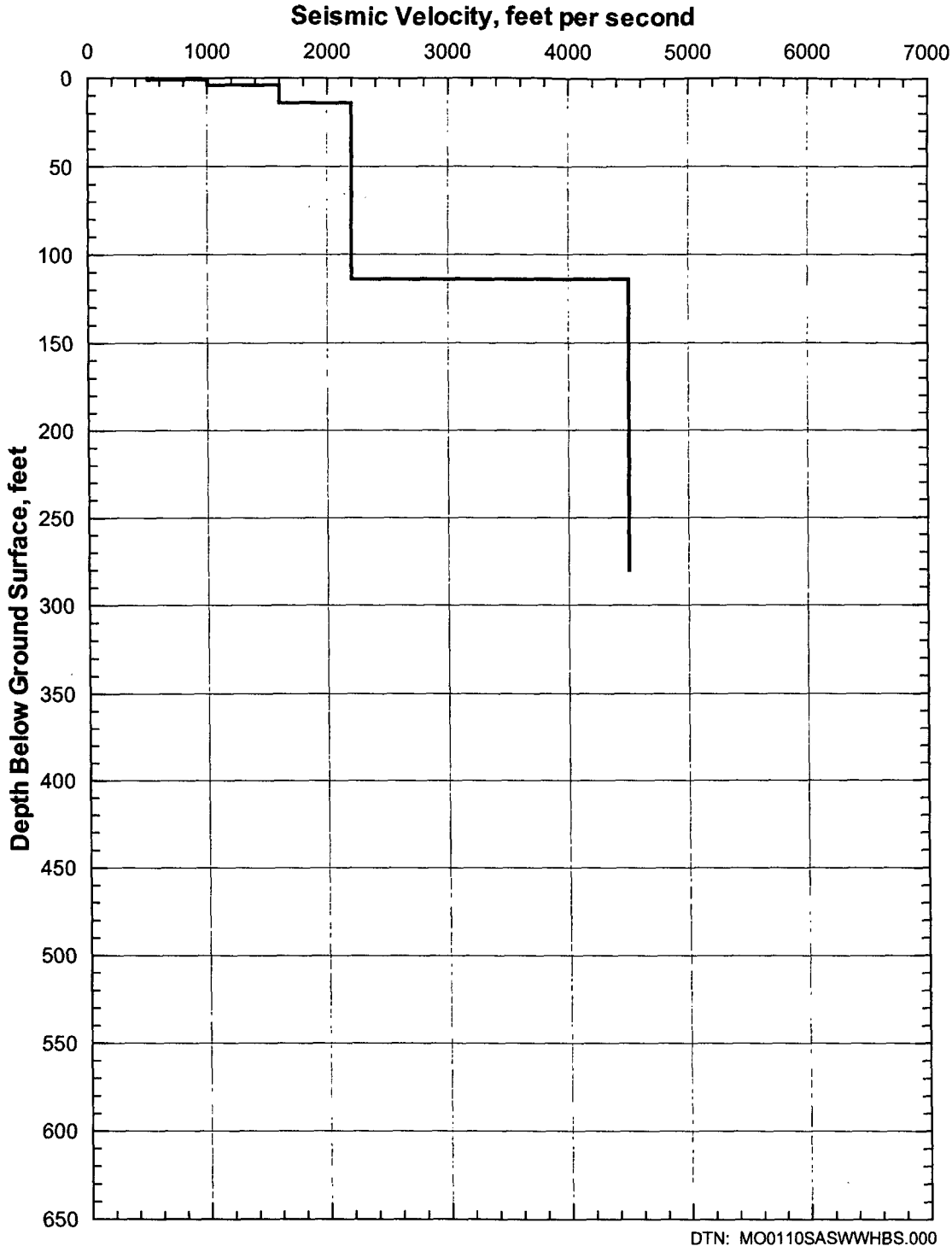

Figure 64. Shear-Wave Velocity Profile from SASW-11

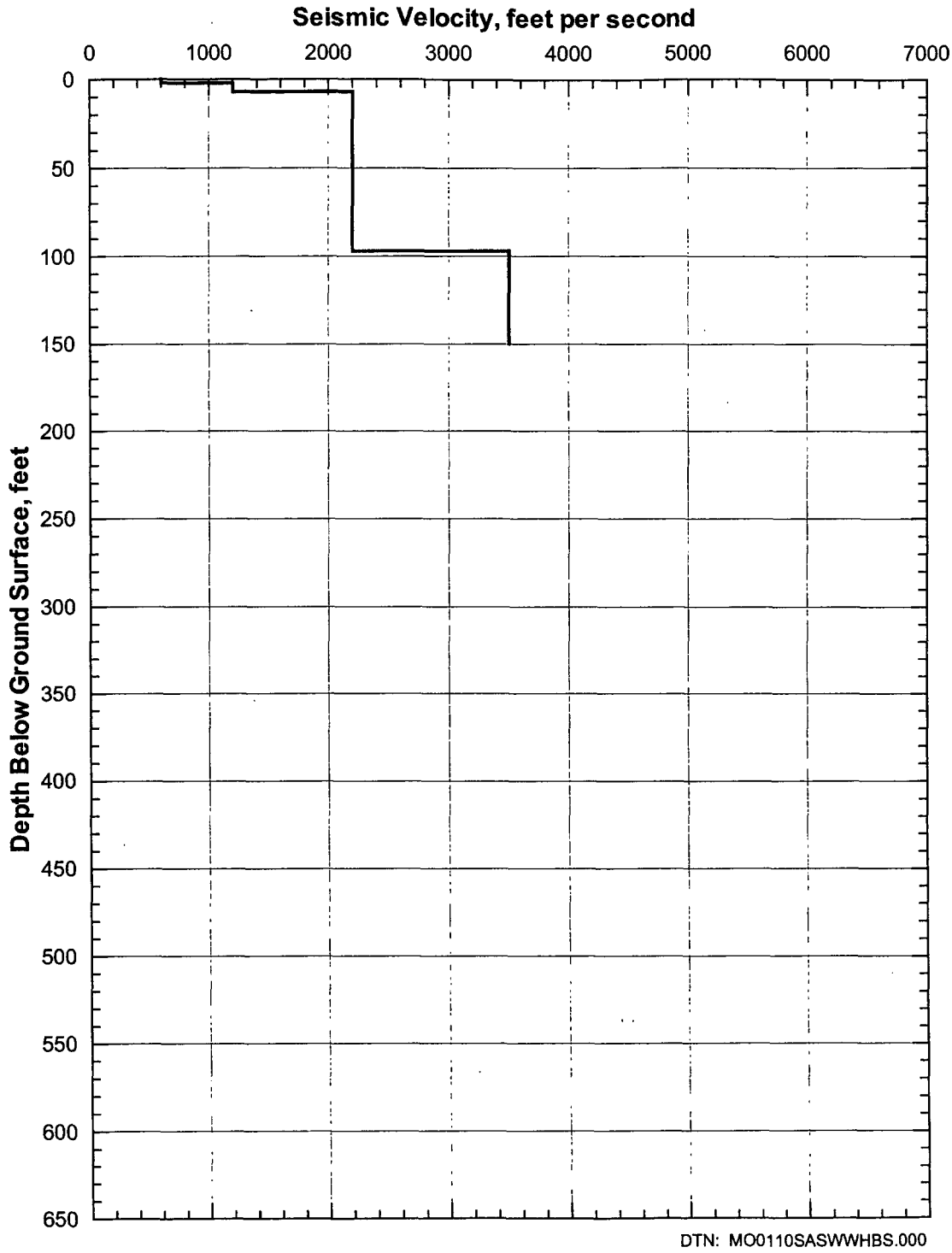

Figure 65. Shear-Wave Velocity Profile from SASW-12

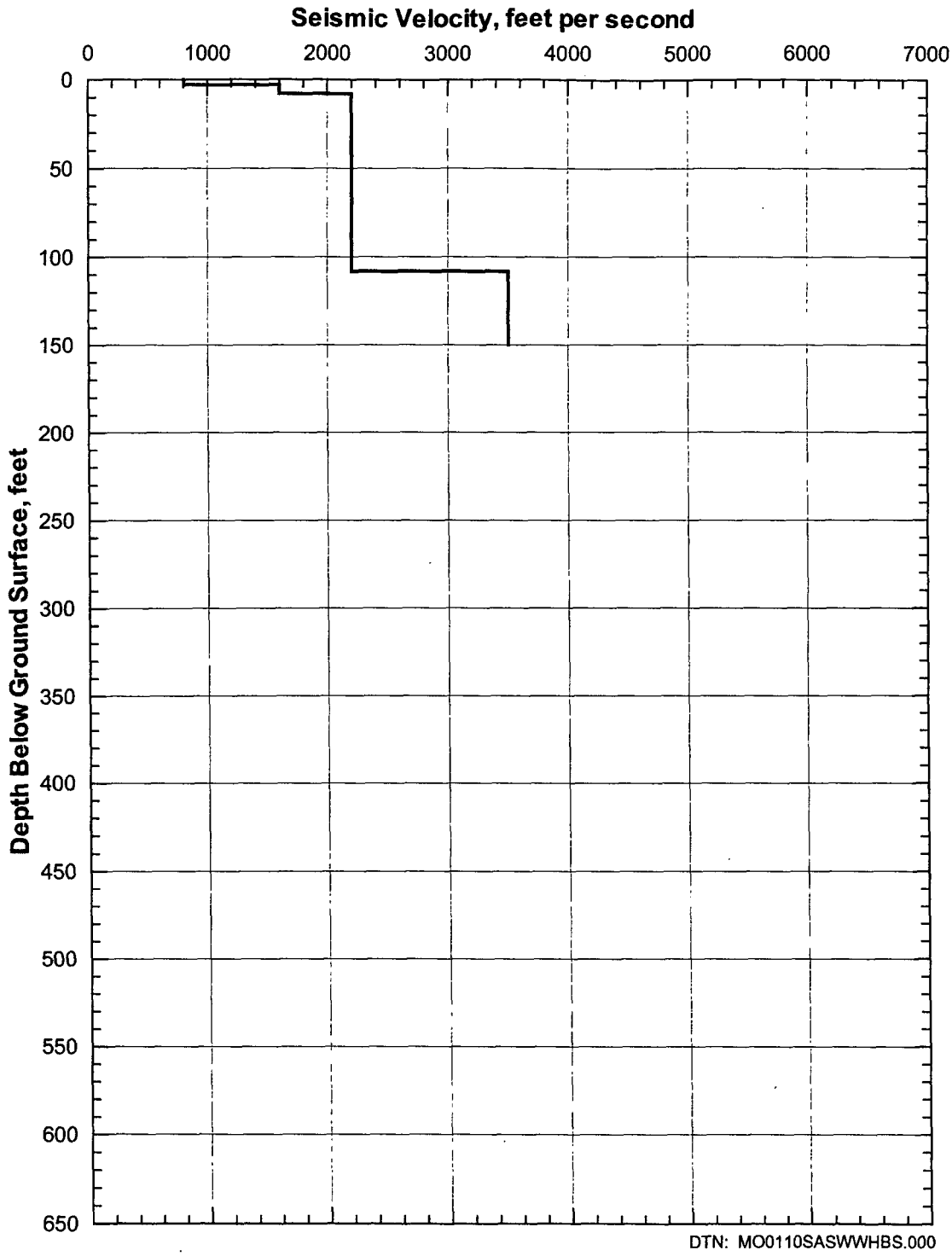

Figure 66. Shear-Wave Velocity Profile from SASW-13

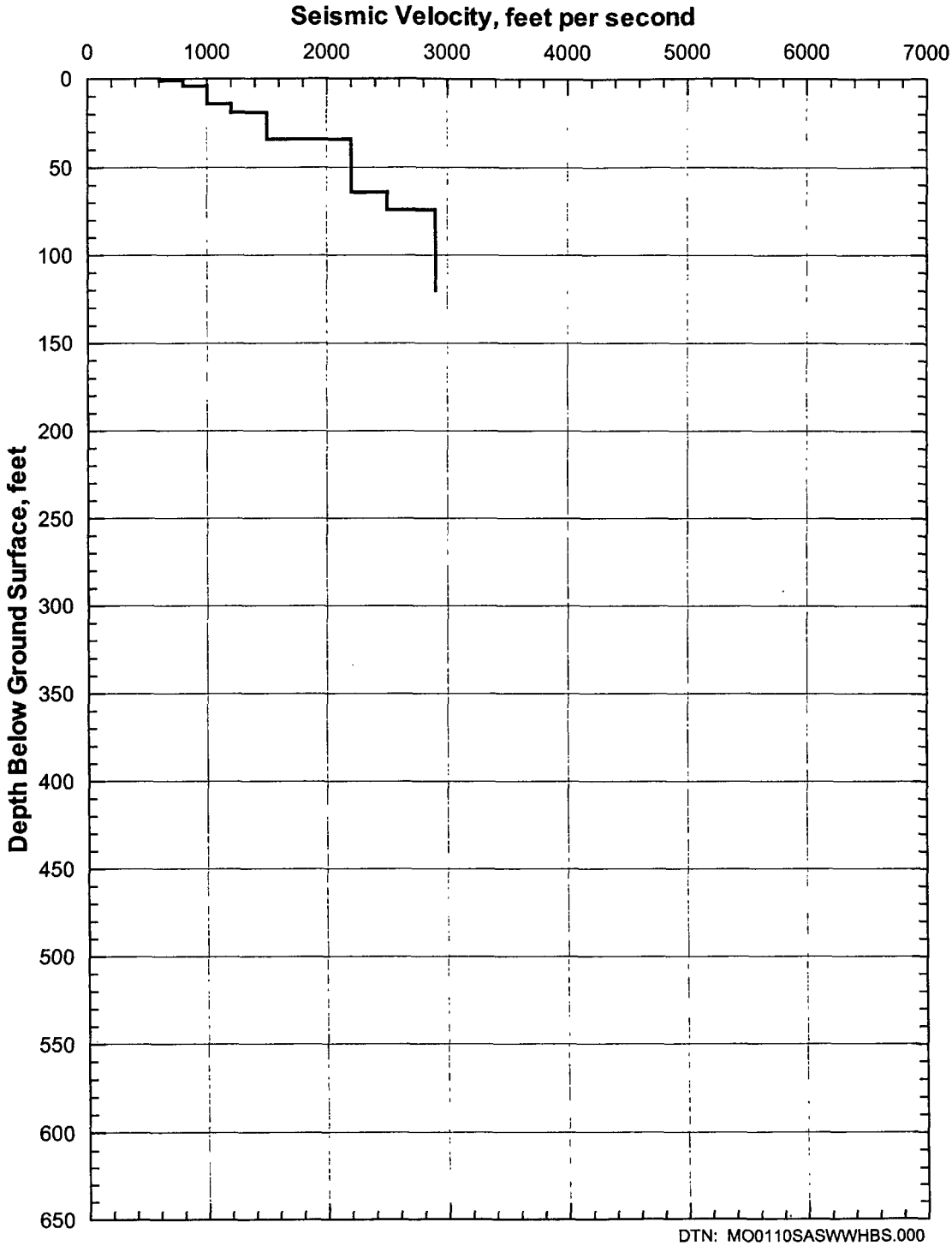

Figure 67. Shear-Wave Velocity Profile from SASW-14

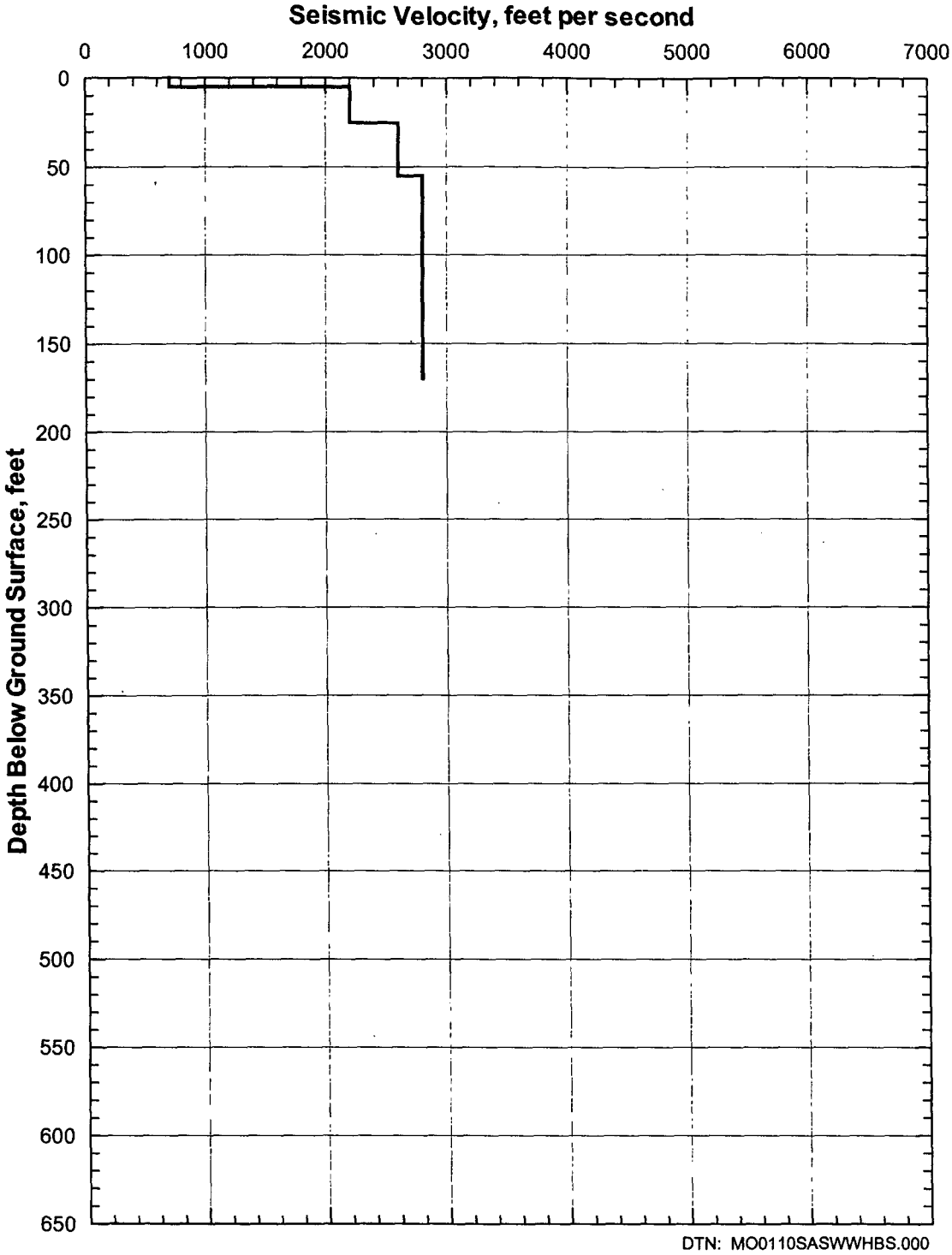

Figure 68. Shear-Wave Velocity Profile from SASW-15

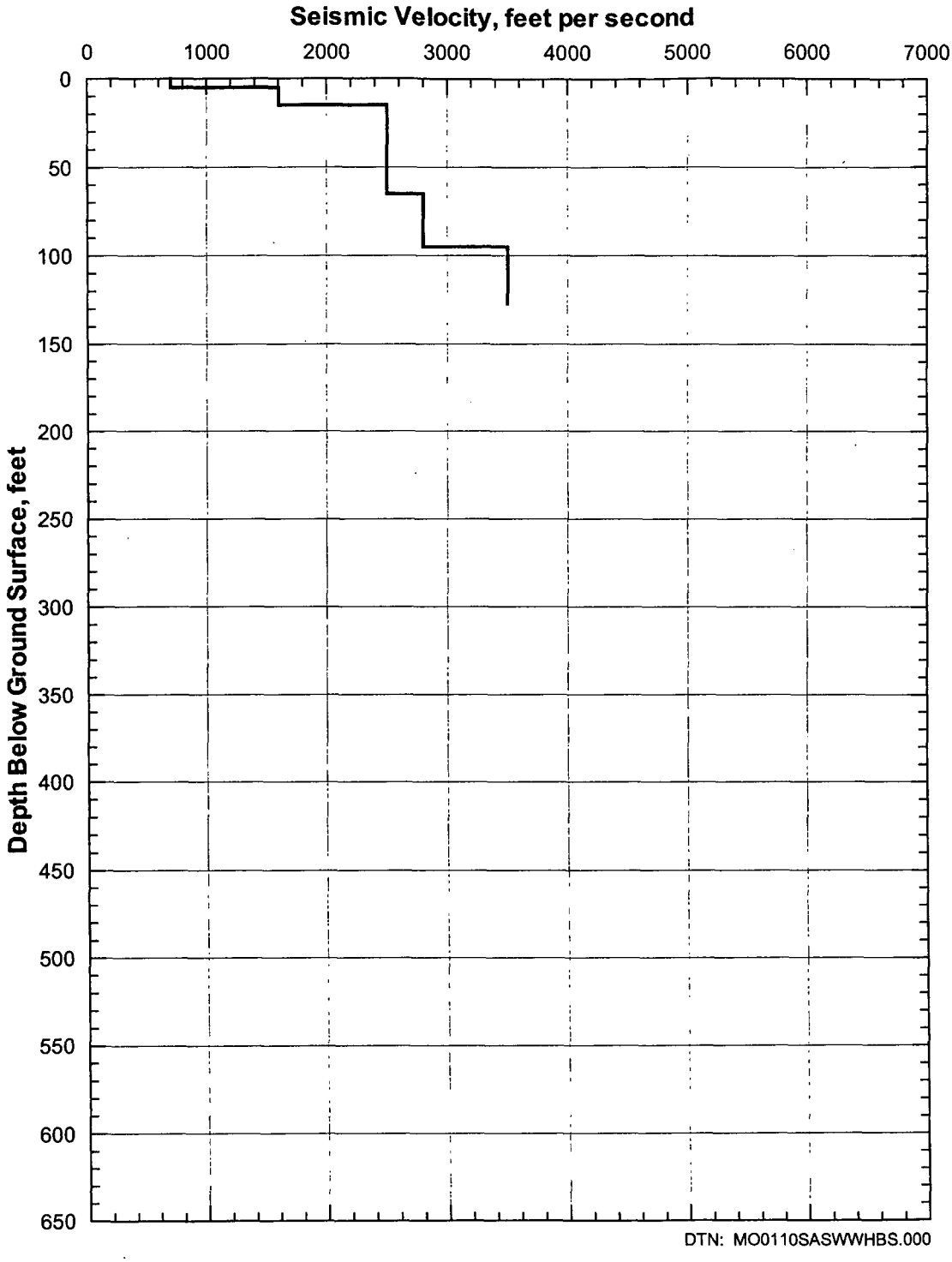

Figure 69. Shear-Wave Velocity Profile from SASW-16

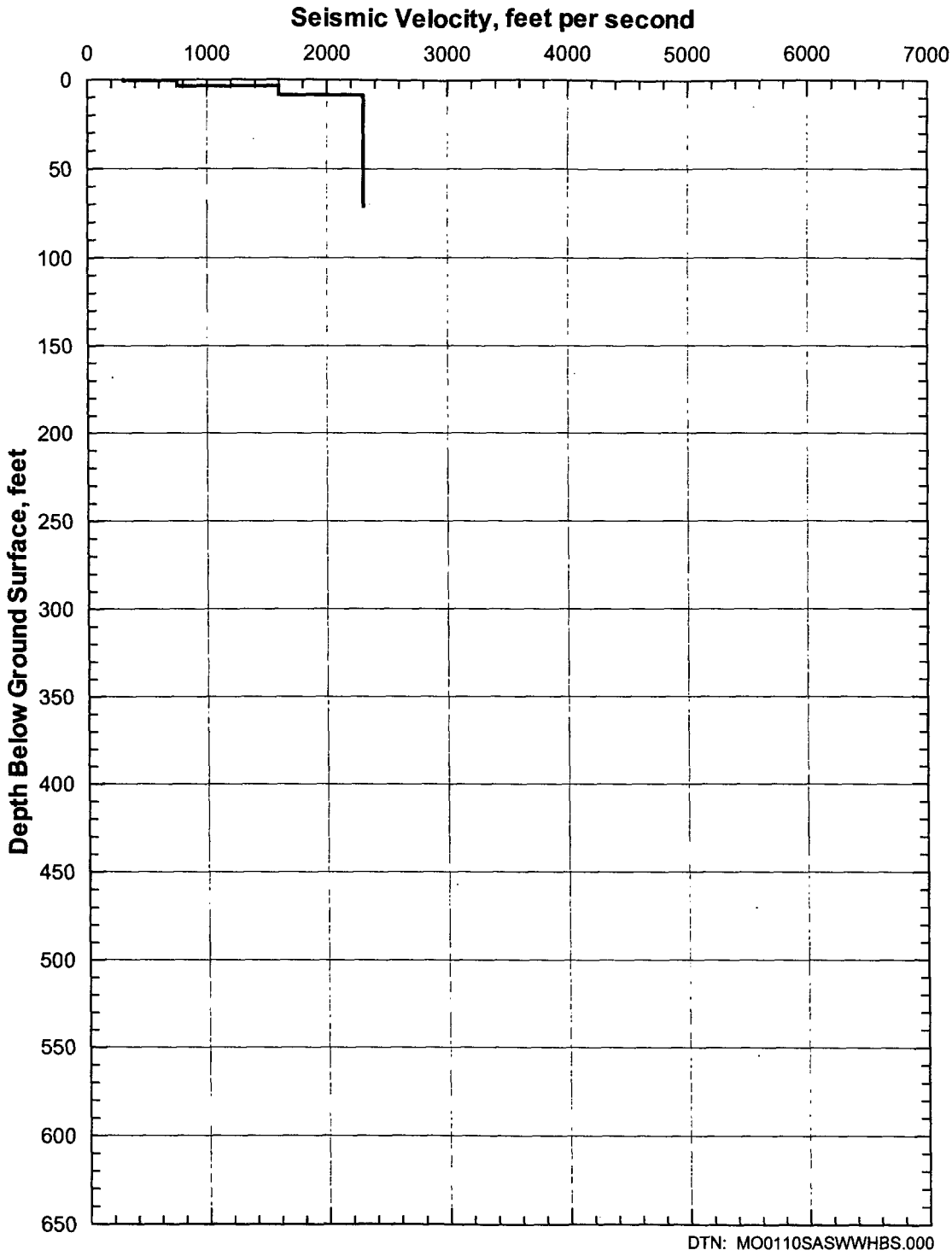

Figure 70. Shear-Wave Velocity Profile form SASW-17

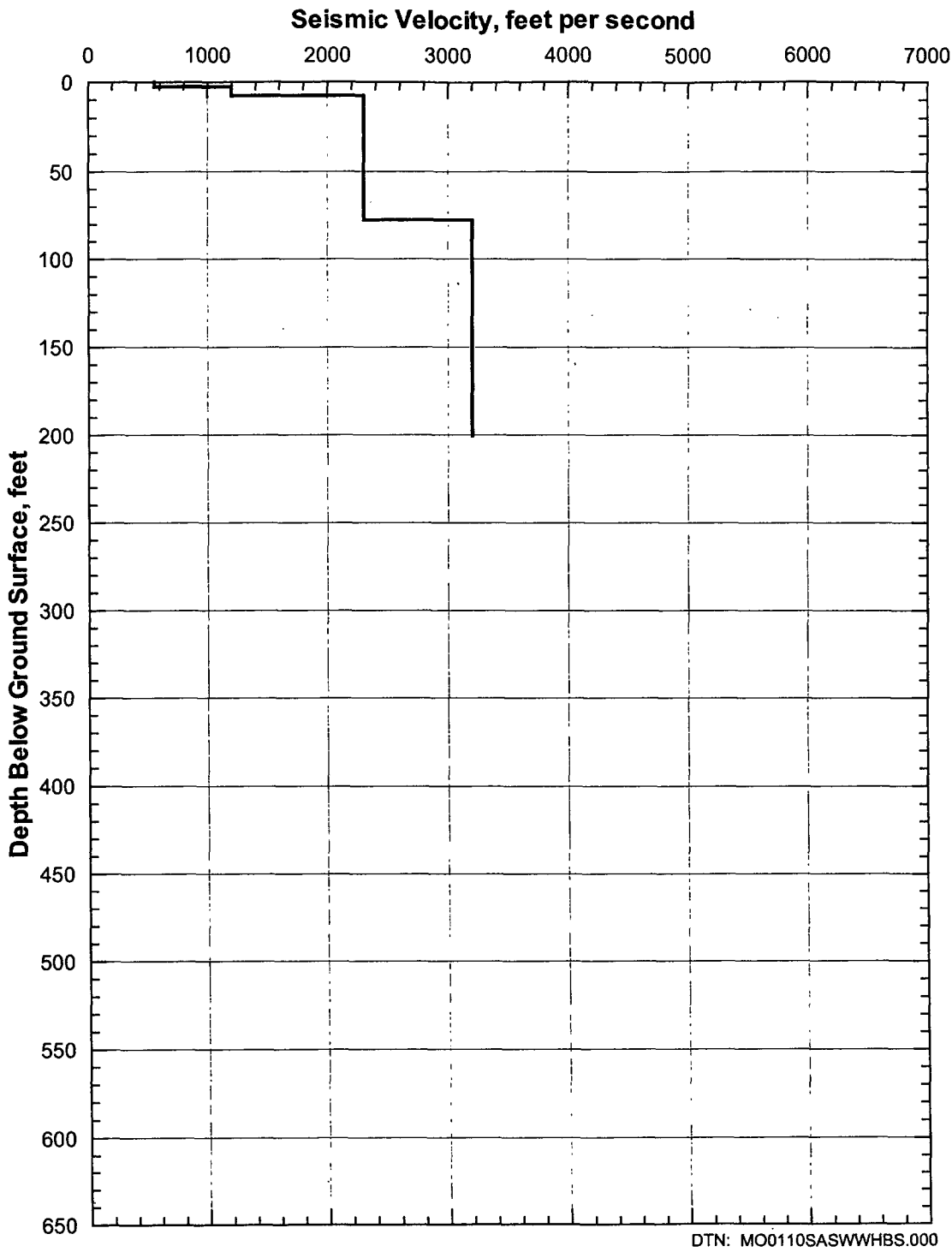

Figure 71. Shear-Wave Velocity Profile from SASW-18

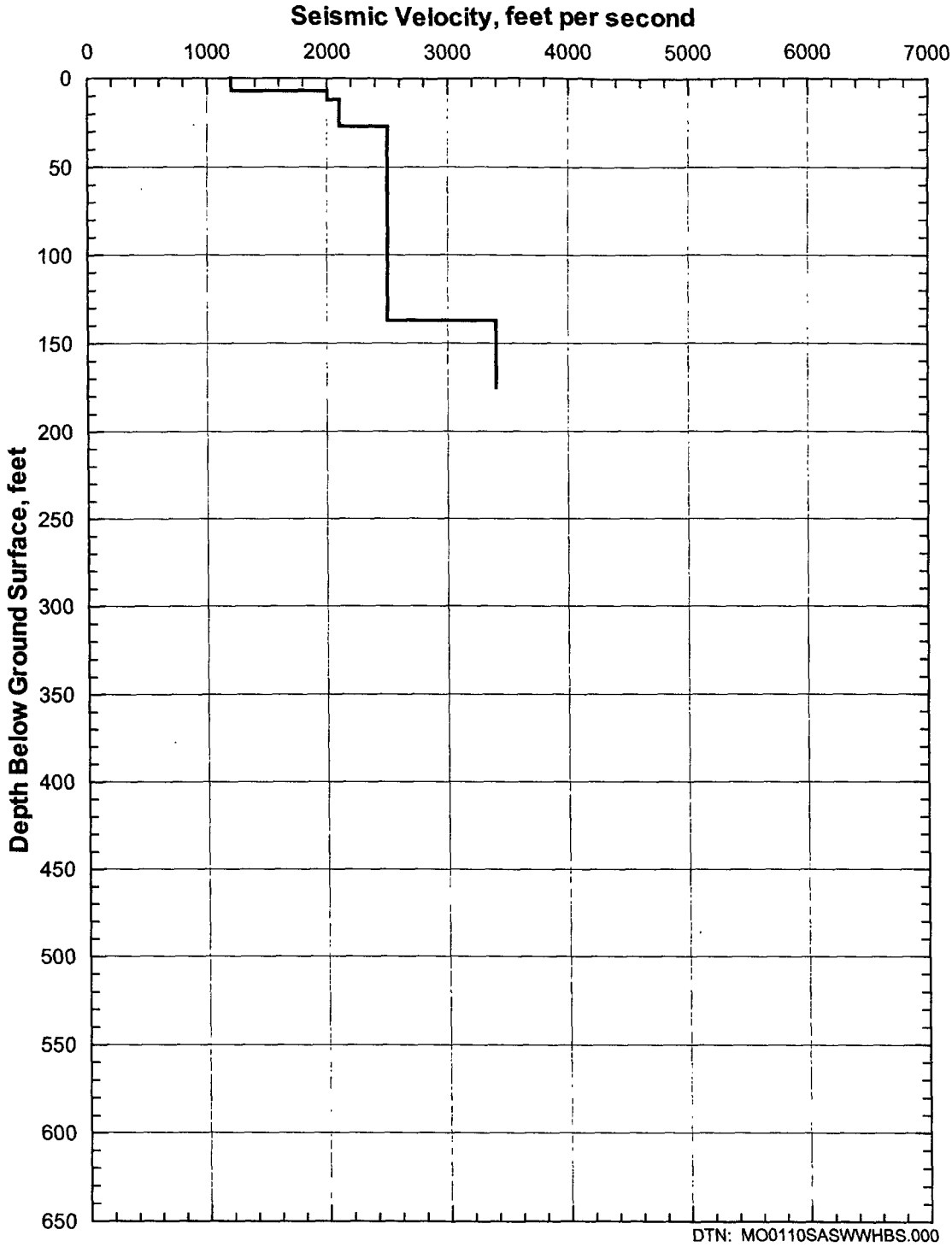

Figure 72. Shear-Wave Velocity Profile from SASW-19

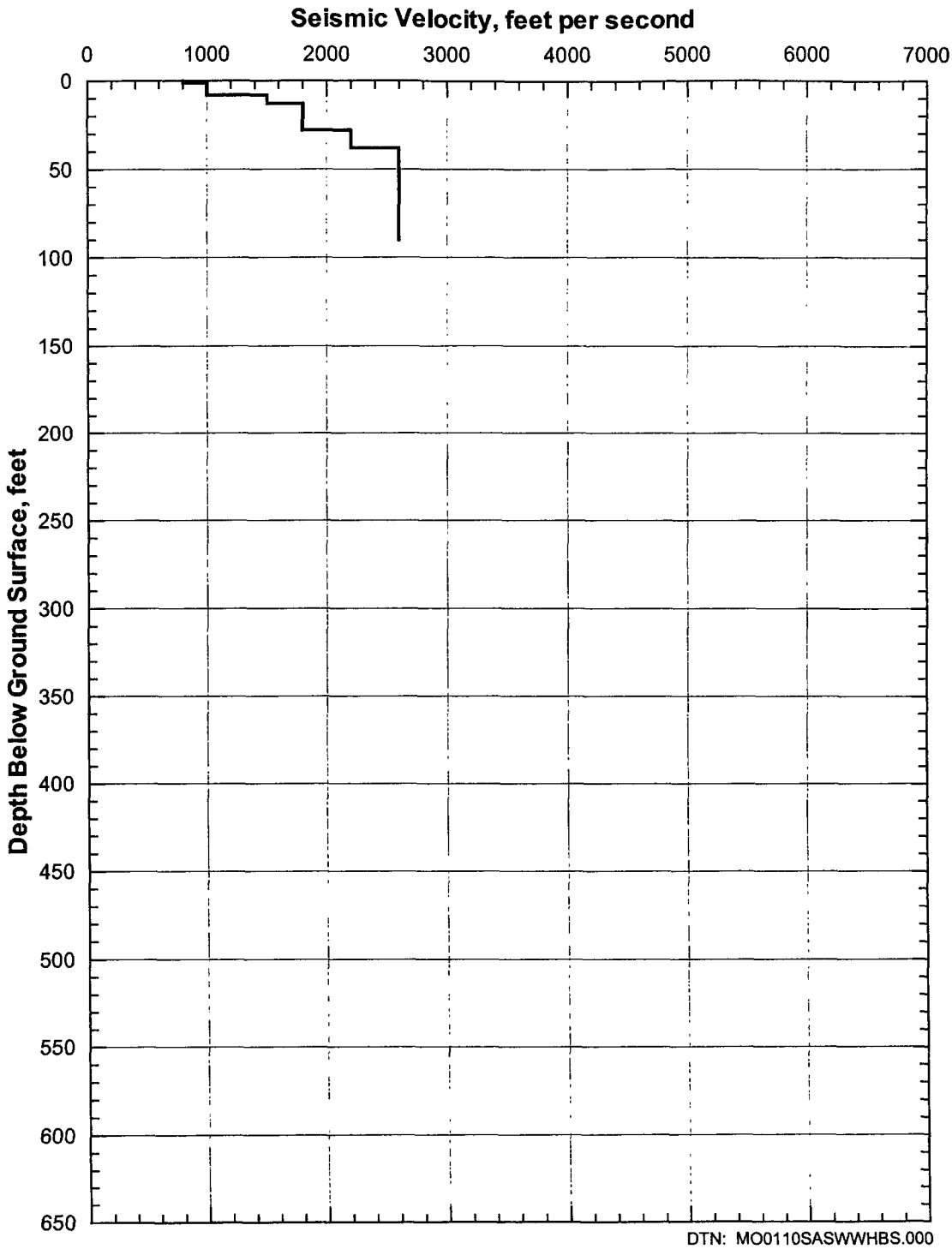

Figure 73. Shear-Wave Velocity Profile from SASW-20

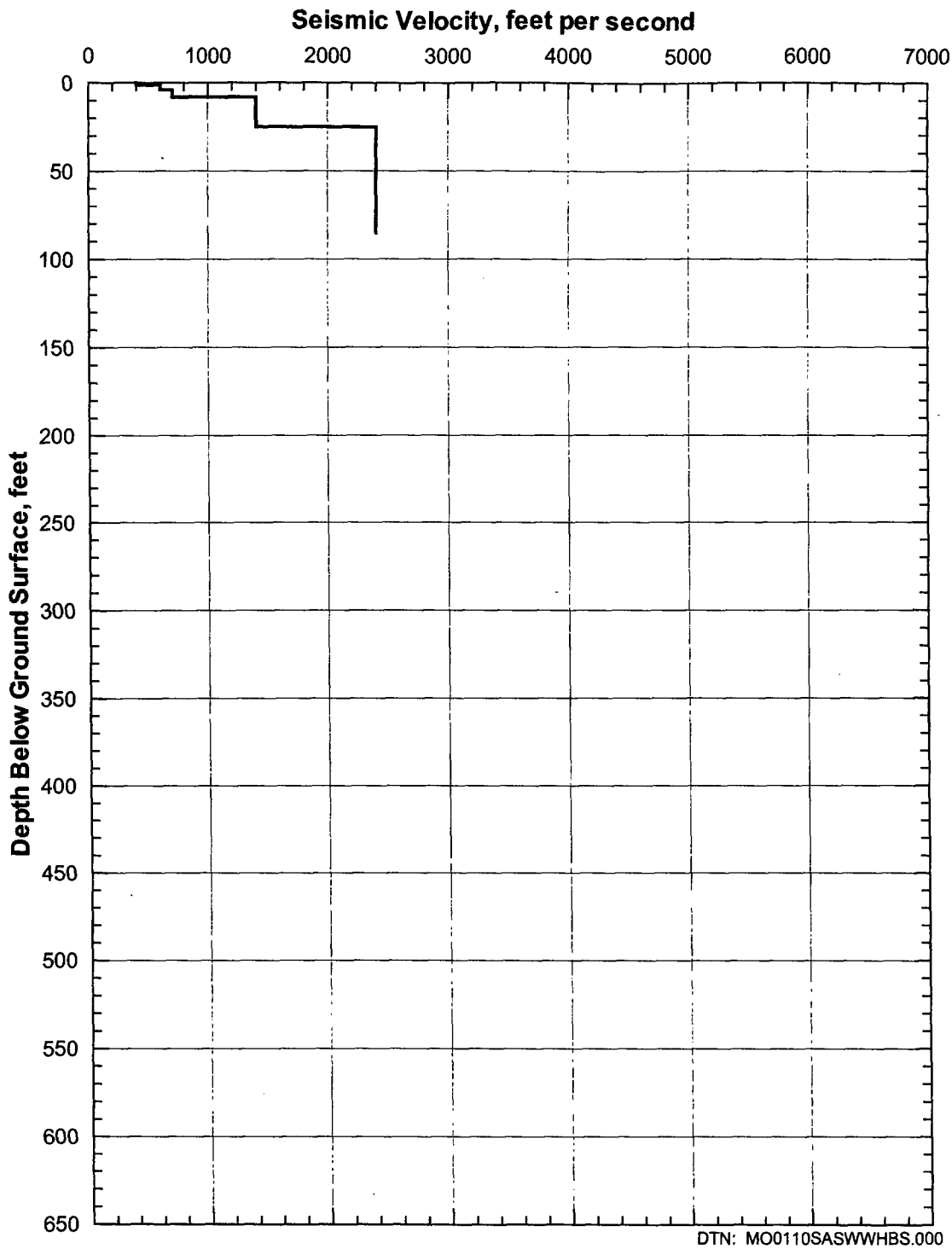

Figure 74. Shear-Wave Velocity Profile from SASW-21

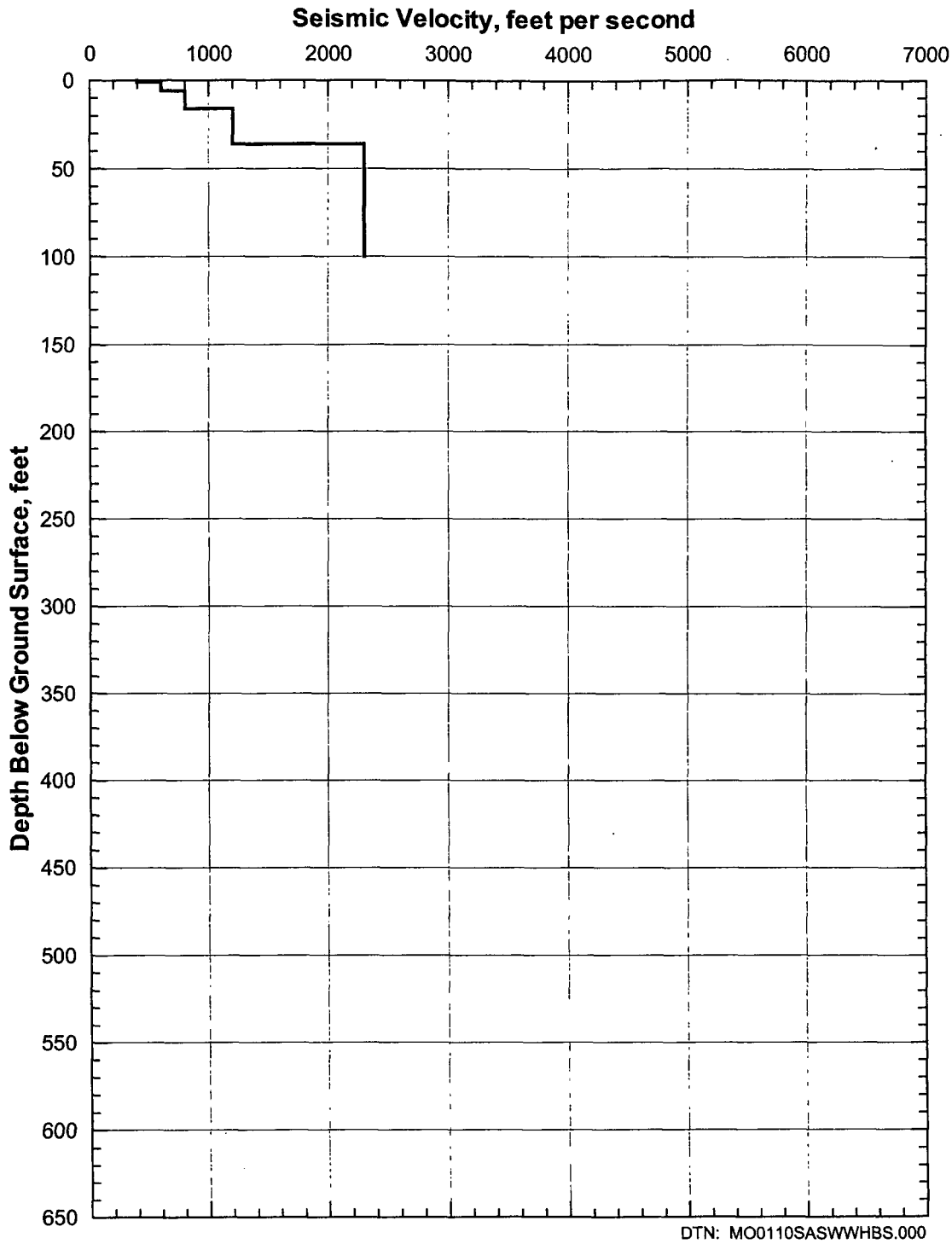

Figure 75. Shear-Wave Velocity Profile from SASW-22

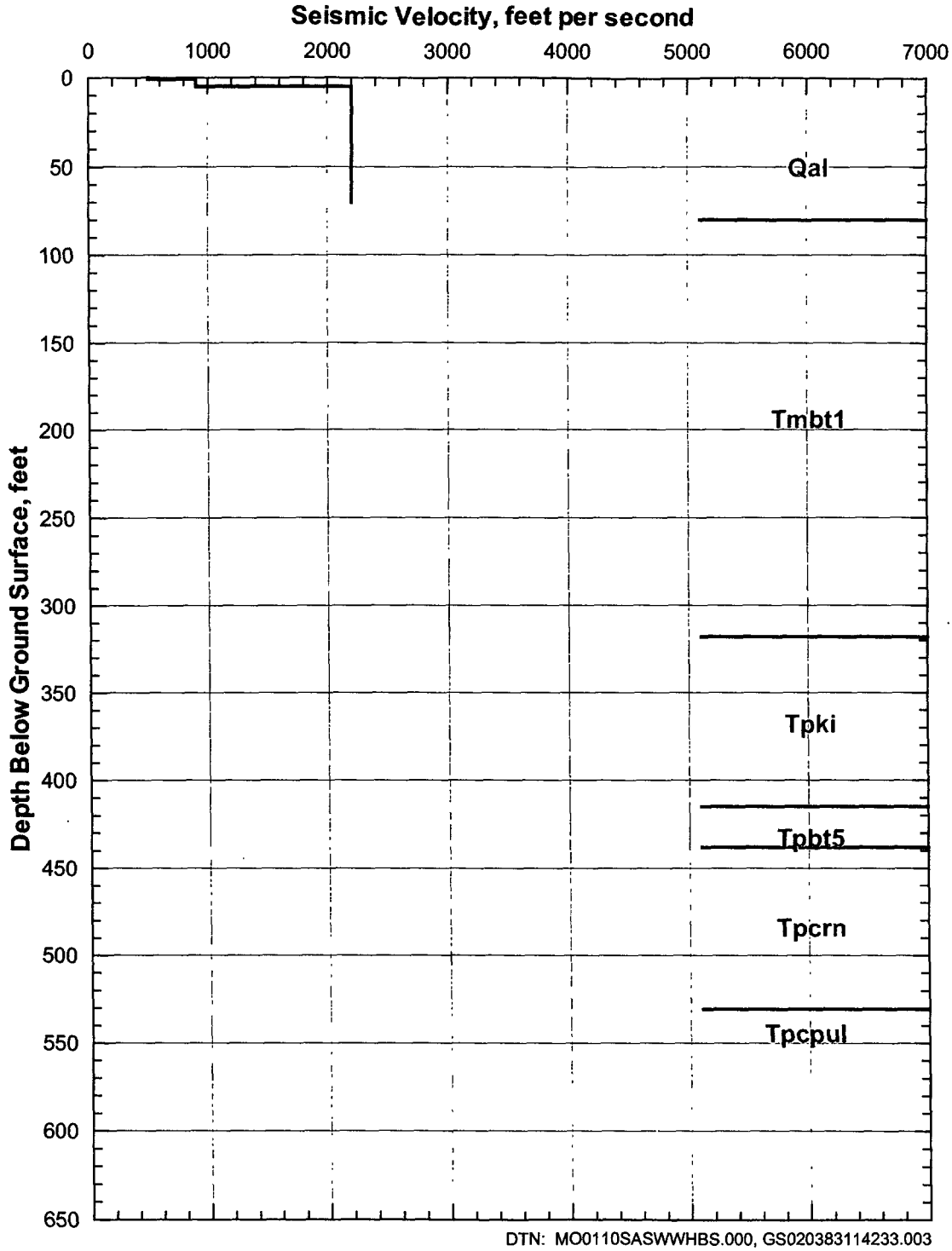

Figure 76. Shear-Wave Velocity Profile from SASW-23 and Generalized Lithology from RF#22

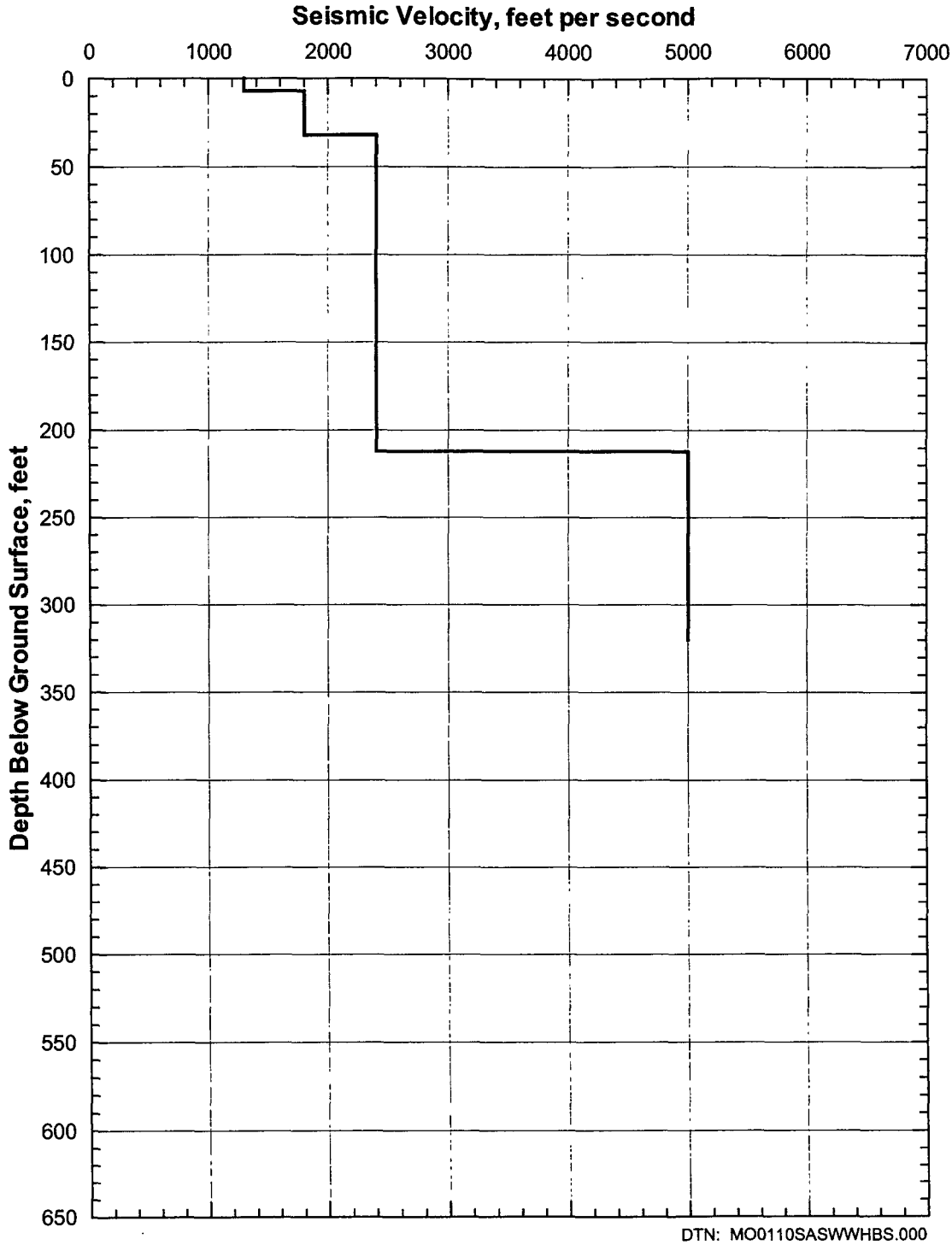

Figure 77. Shear-Wave Velocity Profile from SASW-24

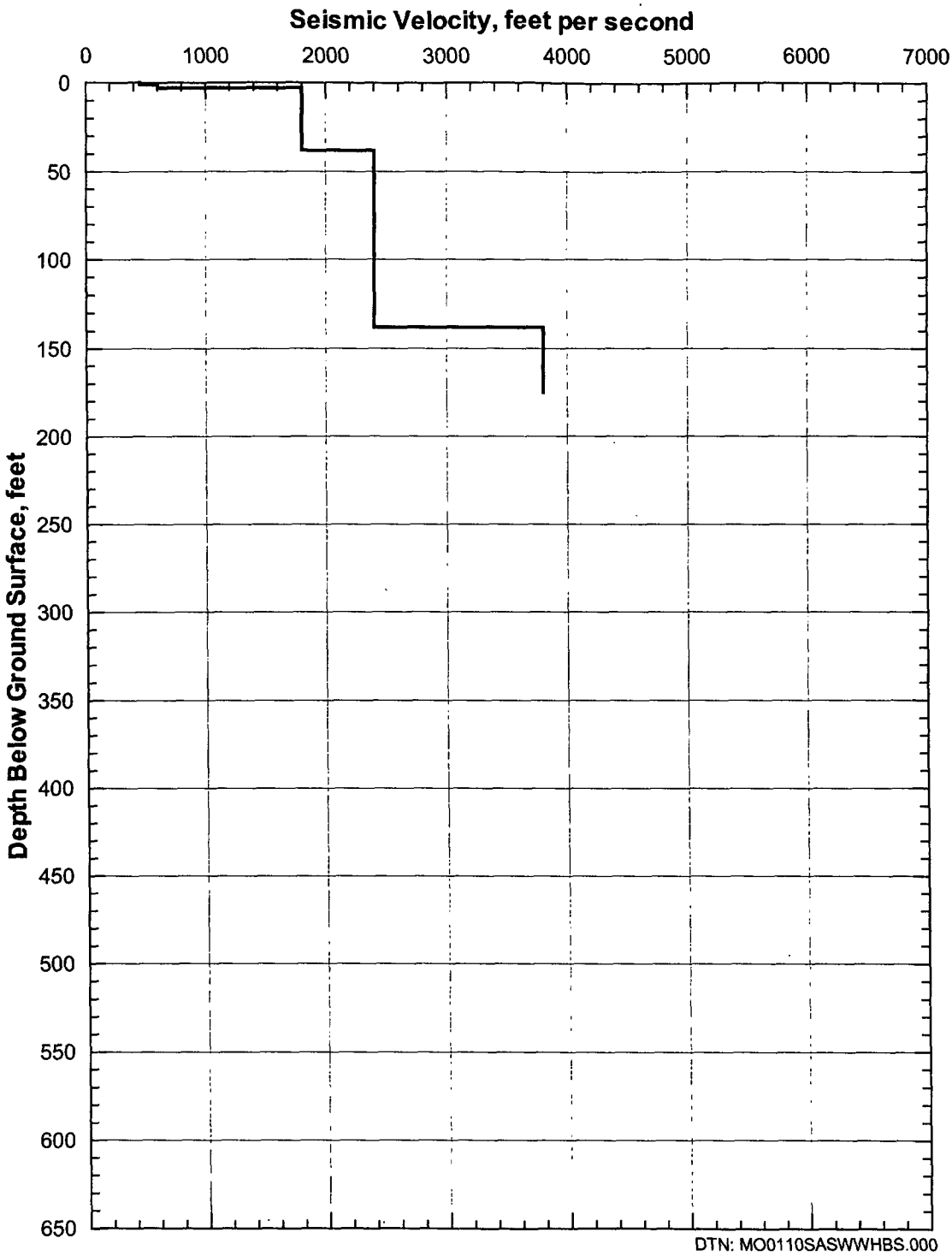

Figure 78. Shear-Wave Velocity Profile from SASW-25

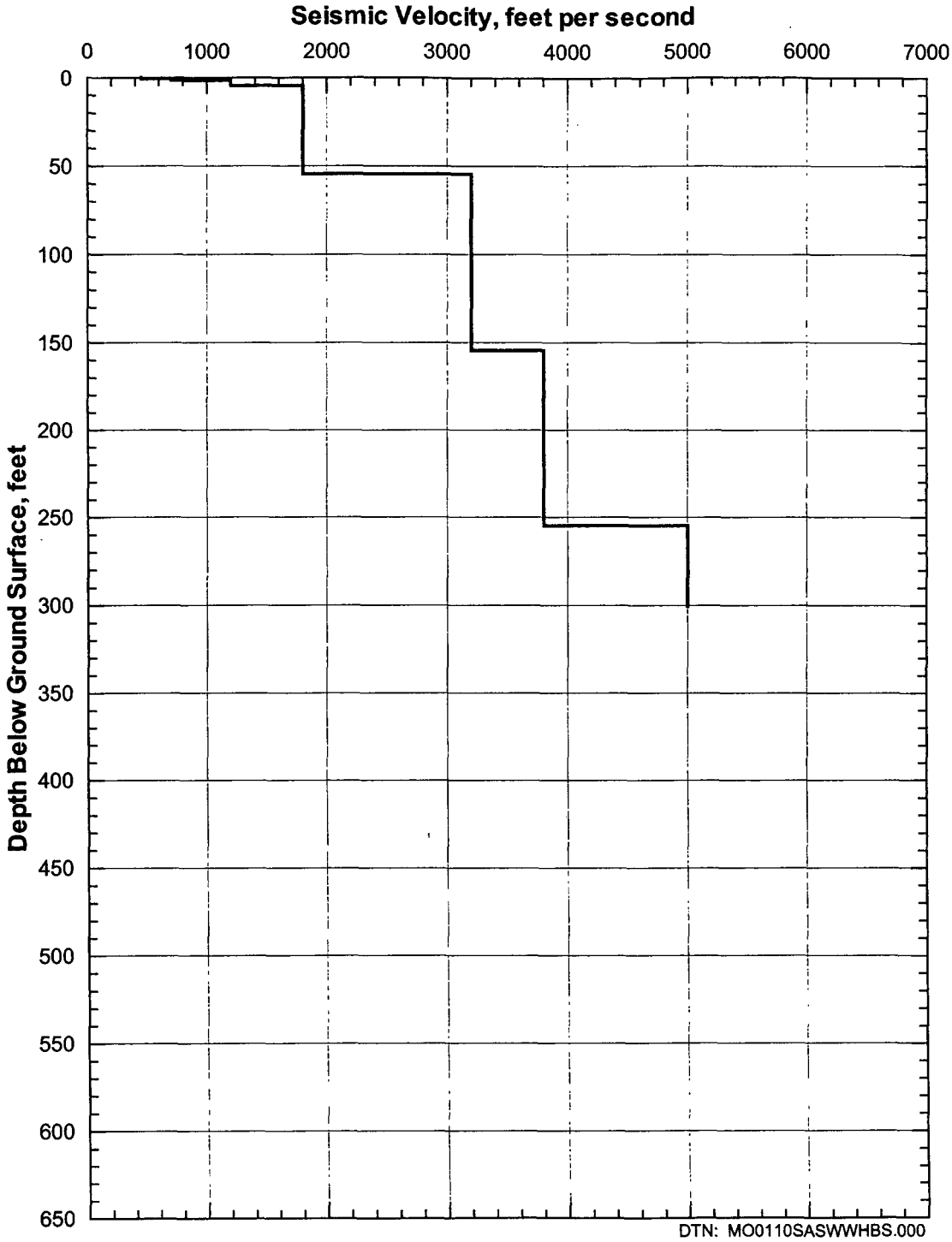

Figure 79. Shear-Wave Velocity Profile from SASW-26

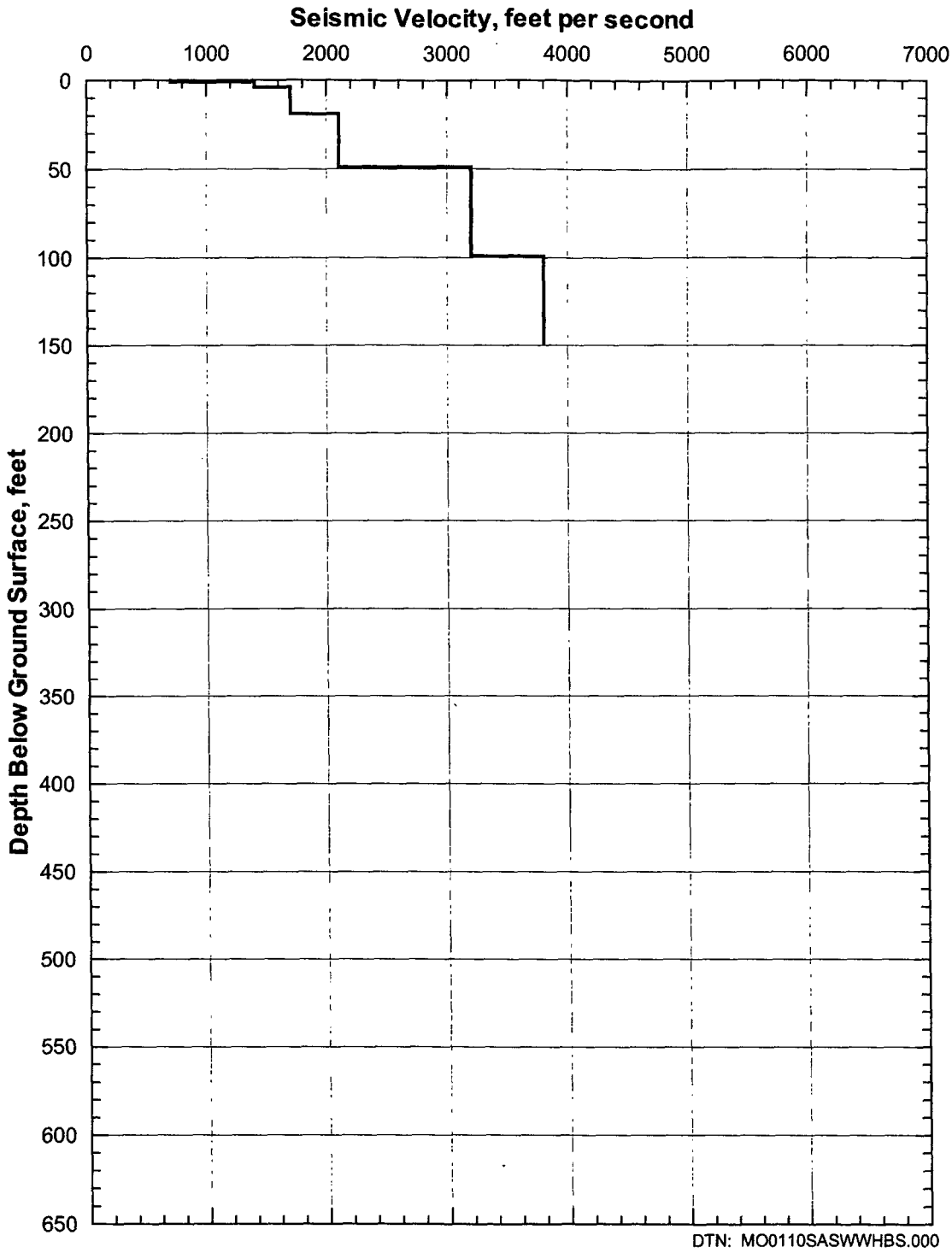

Figure 80. Shear-Wave Velocity Profile from SASW-27

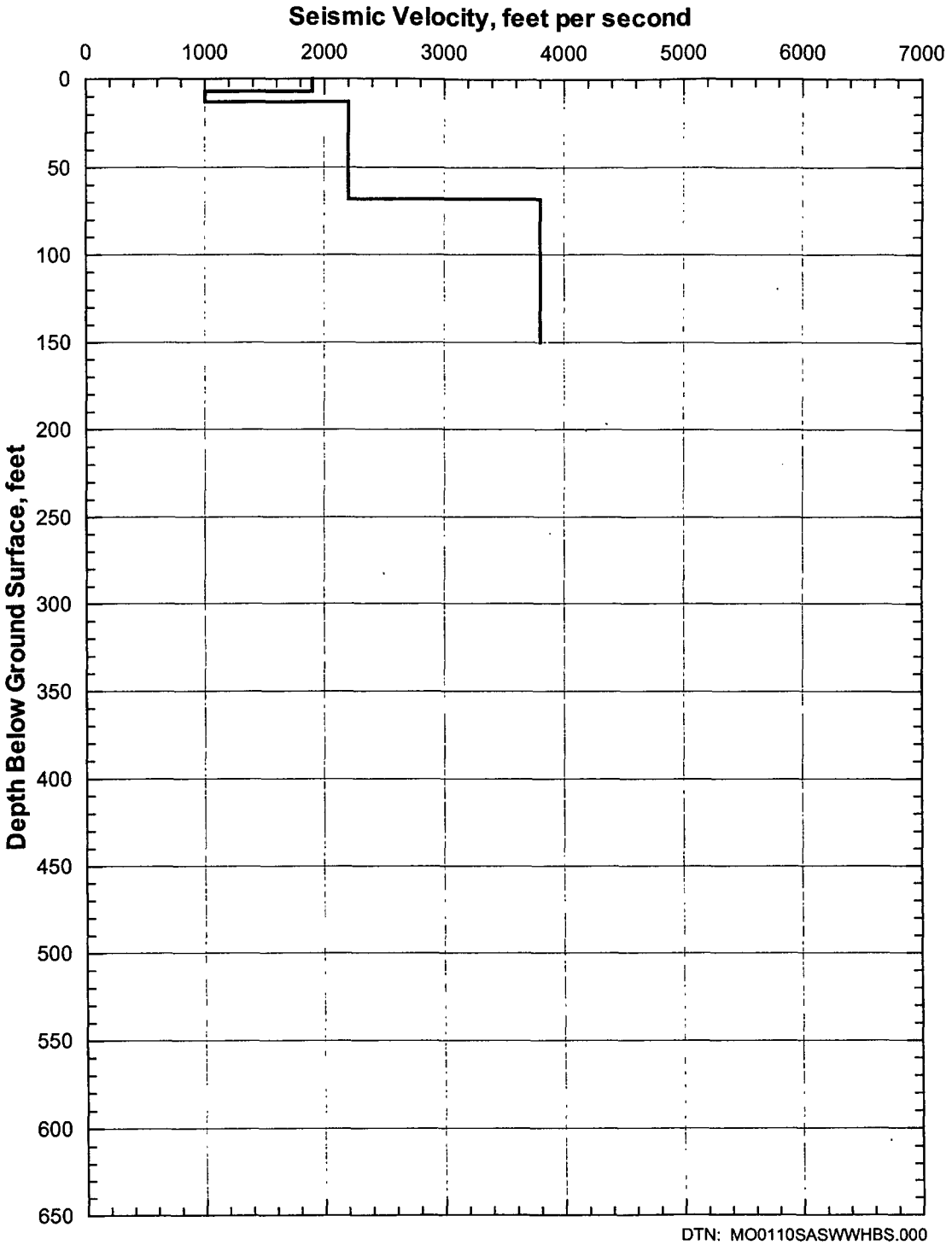

Figure 81. Shear-Wave Velocity Profile from SASW-28

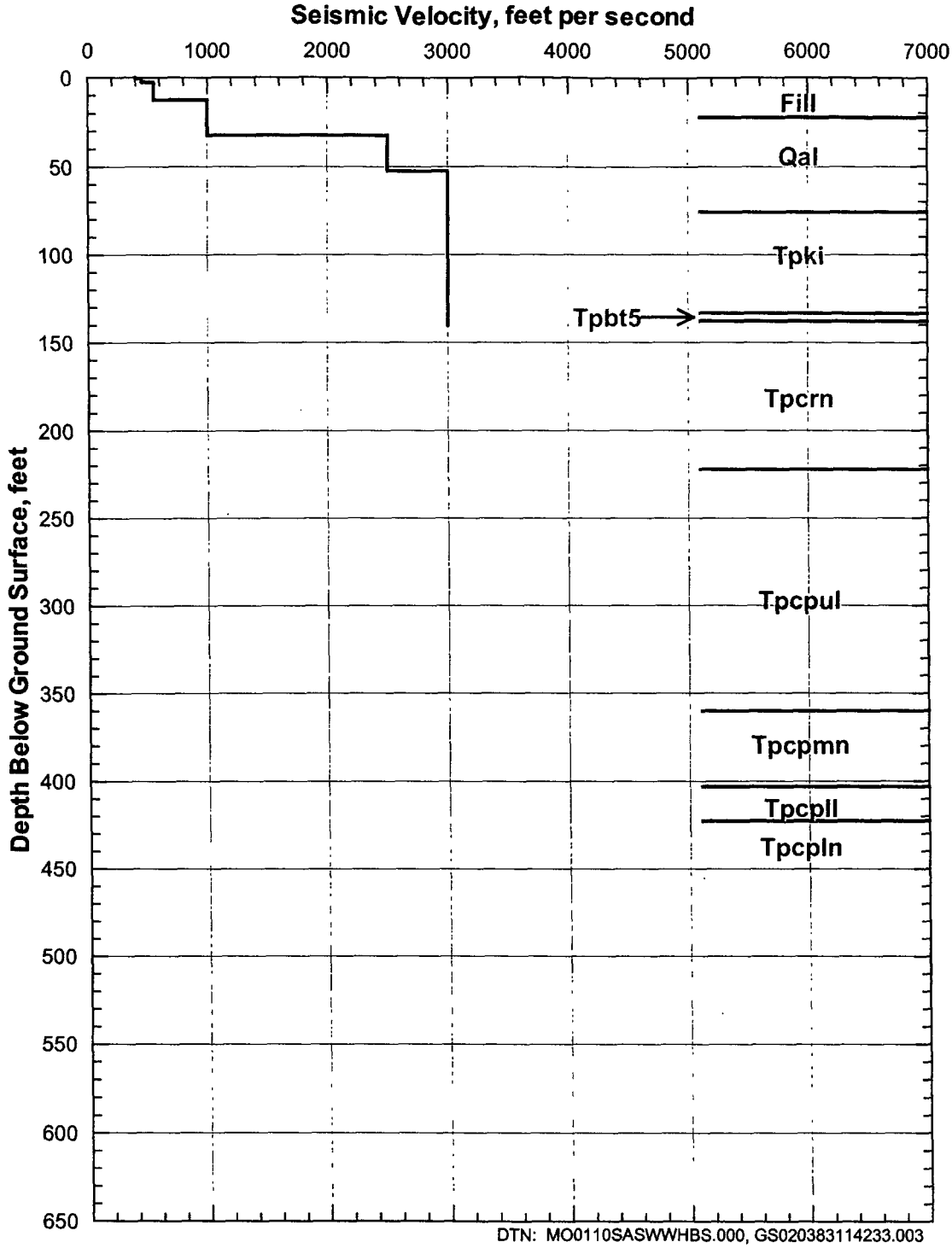

Figure 82. Shear-Wave Velocity Profile from SASW-29 and Generalized Lithology from RF#16

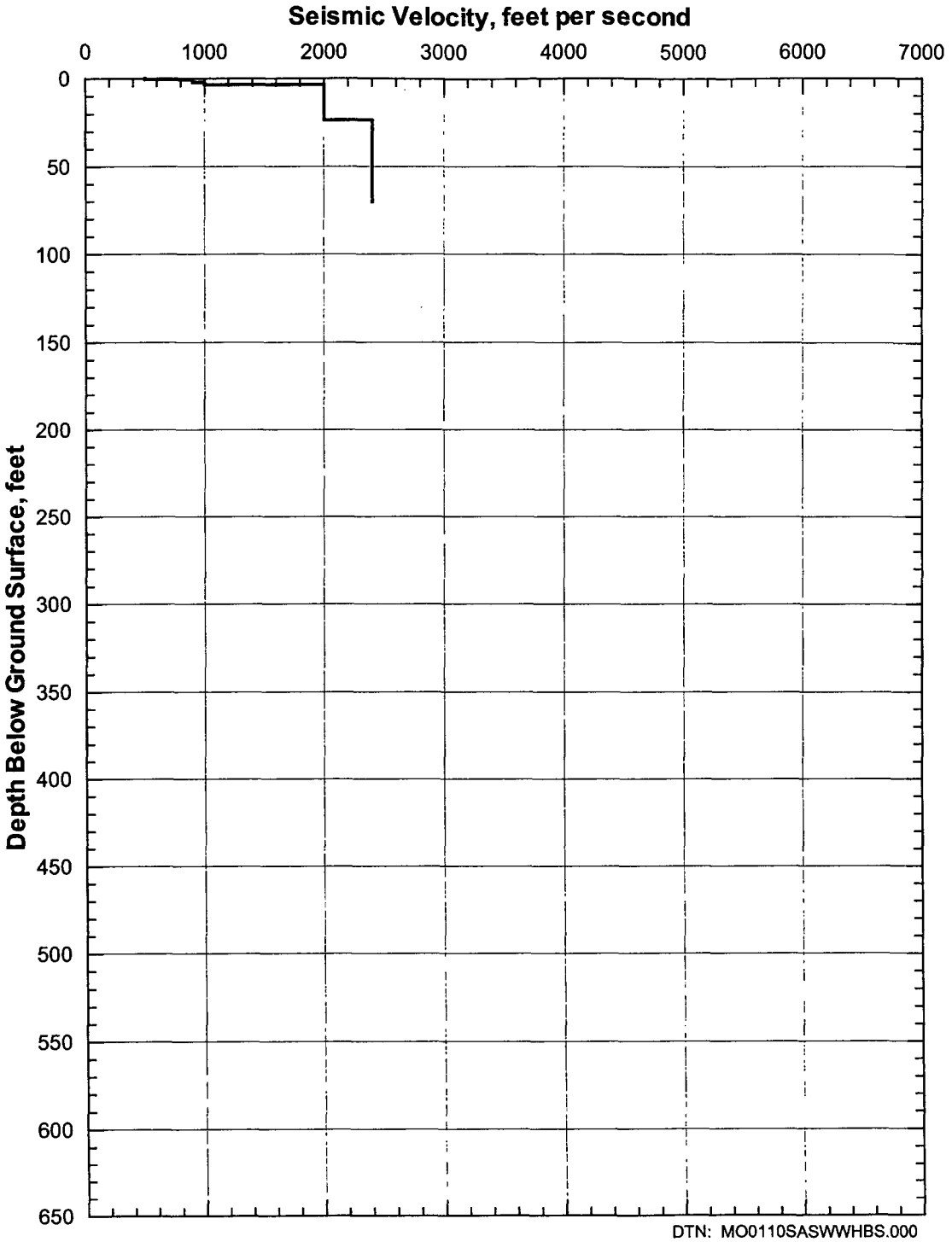

Figure 83. Shear-Wave Velocity Profile from SASW-30

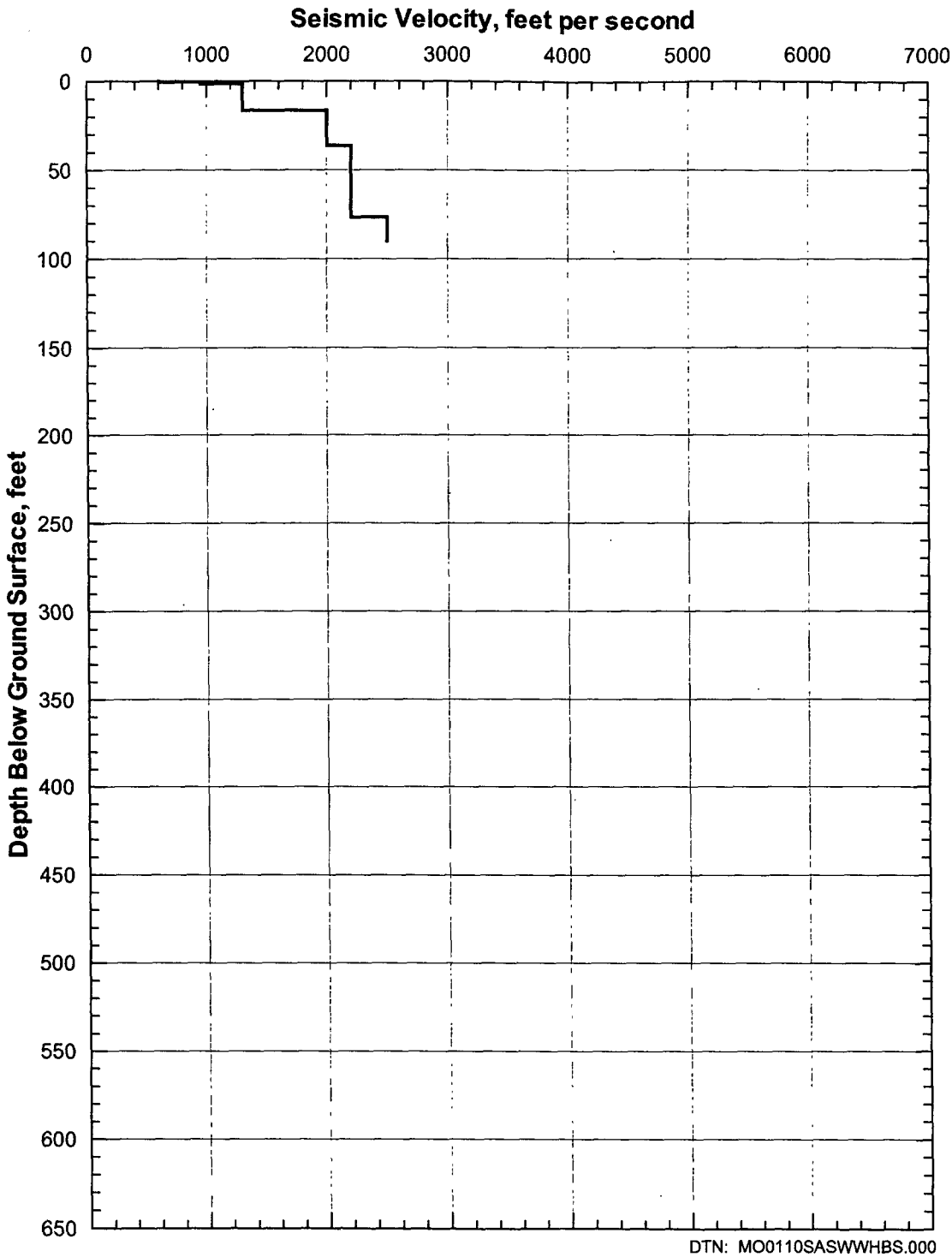

Figure 84. Shear-Wave Velocity Profile from SASW-31

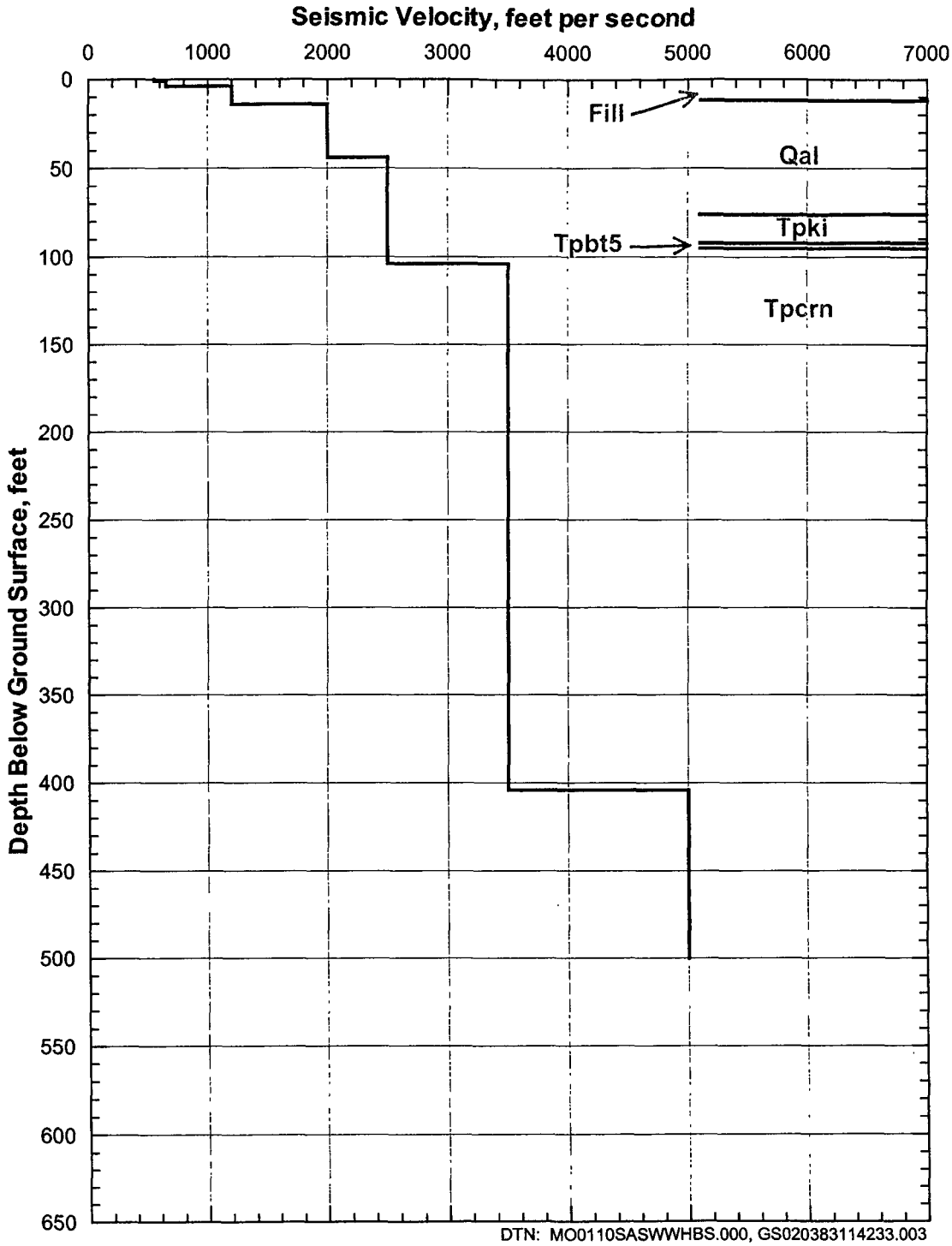

Figure 85. Shear-Wave Velocity Profile from SASW-32+35 and Generalized Lithology from RF#23

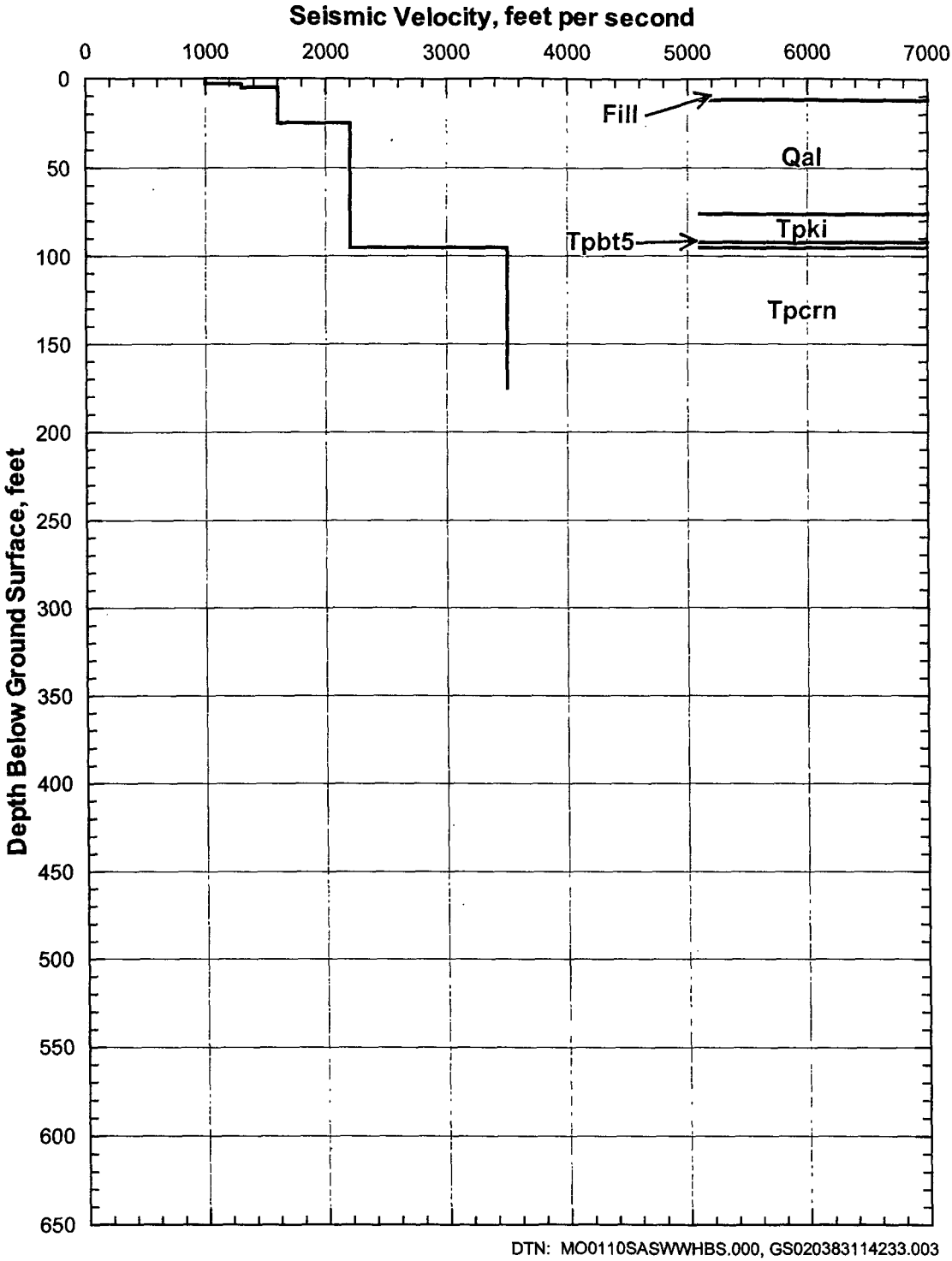

Figure 86. Shear-Wave Velocity Profile from SASW-33

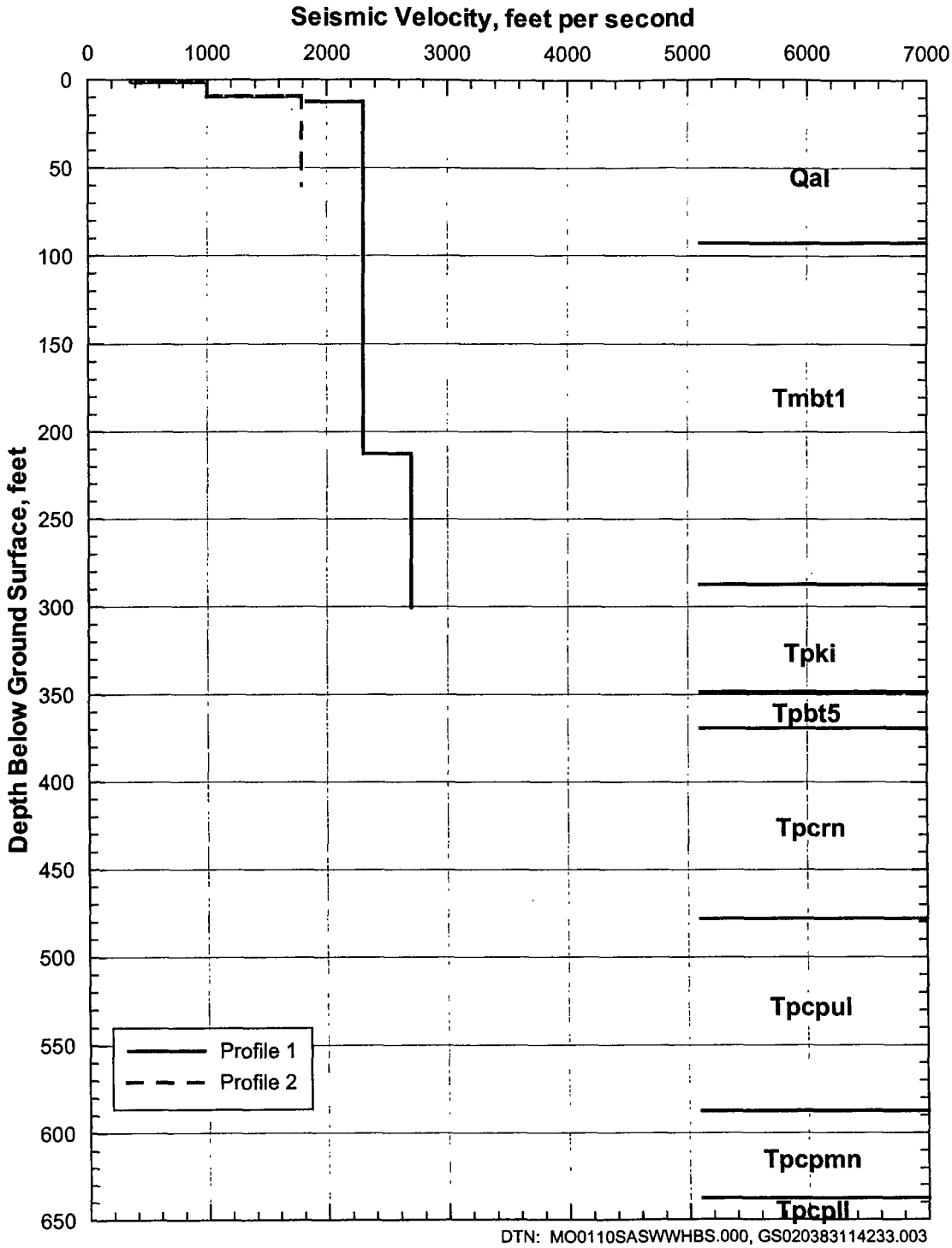

Figure 87. Shear-Wave Velocity Profile from SASW-34+36 and Generalized Lithology from RF#17

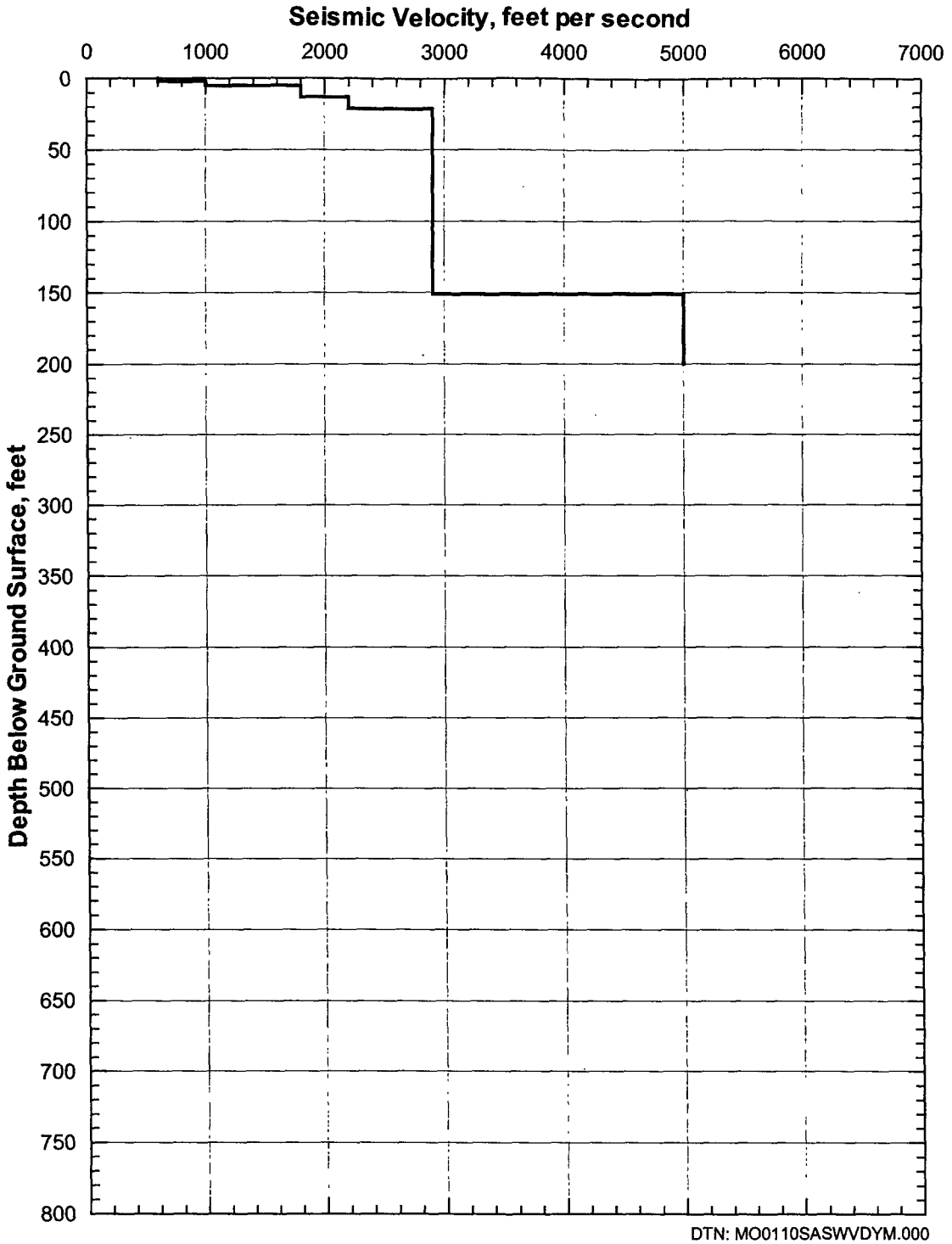

Figure 88. Shear-Wave Velocity Profile from D-12

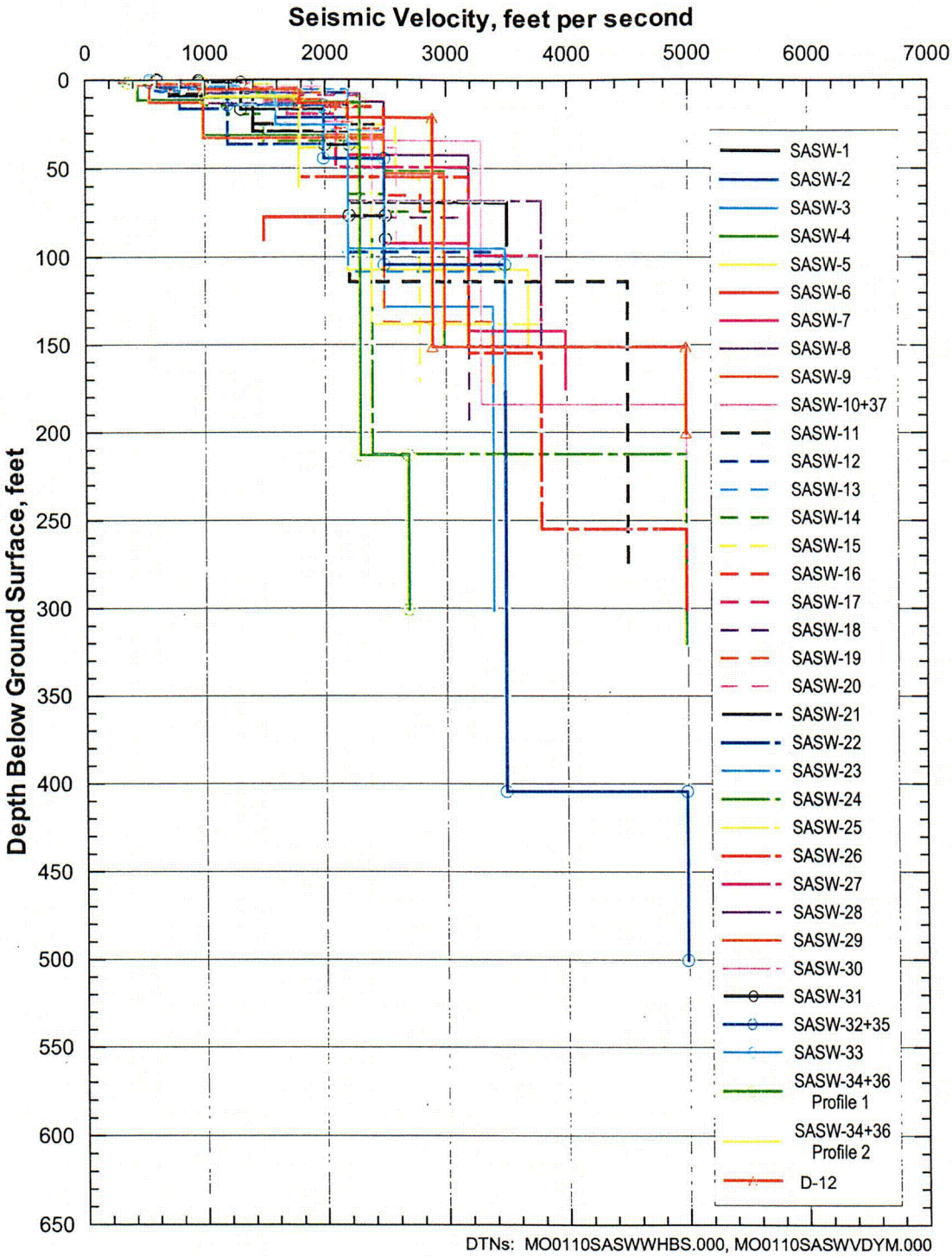

Figure 89. Shear-Wave Velocities from SASW Measurements in the WHB Area

C10

of the surveys (SASW-3, 24, 26, 32+35, and 34+36). The profile for D-12 on Exile Hill is shown on Figure 88. Five profiles (SASW-3, 14, 19, 20, and 34+36) are located off the North Portal pad area and these profiles are shown on Figure 90. For SASW 34+36, the experimental dispersion curve had a portion (from wavelengths of about 30 to 120 ft) where the individual dispersion curves did not overlap. This indicates some lateral changes in velocity. In this wavelength range, there are really two paths for the theoretical dispersion curve to follow and thus, to a depth of about 60 ft, there are two possible profiles. Since the SASW technique is limited to a 1-D model, the two profiles are presented to indicate that there is lateral variability along the extent of the receiver array (Figure 87).

With the exception of SASW 34+36, the five profiles located off the North Portal pad area appear similar to the profiles in the main WHB area (Figures 89 and 90). Most of the profiles start with shear-wave velocities near the surface of less than 1000 ft/s and quickly increase to velocities of 2,500 to 4,000 ft/s at depth. Figure 91 presents the mean, median, and mean ± one standard deviation profiles for all the profiles.

The shear-wave velocity profile for D-12 shows what appears to be a thin 20 ft-thick soil and/or weathered rock over subunits, probably Tpcrn and Tpcpul, of the Tiva Canyon Tuff.

To examine the possible variability in shear-wave velocity profiles throughout the WHB area, average profiles were calculated for three different areas around the pad. Area 1 is located around boreholes RF#16, RF#26, and RF#13 and includes SASW-1, 4, 21, 22, and 29. Figure 92 shows the five individual profiles and the mean profile in Area 1. Area 2 is located around boreholes RF#28 and RF#15 and includes SASW-8, 9, 10+37 and 11. Figure 93 shows the four profiles and the mean profile determined in this area. Lastly, Area 3 is located around boreholes RF#24 and RF#22 and includes SASW-6, 12, 13, 17, 18, 23, and 30. Figure 94 shows the individual profiles and the mean profile determined in Area 3.

The mean profiles from Areas 1, 2, and 3 are plotted together on Figure 95. They do not differ greatly at depths below 40 ft. Area 3 exhibits slightly slower shear-wave velocities at depths of 60 to 95 ft. In the top 40 ft, however, the mean profile in Area 1 is significantly slower than those in Areas 2 and 3, possibly due to the greater thickness of Qal.

As was done for the downhole velocity profiles (Section 6.2.5.3), the mean and plus and minus one standard deviation SASW velocity profiles on the downthrown and upthrown sides of the Exile Hill fault splay in the northeast corner of the WHB site (discussed in Section 6.6.2) are computed (Figures 96 and 97) and compared (Figure 98). SASW-3, 15, 16, 19, 30, 34, and 36 were located on the downthrown side of the fault (Figure 43). The remaining surveys were on the upthrown side. The comparison shows that the shear-wave velocities on the upthrown side of the fault become increasingly higher than the velocities on the downthrown side at depths below about 100 ft (Figure 98). This pattern is very consistent with the stratigraphic cross sections presented in Section 6.6.2, which indicate that to either side of the projected fault plane there is about 100 feet of alluvium. Below the alluvium, slower velocity bedded tuffs and Tuff unit "x" on the downthrown side abut, over a vertical distance of 200 to 300 ft, higher velocity Tiva Canyon Tuff on the upthrown side.

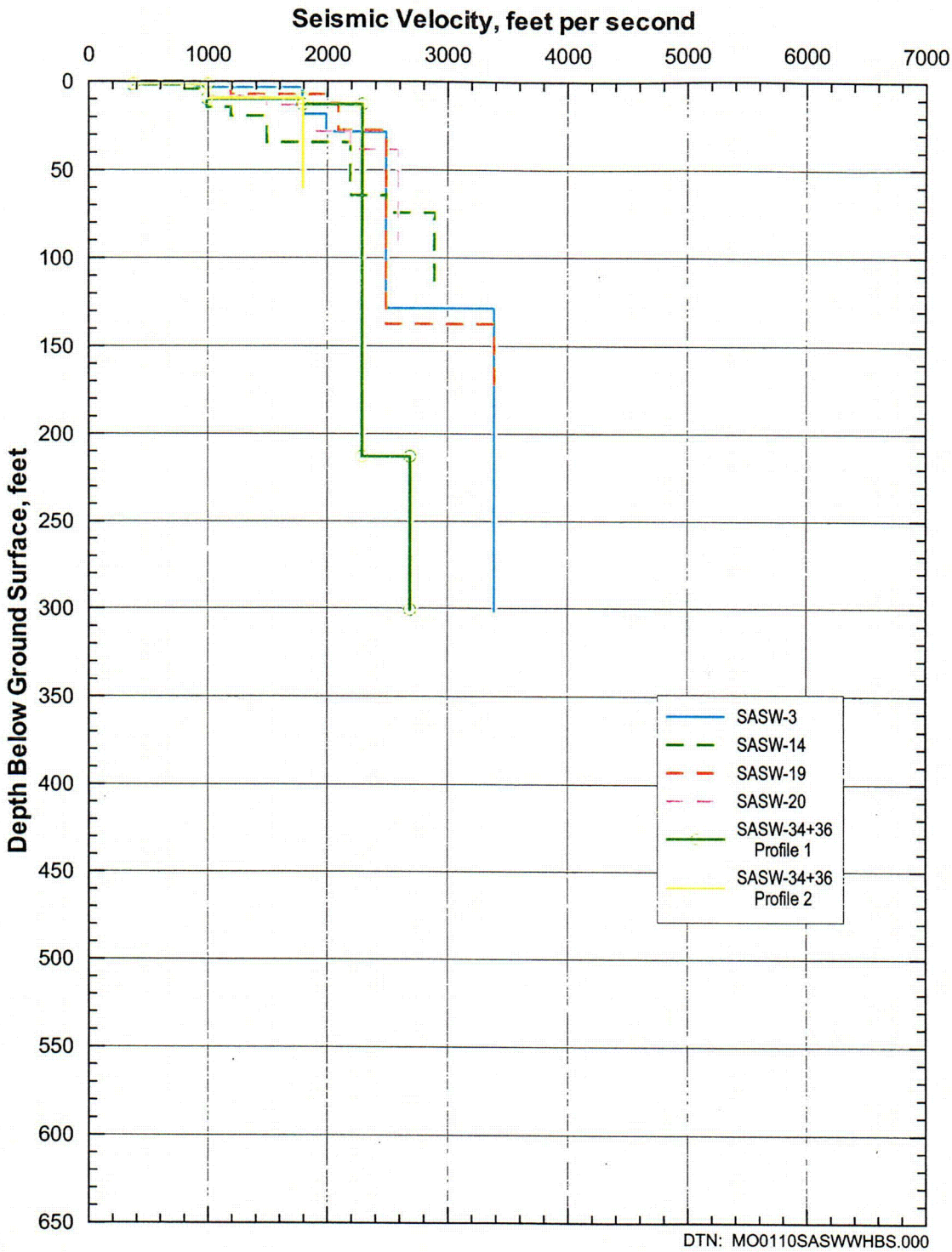

Figure 90. Shear-Wave Velocities from SASW Measurements at Sites Outside of WHB Pad Area

C11

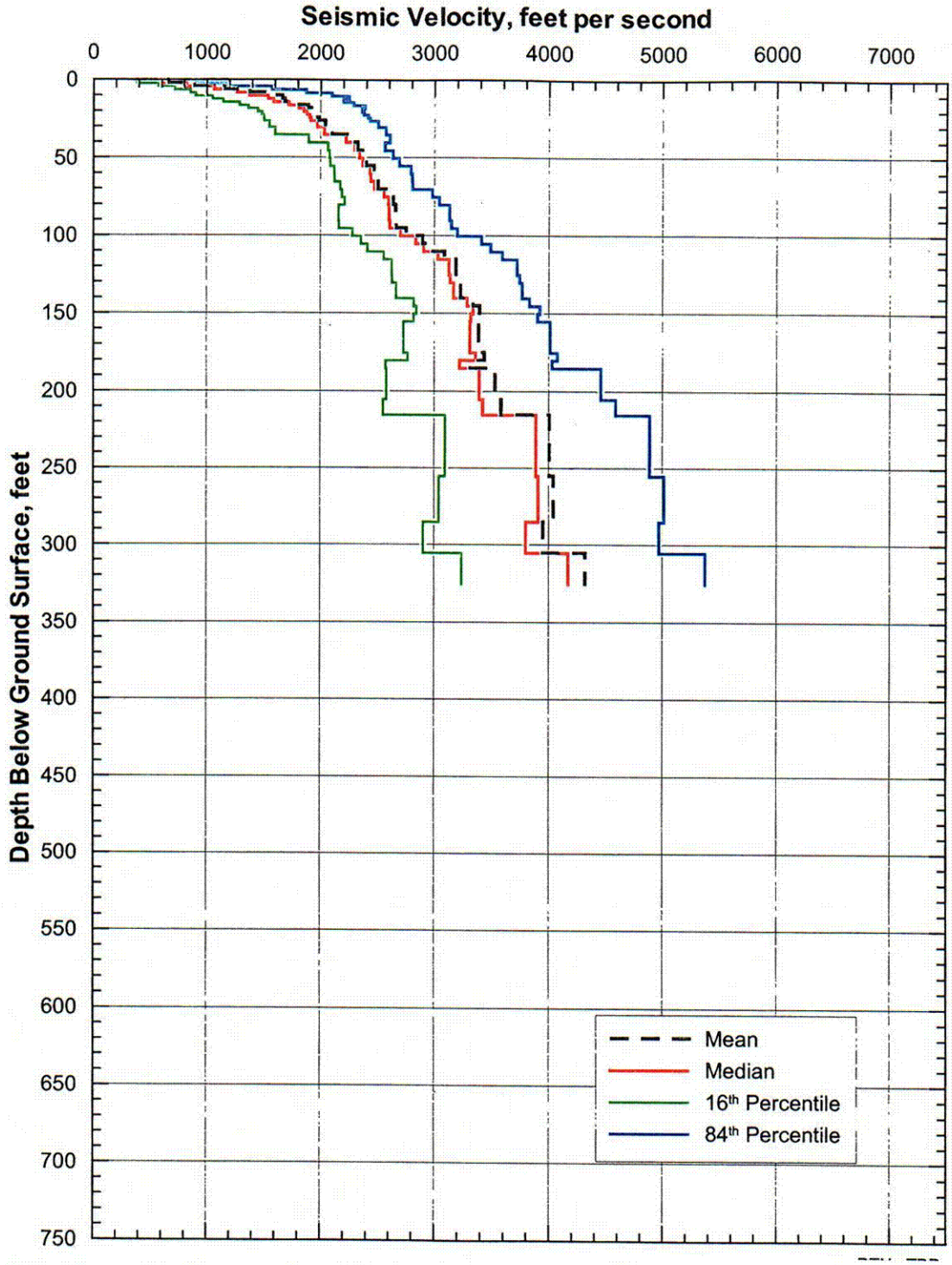

Note: These statistics have been calculated for illustrative purposes only. Final statistics calculated for use in the forthcoming scientific analysis entitled *Development of Seismic Design Input Ground Motions for a Geologic Repository at Yucca Mountain* will be submitted to the TDMS.

Figure 91. Statistical Analyses of Shear-Wave Velocities from SASW Measurements in the WHB Area

C12

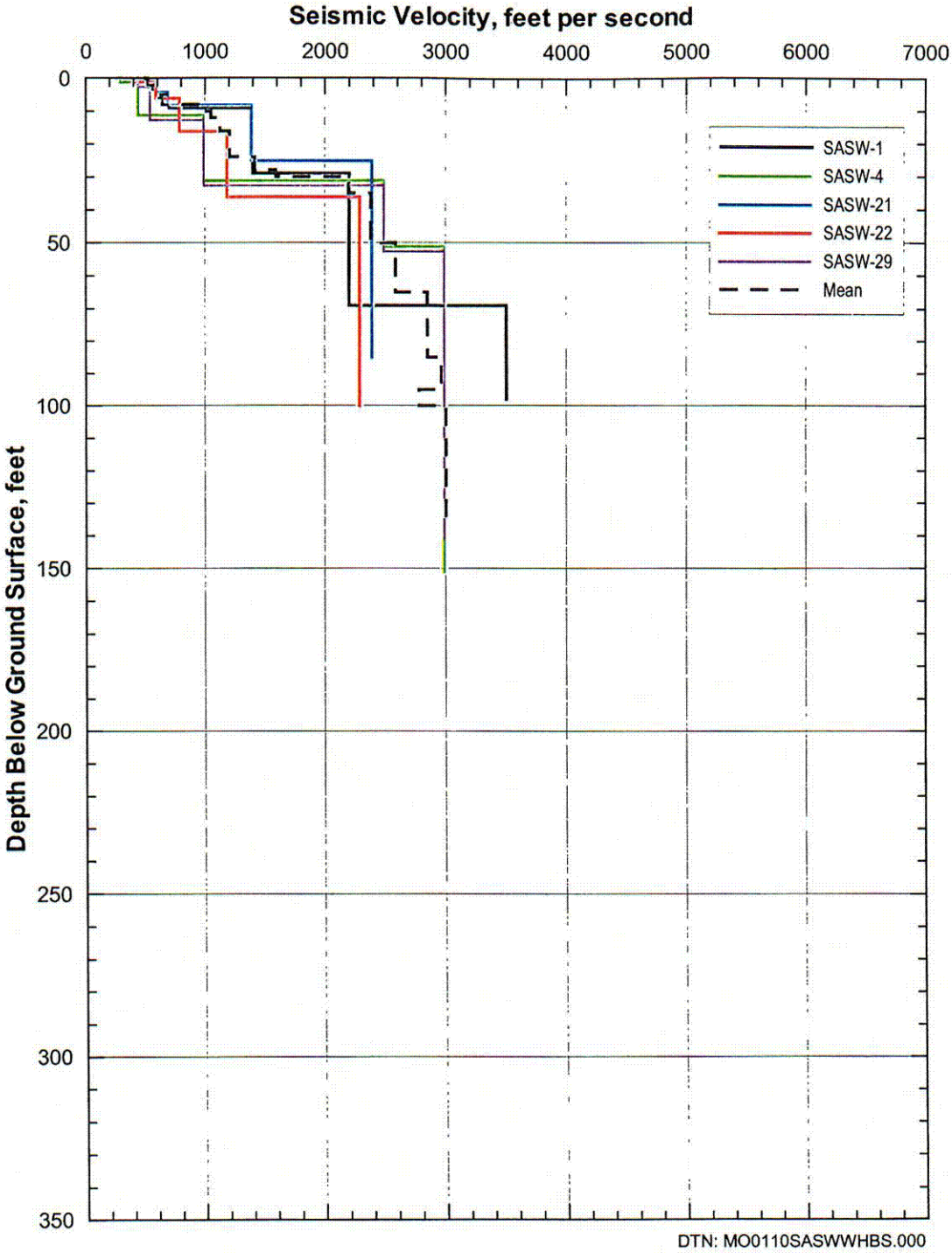

Note: This mean profile has been calculated for illustrative purposes only. Final statistics calculated for use in the forthcoming scientific analysis entitled *Development of Seismic Design Input Ground Motions for a Geologic Repository at Yucca Mountain* will be submitted to the TDMS.

Figure 92. Shear-Wave Velocities from SASW Measurements in the WHB Area (Area 1)

C13

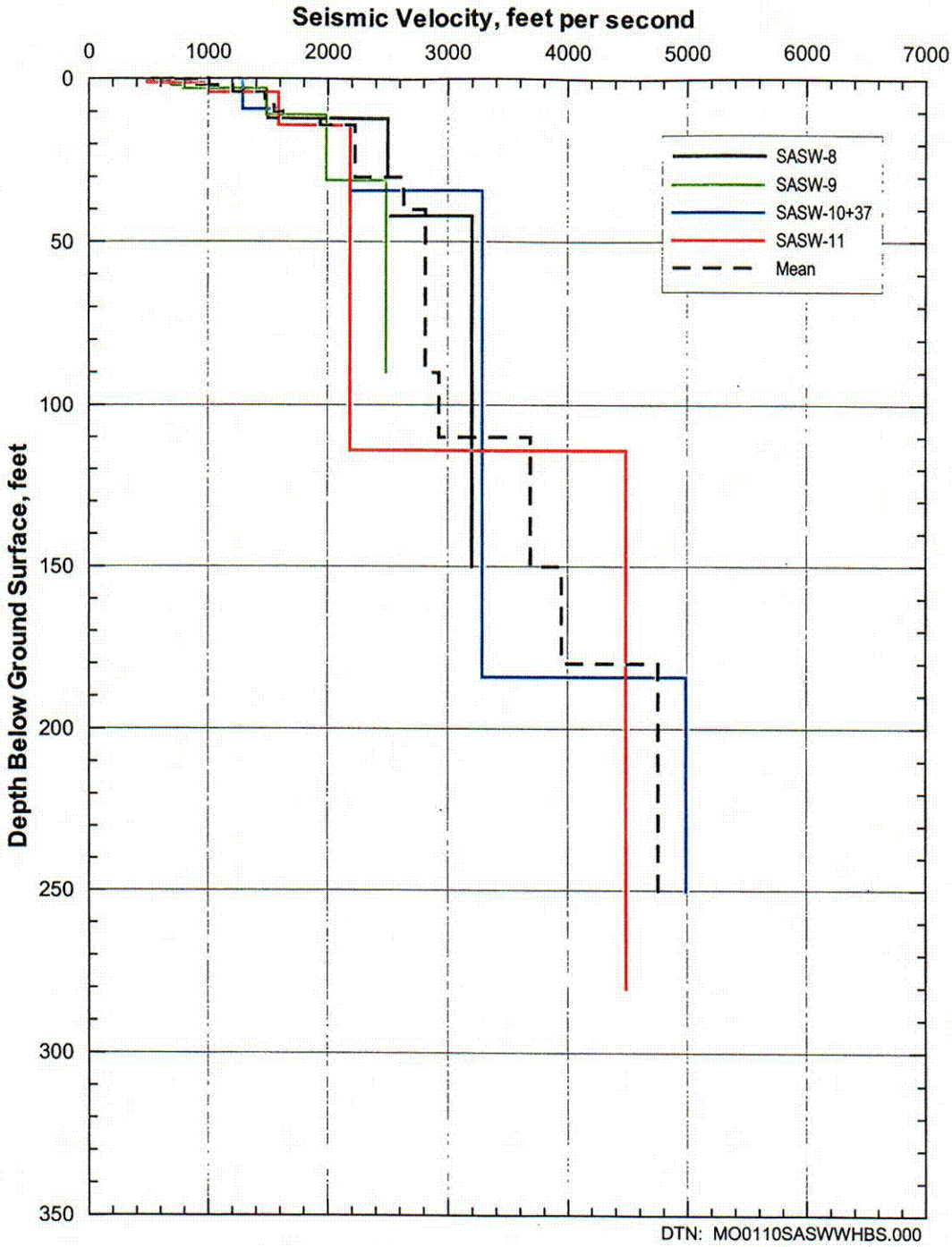

Note: This mean profile has been calculated for illustrative purposes only. Final statistics calculated for use in the forthcoming scientific analysis entitled *Development of Seismic Design Input Ground Motions for a Geologic Repository at Yucca Mountain* will be submitted to the TDMS.

Figure 93. Shear-Wave Velocities from SASW Measurements in the WHB Area (Area 2)

C14

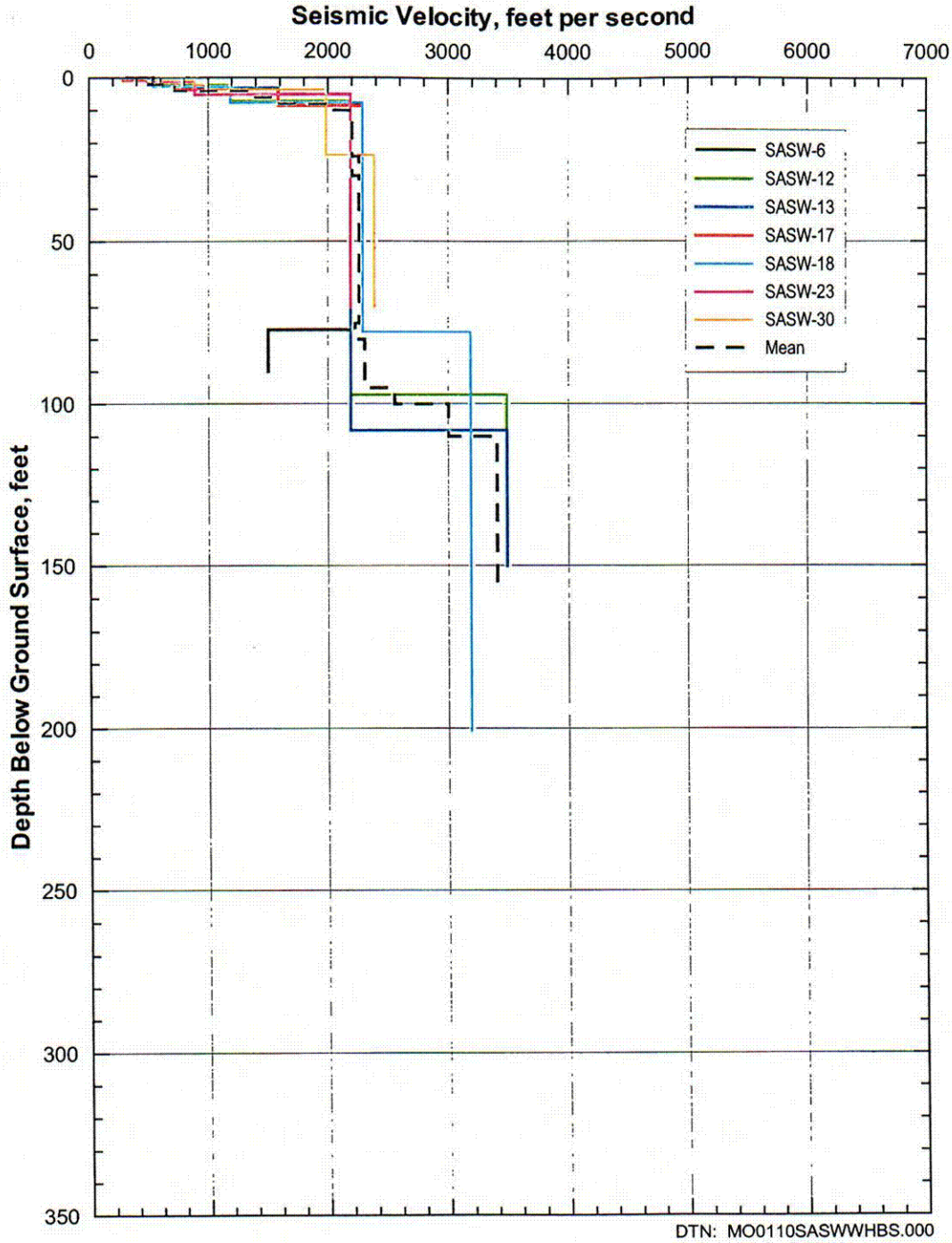

Note: This mean profile has been calculated for illustrative purposes only. Final statistics calculated for use in the forthcoming scientific analysis entitled *Development of Seismic Design Input Ground Motions for a Geologic Repository at Yucca Mountain* will be submitted to the TDMS.

Figure 94. Shear-Wave Velocities from SASW Measurements in the WHB Area (Area 3)

C15

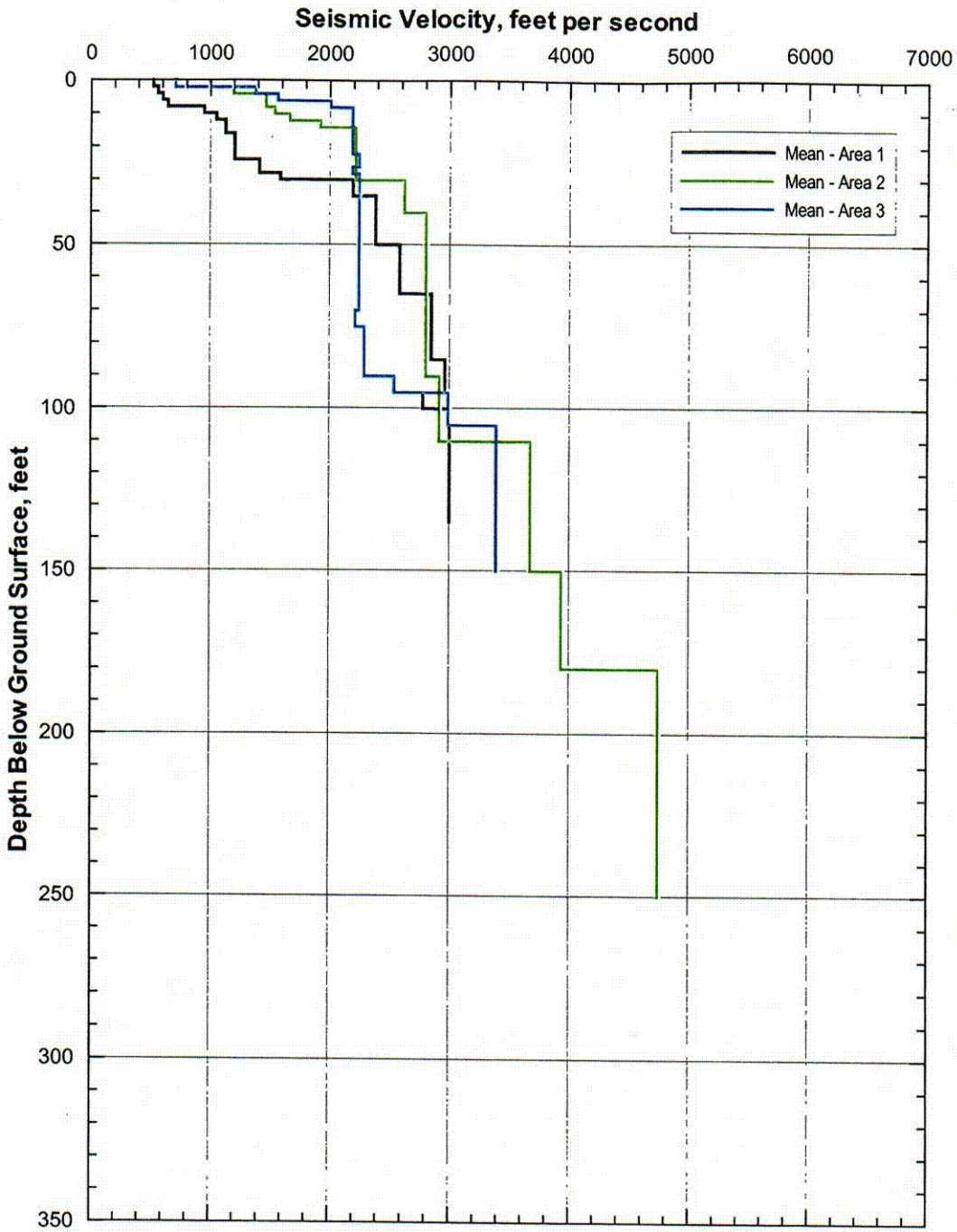

Note: These mean profiles have been calculated for illustrative purposes only. Final statistics calculated for use in the forthcoming scientific analysis entitled *Development of Seismic Design Input Ground Motions for a Geologic Repository at Yucca Mountain* will be submitted to the TDMS.

Figure 95. Comparison of Shear-Wave Velocities from SASW Measurements by Area

C16

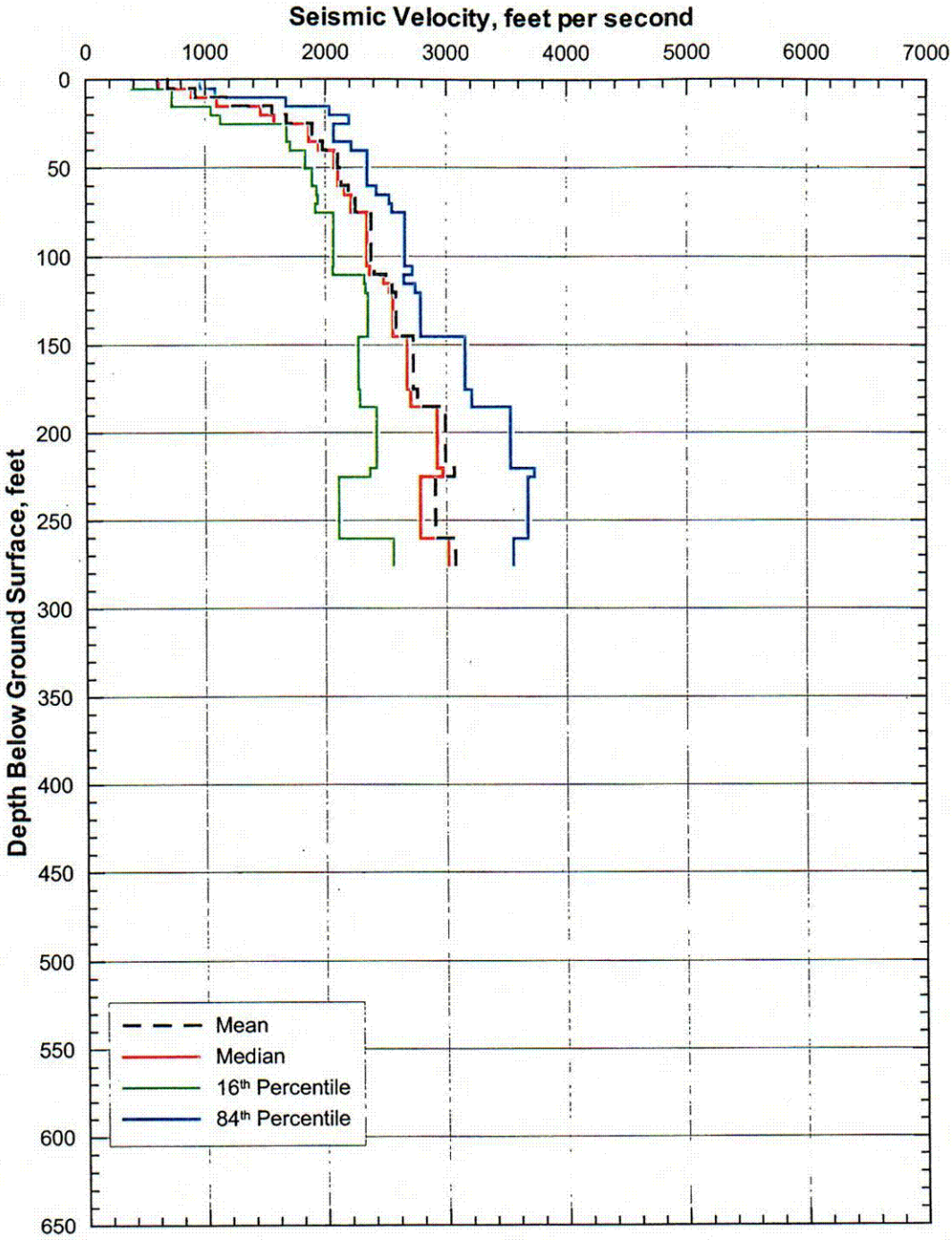

Note: These statistics have been calculated for illustrative purposes only. Final statistics calculated for use in the forthcoming scientific analysis entitled *Development of Seismic Design Input Ground Motions for a Geologic Repository at Yucca Mountain* will be submitted to the TDMS.

Figure 96. Statistical Analyses of Shear-Wave Velocities from SASW Measurements in the WHB Area, Downthrown Side of the Exile Hill Fault Splay

C17

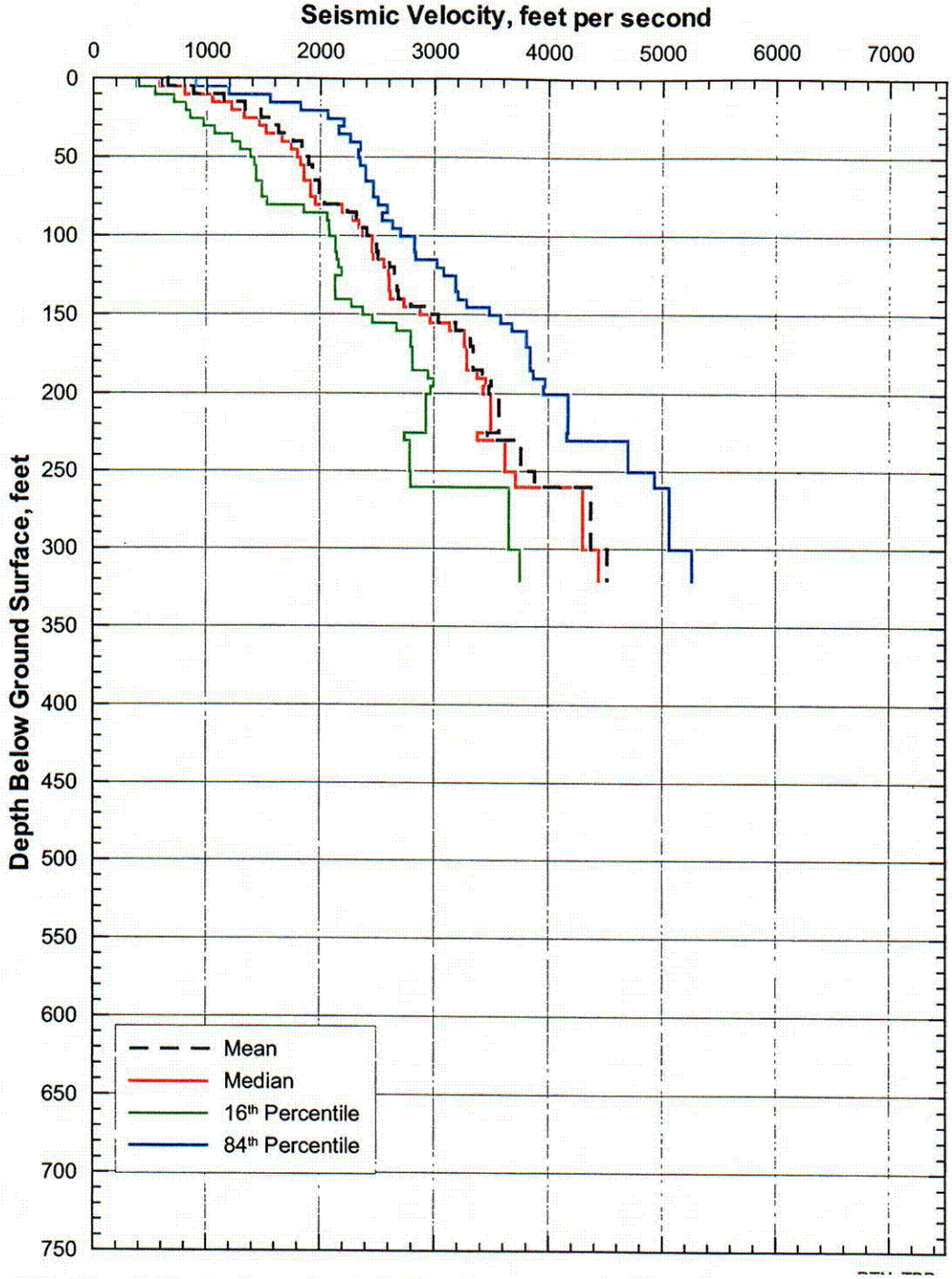

Note: These statistics have been calculated for illustrative purposes only. Final statistics calculated for use in the forthcoming scientific analysis entitled *Development of Seismic Design Input Ground Motions for a Geologic Repository at Yucca Mountain* will be submitted to the TDMS.

Figure 97. Statistical Analyses of Shear-Wave Velocities from SASW Measurements in the WHB Area, Upthrown Side of the Exile Hill Fault Splay

C18

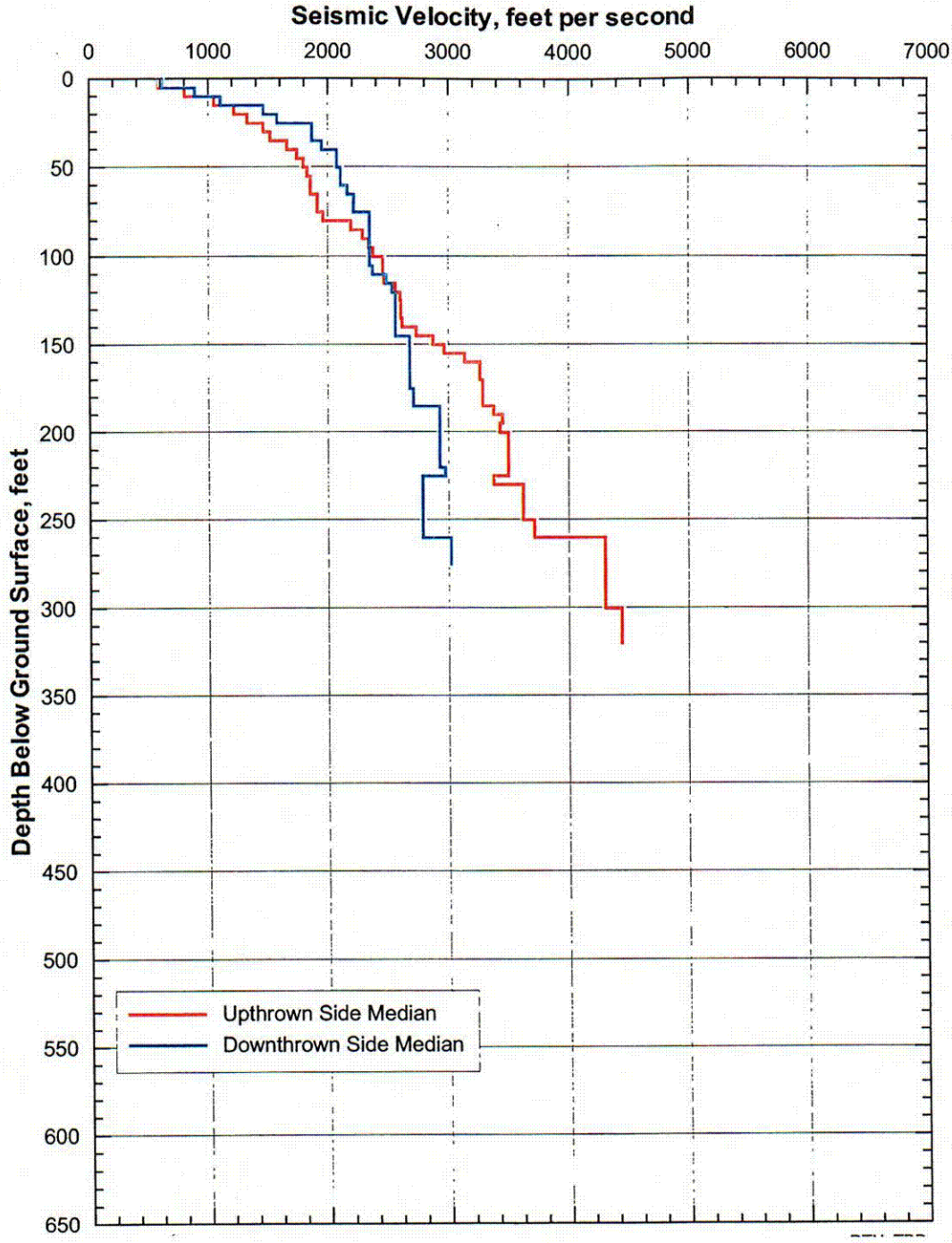

Note: These mean profiles have been calculated for illustrative purposes only. Final statistics calculated for use in the forthcoming scientific analysis entitled *Development of Seismic Design Input Ground Motions for a Geologic Repository at Yucca Mountain* will be submitted to the TDMS.

Figure 98. Comparison of SASW Shear-Wave Velocities Across the Exile Hill Fault Splay

C19

In considering the SASW results, three possible limitations of the methodology should be noted. First, the theoretical model used to determine the shear-wave velocity profile at a site is a one-dimensional layered model. Any lateral variations in shear-wave velocity and layer thickness beneath the extent of the receiver array (hence uniform horizontal layers) are averaged. Therefore, the profile that is presented represents a 1-D layered model that fits the measured dispersion data. It should be noted that lateral variability can be observed qualitatively from mismatches in the individual experimental dispersion curves from adjacent receiver spacings.

Secondly, successful implementation of the SASW method requires that multiple receiver spacings be used at one site. This poses some difficulty when creating a single theoretical dispersion curve to match the experimental dispersion curve. Because the actual receiver spacing is not used, the theoretical dispersion curve is calculated based on the receivers being located 2λ and 4λ (λ is wavelength) from the source. Past studies have shown that these values of receiver spacing do not greatly affect the final shear-wave velocity profile determined at most sites (Joh 1996).

Finally, it is also important to note that as the wavelength used in the SASW methodology increases, and hence as the depth of penetration increases, the surface wave propagates through a greater volume of material. The resolution of the SASW method (ability to detect changes in velocity and thickness at depth) decreases as the wavelength increases. Therefore, the resolution is best near the surface and lowest at the greatest depths in the profile. For these analyses, the shear-wave velocity profiles are presented to a maximum depth of approximately 0.5 times the longest wavelength recorded in the field. The maximum profile depth is based on the fact that most of the surface wave particle motion is occurring at depths less than 0.5 times the longest wavelength. The step-wise shear-wave model used in the SASW analysis reflects the general trend in the shear-wave velocities to this depth (0.5 times the longest wavelength). For the SASW surveys near the WHB, the shear-wave profile is well resolved to depths within the range of approximately 75 to 125 ft. At greater depths, the trend in the shear-wave velocity profile is accurately reflected, but the absolute depths and relative changes in shear-wave velocities at interfaces are less well resolved.

6.2.8 Borehole Wireline Geophysical Surveys

Caliper and gamma-gamma wireline surveys were performed by Schlumberger Limited in boreholes RF#16, RF#18, RF#20, RF#21, RF#22, RF#24 and RF#28. These seven boreholes were the ones that were available for logging at the time when the subcontractor was mobilized to the site. The locations of these boreholes are shown on Figure 2 in Section 6.2.2. The processes established in AP-SIII.5Q, *Yucca Mountain Site Characterization Project Field Verification of Geophysical Operations*, and AP-SIII.6Q, *Geophysical Logging Programs for Surface-Based Testing Program Boreholes*, were followed for both the caliper and gamma-gamma wireline surveys. The main purpose in performing the caliper measurements was to quantitatively assess the extent of erosion of the borehole walls by the drilling fluid, as this was found to be a factor affecting data acquired from borehole RF#13 (see Section 6.7.2 for a discussion of the erosion in borehole RF#13 and the potential effects of that on the suspension seismic results). The main purpose of performing the gamma-gamma measurements was to evaluate the density of the subsurface materials. It was also hoped that the density values would help with identification of the lithostratigraphic units.

The caliper surveys utilized a four-arm caliper, yielding borehole diameter measurements in two orthogonal directions. One pair of arms usually aligns itself with the major axis of an elliptical borehole, and the other with the minor axis (Schlumberger Educational Services 1987, page 42). The caliper logs indicate divergences between the borehole dimensions and the drill bit size, which may reflect rock fractures or erosion of the borehole walls by the drilling fluid. However, borehole ellipticity can result from other factors, including directional drilling, deviated borehole, drilling at an acute angle to bedding, and an oriented pore structure (Schlumberger Educational Services 1987, page 42).

The gamma-gamma density measurement involves emitting a known number of gamma rays from a radioactive source and counting the number of gamma rays arriving at a detector. After leaving the source, the gamma rays collide with electrons in the material surrounding the borehole, causing the gamma rays to lose some of their energy before continuing in a different direction. The percentage of gamma rays arriving at the detector is related to the density of electrons in the formation (electrons per cubic centimeter) and thus to the formation bulk density.

The boreholes were advanced using drilling mud to support the opening. To minimize the effect of the mudcake on the borehole walls, the source and detectors were mounted on a skid and shielded. The shielded openings were pressed against the borehole walls by an eccentering arm. The force applied by the arm and the plow-shaped design of the skid help the skid to cut through soft mudcakes.

Any mud or mudcake remaining between the source and the formation or between the detectors and the formation affect the gamma rays and must be taken into account. In the dual-detector Formation Density Logging Device (FDLD) shown on Figure 99, mudcake compensation is effected by the use of two detectors with different source-detector spacing and hence different depths of formation penetration. The acquisition software uses data from both detectors to compute a bulk density value (ρ_b) and the correction ($\Delta\rho$). This process is illustrated in the "spine and ribs" charts on Figure 100.

Figure 100 provides the overall concept of the dual-detector correction process using what is referred to as the "spine and ribs" method. The t_{mc} is the mudcake thickness, ρ_b is the bulk density of the formation, ρ_{mc} is the actual bulk density of the mudcake and ρ^+_{mc} is the apparent density of the mudcake. While the design of the tool removes the influence of electron density from the measurement of bulk density of the formation, the same is not true for the mudcake density. The apparent density of the mudcake, ρ^+_{mc}, combines the influence of both the bulk density of the mudcake and the electron density.

The "spine" is shown in (a) where mudcake thickness is zero and the detector responses are only a function of variations in the formation density.

In (b), for a constant ρ^+_{mc} (=1.5 gm/cc) and a constant ρ_b (=2.5 gm/cc), the departure from the true bulk density, resulting from increasing mudcake thickness, follows a line that leads to, at infinite mudcake thickness, 1.5 gm/cc.

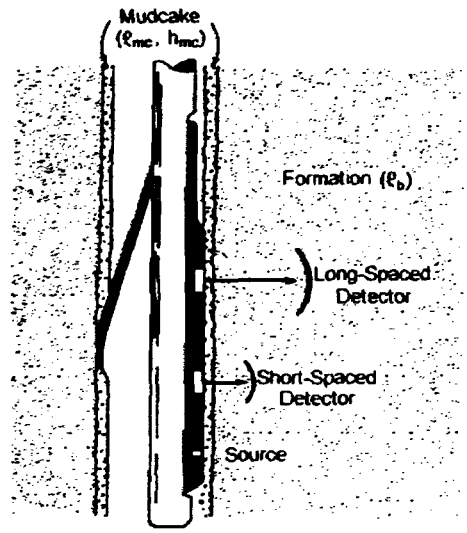

Source: Wahl et al. (1964, page 1411)

Figure 99. Schematic Diagram of Dual-Detector Formation Density Logging Device

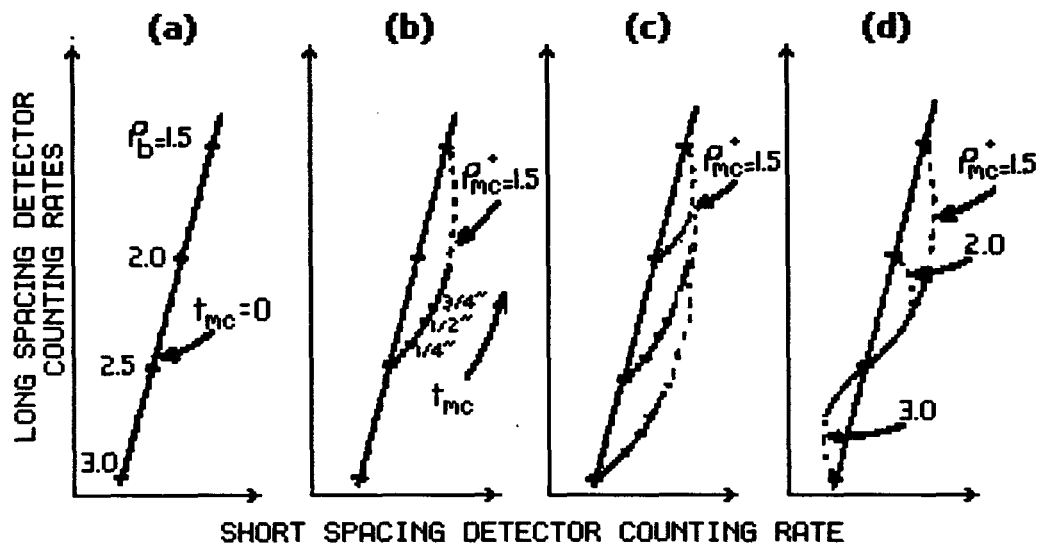

Source: Wahl et al. (1964, page 1413)

Figure 100. "Spine and Ribs" Plot Used To Compute Bulk Density And Density Correction From Dual Detector Density Tools

In (c), ρ^+_{mc} is constant at 1.5 gm/cc while both t_{mc} and ρ_b are varied. The three curved lines emanating from bulk density values of 2.0 gm/cc, 2.5 gm/cc, and 3.0 gm/cc represent increasing t_{mc}. Once again, when the mudcake thickness becomes infinite, all three ρ_b values converge at the bulk density value of the mudcake.

In (d), varying thickness of three different values of ρ^{+}_{mc} (1.5 gm/cc, 2.0 gm/cc, and 3.0 gm/cc) are superimposed on a formation having ρ_b=2.5 gm/cc. When ρ^{+}_{mc} is greater than ρ_b the mudcake curve falls down and to the left of the "spine". This indicates that mudcake curves exist on both sides of the "rib" and can be corrected in the same manner. When the mudcake curves are cut off at the point they begin to separate, the "ribs" of the plot become apparent.

The result is that for each value of ρ_b, all mudcake curves leaving one side of the "spine" can be described, for the normal ranges of mudcake thickness, by a single algorithm. This means that, by proper tool design, the correct formation density can be determined by the counting rates of the two detectors.

The above discussion was developed to describe the compensation routine used with the early borehole compensated density tools. The modern density tools still use a dual-detector system along with the "spine and ribs" correction. For moderate borehole rugosity or mudcake, the slope of the line passing through the value for the correct bulk density and the density measured from each detector is virtually the same for the usual densities and thicknesses of intervening materials separating the detectors and the formation wall. This provides a means for estimating the amount of correction to be added to or subtracted from the measured response from the long-spacing detector.

DTN: MO0112GPLOGWHB.001 summarizes the results of the borehole geophysical surveys in tabular format, and these data are shown on the figures in Attachment X. Table 12 and Figure 101 summarize the data. Figure 101 plots the total density as a function of depth bgs, and identifies the lithostratigraphic unit and borehole with different symbol colors and symbol shapes, respectively. With all boreholes considered together, little trend of density with depth can be discerned. However, if the data from borehole RF#22, located north of the Exile Hill fault splay, are considered separately from the data from boreholes located southwest of the Exile Hill fault splay, a trend of increasing density with depth can be observed in the data from southwest of the Exile Hill fault splay. Another can be observed between density and lithostratigraphic unit. Table 12 summarizes the mean and coefficient of variation of the total density values by lithostratigraphic unit.

6.2.9 Geotechnical Laboratory Static Testing

As discussed in Section 6.2.4, four test pits, WHB-1 through –4, were excavated in the WHB area. In-situ density tests were performed in each of the test pits, as described in Section 6.2.4. Most of the material from those tests was placed in lined canvas sacks, but a part of the material excavated in each 6-foot ring test and all material from 20-inch sand cone density tests was placed in sealed plastic buckets to help preserve the specimen's as-tested water content. The samples were shipped to a geotechnical laboratory in Denver, CO, where additional tests were performed in order to classify the material according to the USCS (see USBR 5000-86) and to determine the in-place relative density.

Table 12. Statistical Summary of Density Measurements by Lithostratigraphic Unit

Unit (Symbol)	RF#16	RF#18	RF#20	RF#21	RF#22	RF#24	RF#28	All
Fill								
Data Interval, ft	9-22	--	11.0-28.0	--	--	--	--	
Minimum, lbm/ft^3	98.26		109.75					98.26
Maximum, lbm/ft^3	131.29		124.11					131.29
Mean, lbm/ft^3	112.09		117.91					115.37
Standard Deviation, lbm/ft^3	9.50		3.24					7.26
Count	27		35					62
Qal				(see Note 2)				
Data Interval, ft	22.5-75.5	7.0-59.5	28.5-97.5	7.0-115.0	7.0-80.0	10.0-30.0	5.0-15.0	
Minimum, lbm/ft^3	105.75	96.95	110.37	80.91	104.50	113.24	93.89	80.91
Maximum, lbm/ft^3	129.29	126.48	126.73	123.42	129.41	122.30	127.79	129.41
Mean, lbm/ft^3	114.13	117.43	118.71	111.24	119.51	118.20	110.12	115.71
Standard Deviation, lbm/ft^3	4.51	5.34	3.61	9.51	3.80	2.70	8.76	7.14
Count	107	106	139	217	147	41	21	778
Tmbt1								
Data Interval, ft	--	60.0-64.5	--	--	80.5-318.0	--	--	
Minimum, lbm/ft^3		109.44			96.51			96.51
Maximum, lbm/ft^3		125.29			130.35			130.35
Mean, lbm/ft^3		117.13			109.67			109.83
Standard Deviation, lbm/ft^3		5.62			5.32			5.42
Count		10			476			486
Tpki								
Data Interval, ft	76-133	65.0-204.0	--	--	318.5-409.5	--	--	
Minimum, lbm/ft^3	86.46	86.03			98.51			86.03
Maximum, lbm/ft^3	111.18	113.43			115.18			115.18
Mean, lbm/ft^3	95.08	96.63			102.76			98.26
Standard Deviation, lbm/ft^3	7.48	4.43			2.52			5.69
Count	115	279			183			577

F:\YMP\4200\data\schlumberger

Table 12. Statistical Summary of Density Measurements by Lithostratigraphic Unit (Continued)

Unit (Symbol)	RF#16	RF#18	RF#20	RF#21	RF#22	RF#24	RF#28	All
Tpbt5								
Data Interval, ft	133.5-137.5	--	98.0-102.0	--	--	--	--	
Minimum, lbm/ft^3	85.09		119.36					85.09
Maximum, lbm/ft^3	113.62		123.67					123.67
Mean, lbm/ft^3	102.00		121.43					111.71
Standard Deviation, lbm/ft^3	11.84		1.51					12.92
Count	9		9					18
Tpcrn (see Note 1)								
Data Interval, ft	138.0-222.0	204.5-292.0	102.5-118.0	115.5-155.0	--	30.5-110.0	15.5-70.0	
Minimum, lbm/ft^3	87.34	95.08	96.45	87.34		97.26	106.13	87.34
Maximum, lbm/ft^3	138.28	138.59	132.10	125.17		129.98	144.08	144.08
Mean, lbm/ft^3	115.16	119.52	109.16	113.24		115.77	121.75	116.87
Standard Deviation, lbm/ft^3	10.09	8.78	12.38	10.89		6.41	10.70	9.90
Count	169	176	32	80		160	110	727
Tpcpun								
Data Interval, ft	222.5-255.5	292.5-325.0	--	--	--	110.5-140.0	70.5-80.0	
Minimum, lbm/ft^3	119.61	116.87				139.34	133.03	116.87
Maximum, lbm/ft^3	138.53	144.15				111.31	142.65	144.15
Mean, lbm/ft^3	131.75	133.94				127.41	137.45	131.74
Standard Deviation, lbm/ft^3	4.30	6.76				7.19	3.18	6.70
Count	67	66				60	20	213
Tpcpul								
Data Interval, ft	256.0-360.0	325.5-424.5	--	--	--	140.5-178.0	80.5-88.0	
Minimum, lbm/ft^3	111.87	114.87				111.85	128.48	111.85
Maximum, lbm/ft^3	136.65	146.96				129.98	135.91	146.96
Mean, lbm/ft^3	127.61	134.75				121.44	132.97	129.69
Standard Deviation, lbm/ft^3	4.74	7.07				4.81	2.24	7.45
Count	209	199				76	16	500

T:\YMP\4200\data\schlumberger

Table 12. Statistical Summary of Density Measurements by Lithostratigraphic Unit (Continued)

Unit (Symbol)	RF#16	RF#18	RF#20	RF#21	RF#22	RF#24	RF#28	All
Tpcpmn								
Data Interval, ft	360.5-402.5	425.0-469.5	--	--	--	--	--	
Minimum, lbm/ft^3	124.73	144.77						124.73
Maximum, lbm/ft^3	148.52	148.14						148.52
Mean, lbm/ft^3	143.35	146.48						144.96
Standard Deviation, lbm/ft^3	4.17	0.74						3.34
Count	85	90						175
Tpcpll								
Data Interval, ft	403.0-422.0	470.0-479.0	--	--	--	--	--	
Minimum, lbm/ft^3	126.17	136.59						126.17
Maximum, lbm/ft^3	138.90	146.83						146.83
Mean, lbm/ft^3	131.78	143.72						135.69
Standard Deviation, lbm/ft^3	3.30	2.83						6.46
Count	39	19						58
Tpcpln								
Data Interval, ft	422.5-440.0	--	--	--	--	--	--	
Minimum, lbm/ft^3	125.61							125.61
Maximum, lbm/ft^3	145.21							145.21
Mean, lbm/ft^3	132.29							132.29
Standard Deviation, lbm/ft^3	4.90							4.90
Count	36							36

T:\YMP\4200\data\schlumberger

DTN: MO0204SEPGAMDM.000

Notes: (1) Tpcrn includes Tpcrv, Tpcrl and Tpcrn.

(2) Assumption 4 (Section 5) was not considered in the statistics for data from borehole RF#21.

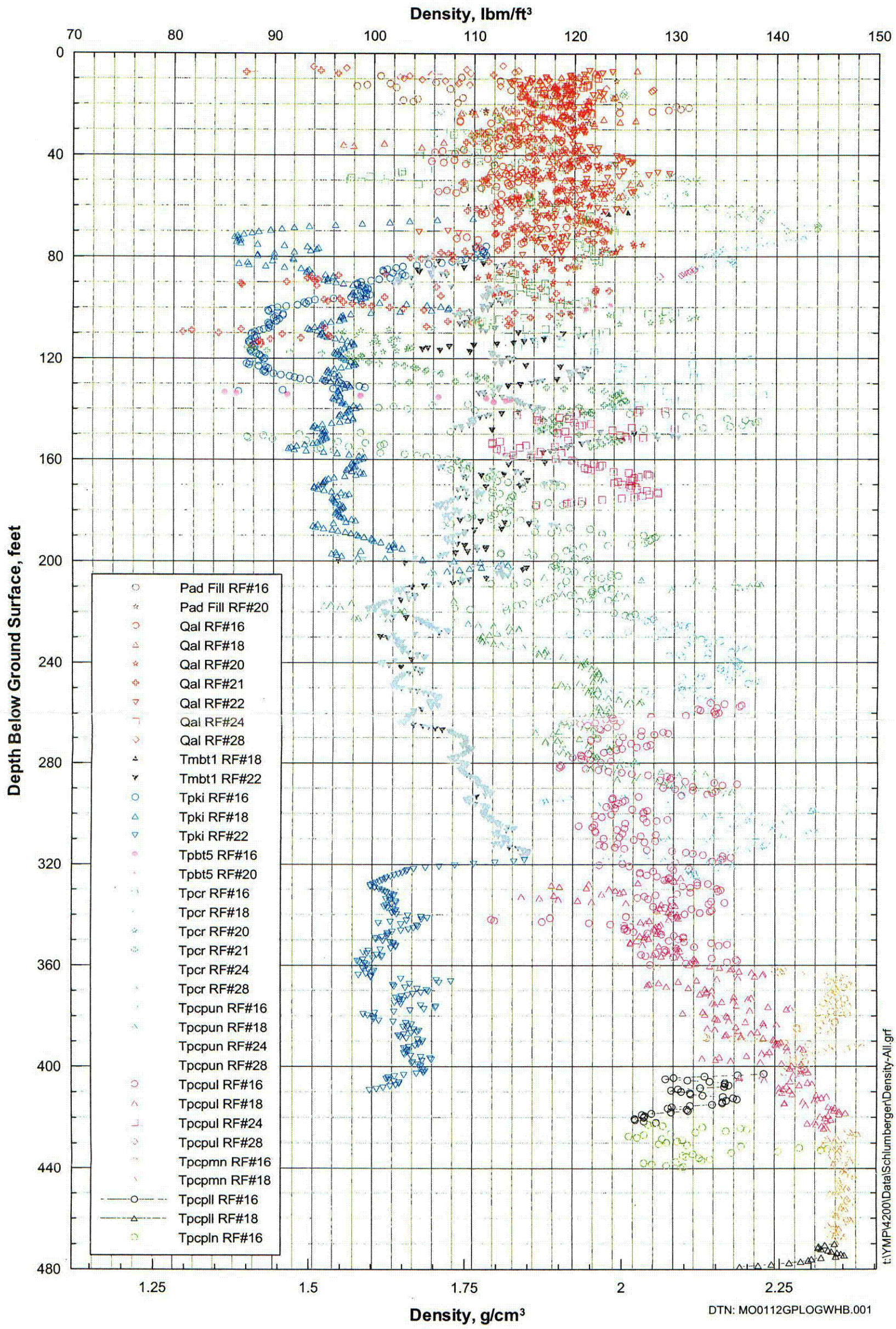

Figure 101. Density from gamma-gamma Logging as a Function of Depth and Lithostratigraphic Unit

C20

INTENTIONALLY LEFT BLANK

The following tests were performed on each sample:

- Particle-size distribution per USBR 5325-89, *Procedure for Performing Gradation Analysis of Gravel Size Fraction of Soils*; USBR 5330-89, *Procedure for Performing Gradation Analysis of Fines and Sand Size Fraction of Soils, Including Hydrometer Analysis*; and USBR 5335-89, *Procedure for Performing Gradation Analysis of Soils Without Hydrometer – Wet Sieve.*
- Water content per USBR 5300-89, *Procedure for Determining Moisture Content of Soil and Rock by the Oven Method.*
- Maximum and minimum index unit weights of the particles passing the 3-inch sieve per USBR 5525-89, *Procedure for Determining the Minimum Index Unit Weight of Cohesionless Soils*, and USBR 5530-89, *Procedure for Determining the Maximum Index Unit Weight of Cohesionless Soils.*
- Specific gravity of the particles passing the 4.75 mm (No. 4) sieve per USBR 5320-89, *Procedure for Determining Specific Gravity of Soils* (volume method).
- Specific gravity of the particles retained on the 4.75 mm (No. 4) sieve per USBR 5320-89 (suspension method).
- Liquid limit and plastic limit (Atterberg limits) per USBR 5350-89, *Procedure for Determining the Liquid Limit of Soils by the One-Point Method*, and USBR 5360-89, *Procedure for Determining the Plastic Limit and Plasticity Index of Soils.*

The test results are summarized in Table 13, and Figure 102 shows plots of the particle-size distribution results. Attachment XI shows the particle-size distribution data on multiple plots (maximum 5 results per plot).

6.2.10 Geotechnical Laboratory Dynamic Testing

Laboratory tests using combined resonant column and torsional shear (RCTS) equipment were performed to evaluate the dynamic properties of tuff and alluvium from the WHB Area. The tuff and alluvial specimens were from boreholes RF#14, RF#15, RF#16, and RF#17. The core specimens were selected to represent the various tuff units and the range of physical properties. The results from the dynamic testing of 19 specimens are presented in this section. A detailed description of this testing and the apparatus used is contained in Scientific Notebook SN-M&O-SCI-033-V1 (Wong 2002e).

6.2.10.1 Test Procedures

The RCTS equipment has been developed at the University of Texas at Austin Civil Engineering Department (UTACED) over the past two decades (Lodde 1982; Kim 1991). The equipment is of the fixed-free type, with the bottom of the specimen fixed and torsional excitation applied to the top. Both resonant column and torsional shear tests can be performed in a sequential series on the same specimen over a shearing-strain range from about 10^{-4}% to slightly more than 10^{-1}%. The primary difference between the two types of tests is the excitation frequency. In the resonant column test, frequencies above 20 Hz are required and the inertia of the specimen and drive system must be known to analyze the measurements. Slow cyclic loading involving frequencies generally below 10 Hz is performed in the torsional shear test and inertia does not enter into the data analysis.

RCTS Equipment

The RCTS apparatus can be idealized as a fixed-free system (Figure 103). The bottom end of the specimen is fixed against rotation at the base pedestal, and the top end of the specimen is connected to the driving system. The driving system, which consists of a top cap and drive plate, can rotate freely to excite the specimen in cyclic torsion.

A simplified diagram of a fixed-free resonant column test is shown in Figure 104a. The basic operational principle is to vibrate the cylindrical specimen in first-mode torsional motion. Harmonic torsional excitation is applied to the top of the specimen over a range in frequencies, and the variation of the acceleration amplitude of the specimen with frequency is obtained (Figure 104b). Once first-mode resonance is established, measurements of the resonant frequency and amplitude of vibration are made. These measurements are then combined with equipment characteristics and specimen size to calculate shear-wave velocity and shear modulus based on elastic wave propagation. Material damping is determined either from the width of the frequency response curve or from the free-vibration decay curve.

The torsional shear test is another method of determining shear modulus and material damping using the same RCTS equipment but operating it in a different manner. The simplified configuration of the torsional shear test is shown on Figure 105a. A cyclic torsional force with a given frequency, generally below 10 Hz, is applied at the top of the specimen. Instead of determining the resonant frequency, the stress-strain hysteresis loop is determined from measuring the torque-twist response of the specimen. Proximitors are used to measure the angle of twist while the voltage applied to the coil is calibrated to yield torque. Shear modulus is calculated from the slope of a line through the end points of the hysteresis loop, and material damping is obtained from the area of the hysteresis loop, as shown on Figure 105b.

The RCTS apparatus used in this study has three advantages. First, both resonant column and torsional shear tests can be performed with the same set-up simply by changing (outside the apparatus) the frequency of the forcing function. Variability due to preparing "identical" samples is eliminated so that both test results can be compared effectively. Second, the torsional shear test can be performed over a shearing-strain range between 5×10^{-4}% and about 10^{-1}%, depending upon specimen stiffness. Common types of torsional shear tests, which generate torque by a mechanical motor outside of the confining chamber, are usually performed at strains above 0.01% because of system compliance. However, the RCTS apparatus used in this study generates torque with an electrical coil-magnet system inside the confining chamber, thus eliminating the problem with an external motor. The torsional shear test can be performed at the same low-strain amplitudes as the resonant column test, and results between torsional shear and resonant column testing can be easily compared over a wide range of strains. Third, the loading frequency in the torsional shear test can be changed easily from 0.01 to 10 Hz. Therefore, the effect of frequency on deformational characteristics can be conveniently investigated using this apparatus.

Table 13. Summary of Laboratory Tests on Material Excavated for In-Situ Density Tests

Test Pit No. (1)	Depth feet	Sample No. 65A-(2)	USCS Group Symbol	Specific Gravity: Minus No. 4 Sieve Fraction	Specific Gravity: Plus No. 4 to minus 3" Sieve Fraction: Apparent	Specific Gravity: Plus No. 4 to minus 3" Sieve Fraction: Bulk SSD	Specific Gravity: Plus No. 4 to minus 3" Sieve Fraction: Bulk Oven Dry	Specific Gravity: Plus 3-inch Sieve Fraction: Apparent	Specific Gravity: Plus 3-inch Sieve Fraction: Bulk SSD	Specific Gravity: Plus 3-inch Sieve Fraction: Bulk Oven Dry	Absorption, %: No. 4 to 3" sieve Fraction	Absorption, %: Plus 3" Fraction	Water Content, %: Minus No. 4 sieve %	Water Content, %: Plus No. 4 sieve %	Particle-Size Distribution: Cobbles %	Particle-Size Distribution: Gravel %	Particle-Size Distribution: Sand %	Particle-Size Distribution: Fines(4) %	Particle-Size Distribution: % Finer than 5 microns	Index Density for Relative Density(6): Maximum lbs/ft³	Index Density for Relative Density(6): Minimum lbs/ft³
1	4	606	GW-GM	2.50	2.40	2.20	2.05	2.38	2.27	2.18	7.1	3.8	7.9	4.4	6.6	57.7	27.7	8.0	3.0	115.8	92.5
1	12	607	GW-GM	2.48	2.48	2.28	2.15	2.34	2.21	2.11	6.0	4.8	7.5	4.0	7.5	55.5	27.9	9.1	3.3	117.6	92.4
1	12	614	GP-GM	2.52	2.43	2.28	2.17	-	-	-	5.1	-	4.4	3.3	0	51.7	39.1	9.2	4.4	127.4	95.5
1	12.3	615	SP-SM	2.55	2.42	2.21	2.06	-	-	-	7.4	-	5.6	3.9	0	44.2	47.8	8.0	4.9	122.6	93.0
1	20	608	GP	2.52	2.47	2.29	2.15	2.40	2.27	2.18	6.0	4.2	4.8	3.9	7.8	60.1	28.8	3.3	1.4	120.2	93.8
2	8	616	GP	2.51	2.41	2.22	2.07	2.38	2.29	2.22	6.9	2.9	10.6	5.91	10.3	57.0	30.1	2.6	2.3	115.4	89.4
2	12	620	GP-GM	2.50	2.47	2.26	2.12	2.30	2.18	2.09	6.7	4.3	5.8(7)	5.8(7)	10.6	55.3	28.7	5.4	1.9	119.6	98.2
2	16	624	GW-GM	2.52	2.48	2.27	2.13	-	-	-	6.7	-	8.7	6.3	0	60.3	33.9	5.8	4.5	116.4	92.0
2	16	625	SW-SM	2.55	2.50	2.28	2.14	-	-	-	6.8	-	7.4	6.1	0	37.2	53.6	9.2	8.0	115.1	93.5
2	16	626	SP-SM	2.48	2.51	2.29	2.14	-	-	-	6.9	-	5.3	3.9	0	37.3	56.8	5.9	5.1	112.8	87.5
2	19	628	GW	2.51	2.51	2.26	2.10	-	-	-	7.8	-	9.6	6.9	0	55.4	40.1	4.5	4.5	118.6	91.9
3	8	617	GP-GM	2.56	2.49	2.28	2.15	-	-	-	6.4	-	3.5	2.3	0	49.4	40.6	10.0	7.7	121.5	90.0
3	8	618	GP-GM	2.54	2.46	2.27	2.13	-	-	-	6.2	-	4.4	3.6	0	70.4	21.7	7.9	3.6	116.6	92.9
3	8	619	GP-GM	2.54	2.42	2.24	2.12	-	-	-	5.9	-	5.1	3.0	0	79.0	16.0	5.0	2.5	112.3	88.0
3	12	621	GP	2.50	2.45	2.27	2.15	-	-	-	5.8	-	8.9	6.3	0	73.9	24.5	1.6	1.5	113.8	92.3
3	12	622	GP	2.54	2.49	2.30	2.17	-	-	-	5.9	-	6.9	4.2	0	76.3	18.8	4.9	2.9	108.2	84.4
3	12	623	GP-GM	2.54	2.48	2.29	2.16	-	-	-	6.0	-	4.1	3.0	0	59.7	31.3	9.0	4.3	125.3	94.9
3	19	629(3)	GW-GM	2.53	2.44	2.26	2.13	-	-	-	6.0	-	16.0	7.7	0	66.2	24.5	9.3	6.3	96.9	83.3
4	4	627	GW	2.48	2.48	2.28	2.14	2.40	2.28	2.20	6.4	3.7	6.7(7)	6.7(7)	3.5	58.8	33.0	4.7	1.2	118.1	88.8
4	8	631	GP-GM	2.50	2.50	2.25	2.08	-	-	-	8.1	-	6.9	5.0	0	46.9	45.6	7.5	4.5	124.9	92.6
4	12	632	GP	2.47	2.46	2.23	2.07	-	-	-	7.6	-	8.0	4.7	0	57.7	37.5	4.8	3.4	112.9	91.5
4	16	633	GW-GM	2.50	2.51	2.26	2.10	-	-	-	7.9	-	8.0	6.6	0	48.4	45.4	6.2	4.2	117.5	90.7

DTN: GS020483114233.004

NOTES:
(1) The complete test pit designation is preceded by TP-WHB-
(2) Laboratory Sample Index Number
(3) Sample 629 has a liquid limit of 32, a plastic limit of 26 and a plasticity index of 6. All other samples were non-plastic.
(4) Fines means particles passing the No. 200 sieve (silt and clay).
(5) – in a cell means the parameter was not measured.
(6) Minus 3-inch material.
Total water content.